NOTCH SENSITIVITY OF FATIGUE BEHAVIOR OF A Hi-NICALON/SiC CERAMIC COMPOSITE WITH AN OXIDATION INHIBITED MATRIX AT 1200˚C IN AIR AND IN STEAM

THESIS

Kurtz, Garrett, Second Lieutenant, USAF
AFIT/GAE/ENY/11-M17

DEPARTMENT OF THE AIR FORCE
AIR UNIVERSITY

AIR FORCE INSTITUTE OF TECHNOLOGY

Wright-Patterson Air Force Base, Ohio

AFIT/GAE/ENY/11-M17

NOTCH SENSITIVITY OF FATIGUE BEHAVIOR OF A Hi-NICALON/SiC CERAMIC COMPOSITE WITH AN OXIDATION INHIBITED MATRIX AT 1200˚C IN AIR AND IN STEAM

THESIS

Presented to the Faculty

Department of Aeronautics and Astronautics

Graduate School of Engineering and Management

Air Force Institute of Technology

Air University

Air Education and Training Command

In Partial Fulfillment of the Requirements for the

Degree of Master of Science in Aeronautical Engineering

Garrett Kurtz, B.S.

Second Lieutenant, USAF

March 2011

AFIT/GAE/ENY/11-M17

NOTCH SENSITIVITY OF FATIGUE BEHAVIOR OF A Hi-NICALON/SiC CERAMIC COMPOSITE WITH AN OXIDATION INHIBITED MATRIX AT 1200˚C IN AIR AND IN STEAM

Garrett Kurtz, B.S.

Second Lieutenant, USAF

Approved:

Marina Ruggles-Wrenn, PhD (Chairman)	16 MRR 11 Date
Thomas Eason, PhD (Member)	3/10/2011 Date
Geoff Fair, PhD (Member)	16 MAR 11 Date

Abstract

The effects of holes on the fatigue behavior of an advanced Silicon Carbide/Silicon Carbide (SiC/SiC) ceramic matrix composite (CMC) was investigated at 1200°C in laboratory air and in steam environment. The composite consisted of an oxidation inhibited HyprSiC matrix reinforced with laminated Hi-Nicalon fibers woven in an eight-harness-satin weave (8HSW). Fiber preforms were coated with pyrolytic carbon (PyC) fiber coating with boron carbide overlay and were then densified with HyprSiC matrix via chemical vapor infiltration (CVI). Effects if center hole on tensile stress-strain behavior and tensile properties were evaluated at 1200ºC. To assess the effect of holes on fatigue performance, the standard dogbone-shaped specimens with a center-hole were subjected to tension-tension fatigue tests at frequencies of 0.1, 1.0, and 10 Hz for fatigue stresses ranging from 80 to 140 MPa in air and from 100 to 140 MPa in steam. The R ratio (minimum stress to maximum stress) was 0.05. Fatigue run-out was defined as 10^5 cycles at the frequency of 0.1 Hz and as $2x10^5$ cycles at the frequencies of 1.0 and 10 Hz. Strain accumulation with cycles and modulus evolution with cycles were analyzed for each fatigue test. The presence of steam degraded fatigue performance at stress levels above the proportional limit (137.5 MPa). Fatigue limit was 80 MPa (32% UTS) in air and 100 MPa (40% UTS) in steam at 0.1 Hz, 100 MPa in air and steam at 1.0 Hz, and 140 MPa (56% UTS) in air at 10 Hz. Specimens that achieved run-out were tested in tension to failure to characterize the retained tensile properties. Specimen tested in air retained 74-81% of their tensile strength and specimen tested in steam retained 82-87% of their tensile strength. The modulus loss in air and in steam was limited to 65%. Composite microstructure, as well as

damage and failure mechanisms were investigated revealing oxidation on all fatigued specimen fracture surfaces, with oxidation being more pronounced in specimens tested in steam.

Acknowledgements

I would like to extend a heartfelt thank you to the following individuals: Dr. Ruggles-Wrenn for her continuous guidance and support throughout the entirety of this research project, Captain Mike Knauf and Lieutenant Tyler Jones for their help in the laboratory, my fellow yeomen for their advice and guidance on always doing what is right, and my fiancée for her love and support.

Table of Contents

List of Figures

List of Tables

NOTCH SENSITIVITY OF FATIGUE BEHAVIOR OF A Hi-NICALON/SiC CERAMIC COMPOSITE WITH AN OXIDATION INHIBITED MATRIX AT 1200˚C IN AIR AND IN STEAM

I. Introduction

With rapid advances in the aircraft engine industry and an increased demand to effectively and reliably perform higher and faster, new materials must be explored to determine their worthiness for use in aerospace applications. Increasing performance requires greater loads realized in aircraft components. In aircraft, like any industry, gains in performance are limited by the availability of materials. The desired performance gains can be realized in the aerospace industry with the implementation of structural ceramics [5:9]. In turbine engines, operating at higher temperatures allows for increased power, specific fuel consumption, and a reduction in emissions. Operating temperatures are currently limited by the materials contained in propulsion systems. Traditional metal alloys found in the power plants of aircraft today are now being replaced by a family of structural ceramics: namely, ceramic matrix composites (CMCs). CMCs are capable of reliable operation under extreme thermal and oxidative conditions and possess thermostructural properties required for long-term component service [8:1].

Figure 1 shows a comparison of strength to weight ratio of various materials as a function of temperature. It can easily be seen that CMCs are capable of retaining their strength at much higher operating temperatures than other materials currently used in aircraft engines [18]. This high temperature strength as well as fracture toughness and thermal resistance are all properties CMCs are expected to provide to structural components. Past studies have

examined fatigue behavior of CMCs, including the particular composite analyzed in the present study; however, most studies are limited to unnotched CMCs [15: 631]. The notch to be examined is in the form of a machined hole located in the center of each specimen.

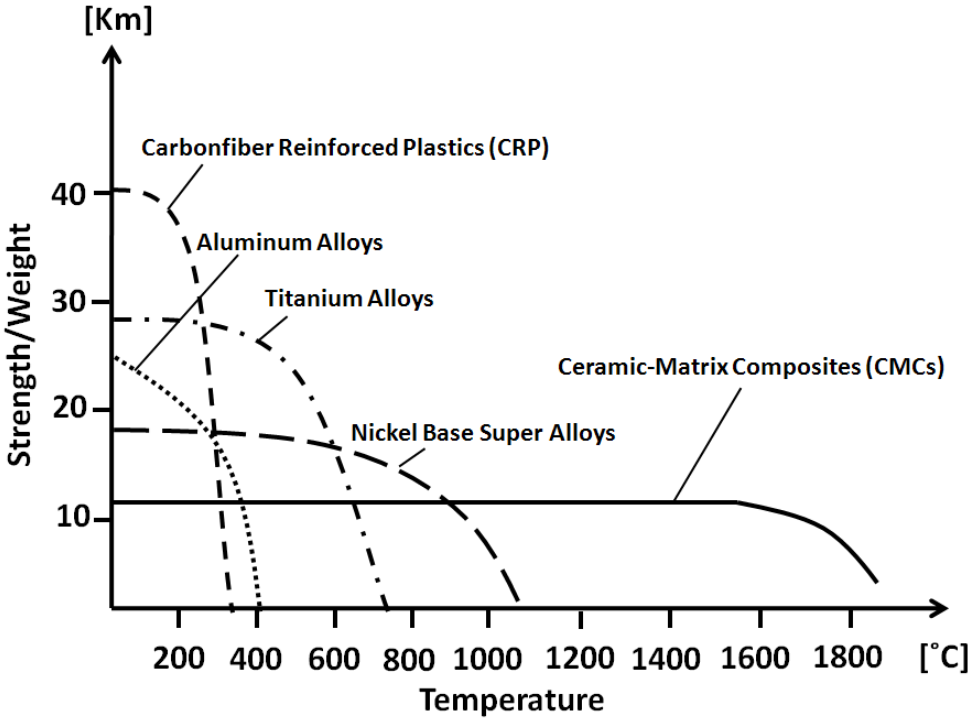

Figure 1: Strength to weight ratio as a function of temperature for select materials [18].

Holes were examined to explore the effects of notches and other stress concentrations on the fatigue behavior of CMCs. The hole is representative of stress concentrations found at attachment points. With analysis of such stress concentrations, mechanical behavior boundaries of the composite as well as its limitations for use in aerospace applications can be determined. Damage tolerance of such materials can also be explored with analysis of such stress concentrations.

One driving force in this research effort is the Versatile Affordable Advanced Turbine Engines (VAATE) program. This program makes an effort to advance aircraft engine technology for both the U.S. military as well as commercial aviation propulsion applications [1: 2]. Specific improvements to be achieved (as outlined by the VAATE executive summary) are (i) 200% increase in engine thrust-to-weight ratio (a key jet engine design parameter); (ii) 25% reduction in engine fuel consumption (and thus fuel cost); and (iii) 60% reduction in engine development, procurement, and life cycle maintenance cost [1: 2]. In order to realize these specific improvements, combustion and turbine inlet temperatures must increase. This, in turn, will cause greater operating stresses and strains on engine components [11: 1].

Weight savings can be realized with the implementation of CMCs. Ceramics have a lower density than the nickel based super alloys seen in Figure 1. This less dense material leads to weight savings realized in lighter parts. By being able to operate at elevated temperatures, the need for cooling of turbine blades is reduced, if not eliminated. With less need to cool hot engine components, there is more air going through the engine, thus more energy is extracted by the turbine. The thrust-to-weight ratio is therefore increased with reduced weight. An increased operating temperature also allows for greater combustion efficiency, reducing fuel consumption.

This thesis attempts to draw conclusions from the fatigue behavior in a variety of ways- namely comparison of collected test data to that of an unnotched specimen and microscopic imagery to determine mechanical degradation mechanisms to provide information critical to the ongoing development of materials for propulsion applications.

II. Background

2.1 Ceramic Matrix Composites

A typical CMC is made up of a ceramic matrix and reinforcing fibers. CMCs were developed to provide the thermal and environmental resistive qualities of ceramics and incorporating fibers into them to increase the damage tolerance of the ceramic. Failure strains of the matrix are typically 0.1-0.2% while the failure strains of the fibers are approximately 1-1.5% under an applied tensile load. Because of its smaller strain threshold, the matrix of a CMC will always fail before the fibers [16: 183]. This behavior is typified in the idealized CMC stress-strain curve shown in Figure 2. The tensile load is carried primarily by the matrix in region one, until microcracking of the matrix begins as tensile stress is increased. It is at this point, known as the proportional limit, that the fibers begin to carry the load as seen in section two of Figure 2. After this initial matrix cracking, the elastic modulus begins to decrease. With increasing stress, the fibers bridge the microcracks of the matrix to restrict crack opening. Once the ultimate stress is reached, fiber failure occurs until complete fracture of the specimen [16: 183].

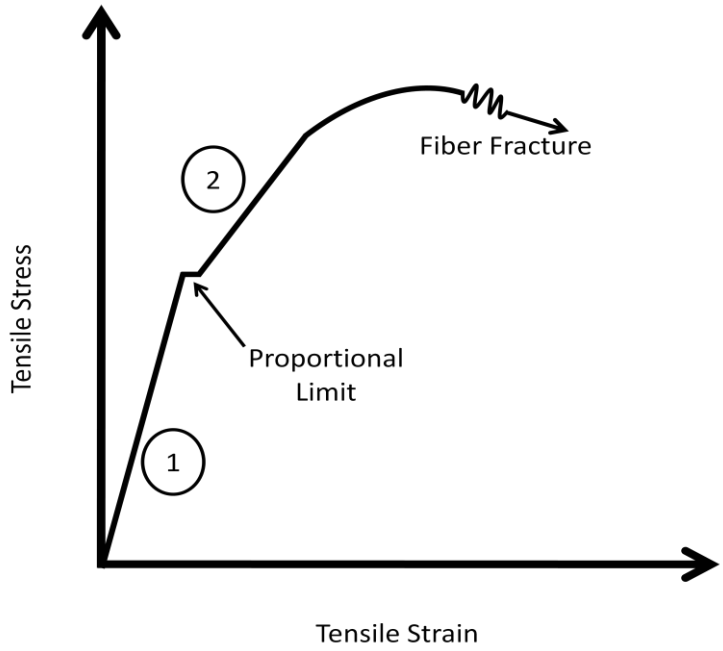

Figure 2: Idealized stress-strain behavior of ceramic fiber composites

The problem with microcracking in the matrix is the boron-nitride-rich interface between the matrix and the fibers found in most successful CMCs. The boron-nitride layer provides the weak interface necessary for fiber pullout and material toughness. Once in a high temperature environment, however, the strains are higher than the strains at the proportional limit and the environmental air is able to penetrate to the interfacial regions between the matrix and the fibers resulting in: (i) removal of the carbon rich interface, (ii) oxidation of the fiber (increasing notch sensitivity), and (iii) accelerated fiber-matrix bonding with associated return to brittle behavior. Result (iii) is commonly referred to as the oxidation embrtittlement failure mechanism found in most fiber reinforced ceramic composites [16: 184].

The embirttlement failure is expected to worsen under cyclic loading since the reaction gases contained inside the microcracks within the matrix are expelled during unloading. The

surrounding oxidizing atmosphere is drawn into the composite through these matrix cracks during reloading. As a consequence of the oxidative environment, cyclic loading is theorized to accelerate fiber fracture of CMCs because of a bonding occurring between the fibers and the matrix, limiting the extent of further sliding along the fiber/matrix interface, enhancing fracture toughness [17: 1331].

2.2 Notch Effects & Stress Concentrations

For CMCs to be used effectively in aerospace applications with sites of stress concentration, the decrease in fracture toughness at elevated temperature must be minimized [14: 3087]. It is theorized [3: 645] that CMCs can have a notch-insensitive behavior resulting from the ability of the matrix to crack and redistribute stresses around holes and notches, similar to yielding in a metal alloy around a stress concentration. Local stresses in the notched regions of specimens often exceed the proportional limit of the composite, thus acting as crack and damage initiation sites. To explore notch effects in composites, especially CMCs, a hole is typically studied.

Stress redistribution around a hole in a specimen occurs as a result of local inelastic straining [17: 1337]. Allowance for some matrix cracking at points of high stress concentration considerably increases the load carrying capabilities of CMCs. The nonlinear stress-strain behavior associated with matrix cracking seen in Figure 2 can redistribute and lower stresses in regions of high stress concentration, in much the way that plastic deformation accommodates stress concentration in metals [10:1245].

"A weak interface between the matrix and the reinforcing material aids the bridging mechanism. When a matrix crack encounters a fiber/matrix interface, this interface experiences Mode II loading; debonding occurs if the fracture energy of the interface is low. If the extent of debonding is sufficient, the matrix crack bypasses the fiber, leaving it intact" [17: 288]. This behavior enables the fiber to predominately carry the load, providing increased damage tolerance.

Prior research [17] on notch sensitivity of fatigue life in SiC composites at elevated temperature indicated mild to moderate influence of a center hole on a SiC composite. This was hypothesized to be caused by a "threshold stress" approximately equal to the matrix cracking limit (proportional limit) to be exceeded in application in fatigue testing. Other studies [3] showed none to mild sensitivity to notches.

2.3 SiC/SiC Ceramic Matrix Composites Prior Research

Recent research efforts [6, 7] explored effects of steam environment on fatigue resistance of two advanced SiC fiber-reinforced composites at 1200°C. Both composites were reinforced with laminated woven Hi-Nicalon fibers. Fiber preforms were coated with pyrolytic carbon with boron carbide overlay. The first composite [6] had a SiC matrix densified by CVI, the second composite [7] had an oxidation inhibited SiC matrix densified by CVI.

Both studies [6, 7] indicated excellent fatigue resistance in laboratory air at 1200°C and a decreased fatigue life as fatigue stress was increased. A reduction in stiffness with increasing fatigue cycles was also detected in both cases. Steam degraded fatigue resistance in the composite without the oxidation inhibited matrix but had minor influence at 1.0 Hz (except at

140 MPa) on the composite with the oxidation inhibited matrix. Considerable strain ratcheting was observed in the composite with the oxidation inhibited matrix while minimal strain ratcheting was noticed in the matrix without. Prior fatigue also appeared to have a large effect on retained properties on the composite with the oxidation inhibited matrix while not having a large affect on the other composite tested.

Results also revealed that the material with an oxidation inhibited SiC matrix exhibited improved fatigue durability in a steam environment at 1200°C. This effort aims to investigate the effects of notches on the fatigue life of the Hi-Nicalon fiber-reinforced composite with an oxidation inhibited SiC matrix at 1200°C in air and in steam.

III. Material and Test Specimen

3.1 Material

The material used for the current research effort was manufactured by Hyper-Therm High-Temperature Composites, Inc., Huntington Beach, CA, by chemical vapor infiltration (CVI) of HyperSiC oxidation inhibited matrix material into the woven Hi-Nicalon fiber performs. The composite was supplied in the form of three 5 mm thick plates. The composite consisted of eight plies of Hi-Nicalon [0°/90°] fabric woven in an eight harness satin weave (8HSW). To produce the laminate performs, the 8 [0°/90°] plies were laid-up symmetric about the mid-plane with warp and fill plies alternated. Prior to matrix densification, the performs were coated with pyrolytic carbon with boron carbide overlay in order to decrease interface bonding between fibers and matrix, thereby increasing composite strength and toughness. The thickness of the pyrolytic carbon fiber coating was ~0.40 µm and the thickness of the boron carbide overlay was ~1.0 µm. The HyprSiC oxidation inhibited matrix was densified by CVI. The fiber volume was 35.1% and the density of the composite was 2.59 g/cm^3. The tensile specimens (dimensions are given in section 3.2 below) had an outer seal coating of HyprSiC that was applied by chemical vapor deposition (CVD) after the specimens had been machined to include the addition of a center hole in each specimen.

3.2 Test Specimen

Preparation

Eight specimens were cut from three different panels for a total of twenty-four specimens to be tested. Test specimens were received from the manufacturer in a rectangular shape (Figure 3). Aluminum tabs were glued on using M-Bond 200 adhesive and M-Bond 200 Catalyst-C manufactured by Vishay Micro Measurements. These tabs were used to prevent producing stress concentrations in the gripping sections of the specimens which could inadvertently cause early failure in the gripped areas. Table 1 provides the specimen dimensions from each of the three panels used in testing. All measurements were taken in the test section. Small variations are primarily due to the fiber weave. Three measurements were taken of both width and thickness and the average of each was used as the final dimension. The total cross sectional area, A, of the test section was calculated using the equation A=t(w-2a) where t is the thickness, w the width, and 2a the hole diameter. All specimens had a center hole of diameter 2a = 4.4mm and a nominal thickness of 5 mm. Figure 3 provides a schematic with dimensions of the test specimens.

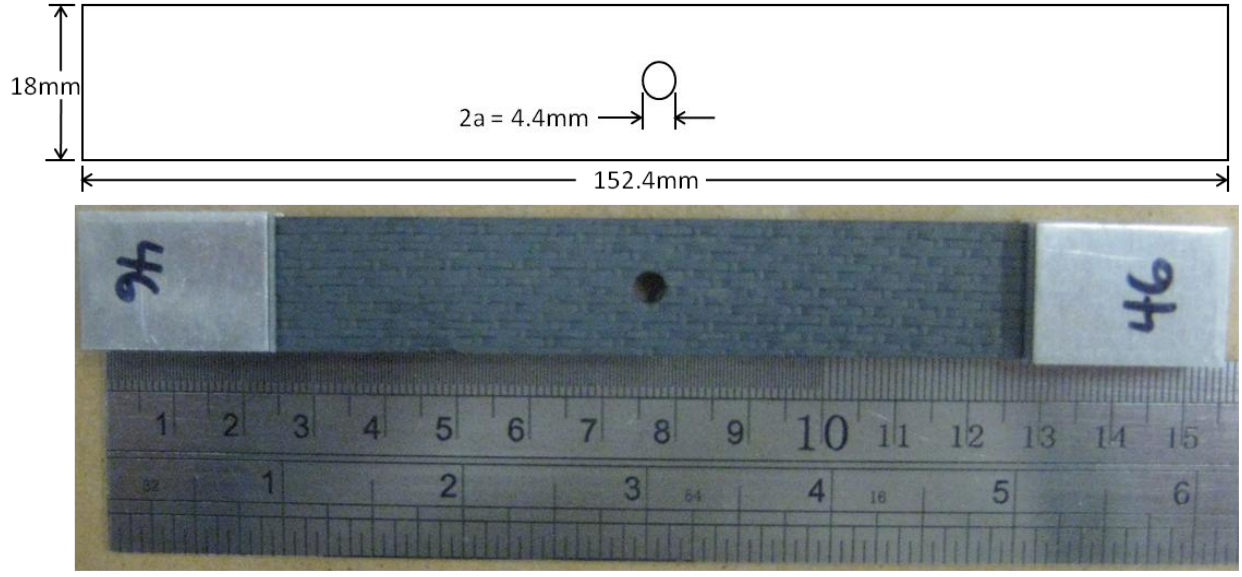

Figure 3: Specimen dimensional drawing (top) and specimen prior to testing (bottom)

Table 1: Dimensions of Hi-Nicalon/PyC/HyprSiC specimens tested in laboratory air and steam at 1200°C.

Specimen	Width (mm)	Thickness (mm)	Hole (mm)	Area (mm^2)
Panel 10C362-1				
11	18.16	3.59	4.4	49.46
12	18.12	3.64	4.4	50.02
13	18.11	3.66	4.4	50.15
14	18.15	3.58	4.4	49.24
15	18.15	3.56	4.4	48.89
16	18.17	3.56	4.4	48.98
17	18.17	3.54	4.4	48.80
18	18.14	3.56	4.4	48.84
Panel 10C362-3				
31	18.21	3.52	4.4	48.59
32	18.16	3.35	4.4	46.14
33	18.20	3.51	4.4	48.37
34	18.16	3.49	4.4	48.06
35	18.17	3.53	4.4	48.63
36	18.17	3.54	4.4	48.80
37	18.17	3.45	4.4	47.58
38	18.17	3.48	4.4	47.93
Panel 10C362-4				
41	18.20	3.54	4.4	48.89
42	18.19	3.53	4.4	48.67
43	18.17	3.52	4.4	48.45
44	18.20	3.53	4.4	48.72
45	18.19	3.53	4.4	48.67
46	18.20	3.56	4.4	49.07
47	18.17	3.45	4.4	47.58
48	18.19	3.56	4.4	49.02

IV. Experimental Arrangements and Procedures

4.1 Test Equipment and Setup

All tests were conducted using a servo-hydraulic controlled MTS 810 Material Test System 5 kip mechanical testing machine. The MTS machine was controlled by a Flextest 40 digital controller connected to a computer with MTS Station Manager installed as seen in Figure 4.

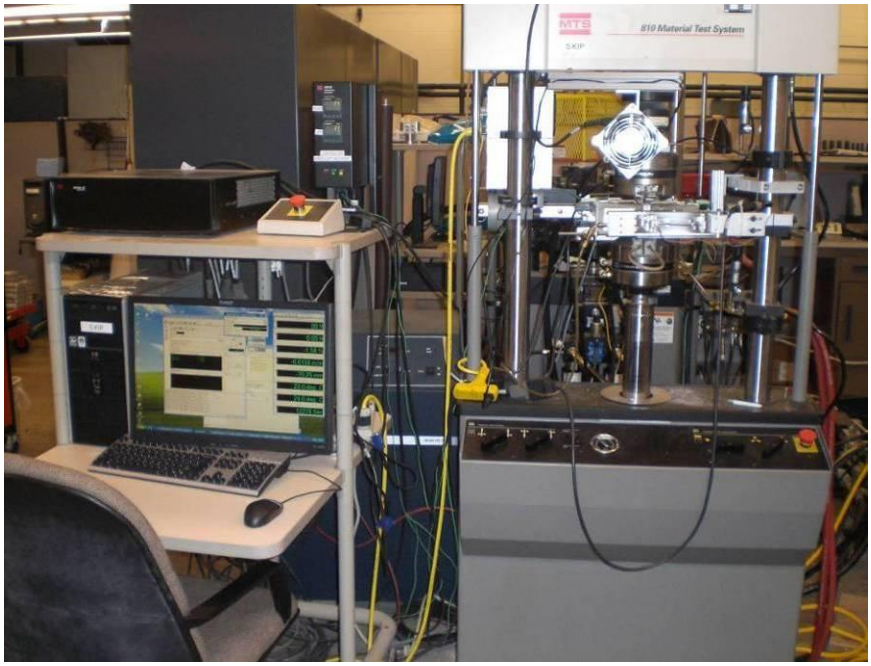

Figure 4: MTS 5 kip machine setup

This machine was equipped with water cooled wedge grips to grip the specimen. Along with the MTS machine, a two-zone resistance-heater furnace connected to a temperature controller for each zone was also used.

The machine's hydraulic system was warmed up prior to testing any specimen by running a displacement-controlled sine waveform of 0.25 in for 20 minutes. Aluminum tabs were attached to each specimen's ends using a high temperature ceramic adhesive. After warm up of the hydraulic system was completed, the specimen was placed in a susceptor (Figure 5) and the tabbed sections were then inserted into the hydraulic wedge grips.

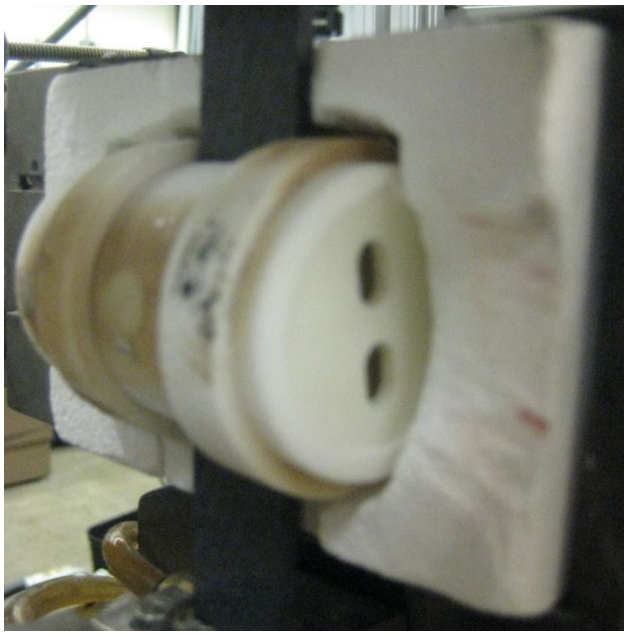

Figure 5: Specimen loaded in susceptor prior to testing

The susceptor used was an alumina cylinder with holes for both the extensometer leads as well as a steam port located in the back of the cylinder. This particular piece of equipment was used in both air and steam in order to help maintain a constant temperature inside the test section. The susceptor also separated the saturated steam environment from the laboratory air within the furnace in steam tests. The grips were cooled with 15°C water from the Naslab model HX-75 chiller and the grip pressure was set to 18 MPa to ensure the specimen would not slip. In steam tests, an AMTECO Steam Generator was used to generate the steam.

Once the specimen was mounted inside the susceptor and grips, the furnaces were closed around the susceptor. For testing, an AMTECO Hot Rail two zone furnace system was used. An R-type thermocouple was inserted into each zone to measure the temperature and provide feedback to the temperature controller. The MTS Model 409.83B Temperature Controller was used to control the furnace operating temperature and was able to control both the left and right furnaces simultaneously. After the furnaces were closed, a MTS Model 632.53 E-14 high temperature extensometer was mounted to measure strain for the duration of testing.

In order to ensure the specimen was being tested at 1200°C, a temperature calibration was performed before any further testing was done. The specimen was mounted using the same procedure as above and the test was run in load control. The specimen was straddled by two R-type thermocouples, which were connected to the Omega CL3515A digital, hand thermometer. The temperature was gradually increased until a specimen temperature of 1200°C was reached. Once the specimen temperature did not fluctuate for 2 hours, the set temperature was recorded. The same procedure was repeated for the steam environment to find the set temperature for this type of testing as well. These set temperatures were then used for all tests. Temperature recalibrations were performed as necessary when test conditions changed.

4.2 Microstructural Characterization

In order to characterize the microstructure of the tested specimens, a Zeiss Discovery V12 stereoscopic optical microscope was used (Figure 6). Photos were taken of each side of the

fracture surface. These pictures can be found in Appendix A. After optical microscopy was complete, the bottom half of each broken specimen was to be analyzed using a scanning electron microscope (SEM). Only the bottom half was analyzed because upon completion of the test, the lower head of the MTS machine would move down in order to remove the fracture surface from the test environment. The top fracture surface of each specimen was not analyzed in the SEM due to prolonged exposure to the extreme test environment. A diamond blade was used to cut the fracture surface from the specimen. The fracture surface was then mounted on an SEM pinmount using conductive double-sided tape and was now ready for analysis. A thin strip of the material was then cut from the specimen and mounted in a 1 ¼ inch conductive phenolic puck using a Buehler Simplimet 2000. After the mounting process was complete, the pucks were placed in Buehler EcoMet/AutoMet 300 for final processing. Table 2 below shows the process used in polishing (as recommended by [9: 231] and [13]). These steps were completed left-to-right in the table until finished.

Figure 6: Zeiss optical microscope (left) and Quanta 200 scanning electron microscope (right) used in microstructural characterization

Table 2: **Materialographic preparation process used as recommended for SiC materials**

SiC/SiC Polishing Method

Grind/Polish	Plane Grind	Fine Grind 1	Fine Grind 2	Fine Grind 3	Polish 1	Polish 2	Polish 3
Disk/Cloth	SiC Paper	SiC Paper	Ultrapad	Ultrapad	Texmet 2500	Texmet 2500	Chemomet
Grit (P)/Grain Size (µm)	P400	P600	15 µm	9 µm	6 µm	3 µm	0.5 µm
Lubricant	Water	Water	Suspension	Suspension	Suspension	Suspension	Suspension
Rotation Disk (rpm)	300	300	150	150	150	150	150
Rotation Holder (rpm)	150	150	150	150	150	150	150
Comp/Contra	Contra	Comp	Comp	Comp	Comp	Comp	Comp
Force Per Specimen (lb)	7	7	7	7	7	5	2
Time (min)	5	5	10	10	20	40	6

Once polishing was complete, the phenolic pucks as well as the fracture surfaces on the pinmounts were placed in the SEM and micrographs were taken using an FEI Quanta 200 HV (Figure 6).

4.3 Test Procedures

4.3.1 Monotonic Testing

In order to determine baseline material properties of each of the three panels to be used in testing, a monotonic tension test was conducted on a randomly selected specimen from each panel. A procedure was written to raise the oven temperature to the set temperature (determined from temperature calibration) at a rate of 1°C/sec in load control. Load control ensured no compressive loads on the specimen due to the thermal expansion encountered when heating the material. The temperature was then held for 20 minutes with a tolerance of ±5°C. If the temperature varied by more than these limits, the program was setup to restart the

dwell period. Once the dwell period was completed, the specimen was loaded under displacement control at a rate of 0.05mm/sec until failure occurred. Once the material failed, the lower half of the specimen was removed from the oven to limit test environment exposure to the fracture surface.

4.3.2 Fatigue Test

Specimens undergoing fatigue testing were loaded into the MTS machine similar to the monotonic tension testing. A new procedure was written for each specimen although each contained the same basic framework. The ovens were raised to the set temperature at a rate of 1°C/sec in load control before dwelling for 20 minutes with a tolerance of ±5°C. After the dwell period was completed, a 30 second ramp to the minimum stress was induced. The minimum stress was calculated as 5% of the maximum stress. It was at this time that the cyclic loading began at the prescribed fatigue rate with an R-ratio of 0.05. A sine waveform was used for loading. A peak-valley compensator was employed to ensure that the commanded minimum and maximum stresses were attained. If run-out (200,000 cycles for 1.0 Hz and 10 Hz; 100,000 cycles for 0.1 Hz) was achieved, the specimen was unloaded and a monotonic tension test was performed with a displacement rate of 0.05mm/sec to explore retained properties. Upon fracture, the bottom half of the specimen was removed from the oven (similar to the monotonic tension test) and allowed to cool in laboratory air to prevent extreme environmental effects on the fracture surface. The ovens were cooled rapidly to room temperature for tests in air and 300°C for tests in steam.

During fatigue testing, data was collected throughout the following cycles (every 0.02 sec): (i) cycles 1-25; (ii) every tenth cycle between cycles 30 and 100; (iii) every hundredth cycle between 100-1,000; (iv) every thousandth cycle between 1,000-10,000; and (v) every ten-thousandth cycle between 10,000 and run-out (or failure). Collecting data at these selected points ensured enough information to provide meaningful results without overwhelming analysis. Data was also collected at each peak and valley of cyclic loading. If the test achieved run-out, data was collected every 0.01 seconds during the tension to failure test for analysis of retained tensile properties.

V. Results and Discussion

5.1 Chapter Overview

The following chapter is a discussion of all tests conducted in this research effort. Section 5.2 presents thermal strain and linear coefficient of thermal expansion for each specimen. Section 5.3 presents the results of the four tension to failure tests performed at elevated temperature. Section 5.4 provides results for the tension-tension fatigue tests conducted in air, while section 5.5 gives results for tension-tension fatigue tests conducted in steam. Section 5.6 presents the results of retained properties for those specimens that achieved a run-out condition. Section 5.7 presents the results of the composite microstructure analysis. Comparisons to the unnotched specimen can be found throughout this chapter.

Specimens were randomly assigned a numeric identification number. The first digit in the specimen number represents the panel from which the specimen was taken from. The

second digit is simply a means of identifying each specimen. For example, specimen 32 is specimen 2 from panel 3. All tests performed in this effort are summarized in Table 3. For tests conducted at 1.0 Hz and 10 Hz, fatigue run-out was defined as 2×10^5, while tests conducted at 0.1 Hz had a run-out condition of 10^5 cycles. All fatigue testing had an R-Ratio (ratio of maximum stress to minimum stress) of 0.05.

Table 3: Summary of Hi-Nicalon/PyC/HyprSiC composite specimen data. All tests conducted at 1200°C.

Specimen	Fatigue Frequency (Hz)	Test Environment	Maximum Stress (MPa)	Elasic Modulus (GPa)	Cycles to Failure (N)	Time to Failure (h)	Failure Strain (%)
Tensile Test							
14	-	Laboratory Air	-	226.0	-	-	0.26
38	-	Laboratory Air	-	249.0	-	-	0.27
45	-	Laboratory Air	-	224.0	-	-	-
48	-	Laboratory Air	-	170.0	-	-	0.29
Tension-Tension Fatigue Test							
36	0.1	Laboratory Air	140	-	29,694	82.5	-
11	0.1	Laboratory Air	120	-	22,195	61.7	0.69
42	0.1	Laboratory Air	100	-	51,738	143.7	0.67
12	0.1	Laboratory Air	80	-	100,000[a]	277.8[a]	0.24
17	0.1	Steam	140	-	17,150	47.6	0.90
31	0.1	Steam	140	-	6,898[b]	19.2[b]	0.17
44	0.1	Steam	120	-	44,515	123.7	0.41
35	0.1	Steam	100	-	100,000[a]	277.8[a]	0.42
41	1.0	Laboratory Air	140	-	43,116	12.0	0.78
33	1.0	Laboratory Air	140	-	105,421	29.3	0.99
16	1.0	Laboratory Air	130	-	104,000	28.9	0.77
15	1.0	Laboratory Air	120	-	113,522	31.5	0.98
18	1.0	Laboratory Air	120	-	77,575	21.5	0.82
37	1.0	Laboratory Air	100	-	200,000[a]	55.6[a]	0.26
34	1.0	Steam	140	-	74,280	20.6	0.88
32	1.0	Steam	130	-	115,050	32.0	0.61
13	1.0	Steam	120	-	177,335	49.3	1.09
43	1.0	Steam	100	-	200,000[a]	55.6[a]	0.17
47	10	Laboratory Air	140	-	200,000[a]	5.6[a]	0.45
46	10	Steam	140	-	26,485	0.7	-

[a]Run-out, faiulre of the specimen did not occur when test was terminated

[b]Failure of the specimen occurred due to equipment malfunction

5.2 Thermal Expansion

Each specimen tested was heated to a test temperature of 1200°C at a rate of 1°/C and allowed to dwell for 20 minutes in zero-load control. No load was applied to the specimen to allow it to thermally strain. Thermal strain was recorded throughout the entire warm-up and dwell phases of the temperature ramp. These values were then used to calculate the coefficient of thermal expansion (CTE), α_t and can be found in Table 4. It is seen in Table 4 that specimens from all three panels tested produced similar values of α_t. The average CTE of each of the panels tested is slightly lower than the average value of 4.82×10^{-6}/°C reported by Delapasse [7: 40].

Table 4: Thermal strain produced by Hi-Nicalon/PyC/HyprSiC composite and corresponding coefficients of linear thermal strain measured for temperature rise from 23°C to 1200°C.

Specimen	Thermal Strain (%)	Coefficient of Linear Thermal Expansion, α (10^{-6}/°C)
11	0.59	5.00
12	0.49	4.13
13	0.54	4.57
14	0.57	4.85
15	0.55	4.70
16	0.51	4.37
17	0.43	3.65
18	0.50	4.26
Average	0.52	4.44
Standard Deviation	0.05	0.43
31	0.53	4.48
32	0.38	3.22
33	0.57	4.83
34	0.49	4.18
35	0.52	4.41
36	-	-
37	0.55	4.64
38	0.56	4.77
Average	0.51	4.36
Standard Deviation	0.06	0.55
41	0.55	4.67
42	0.54	4.61
43	0.55	4.70
44	-	-
45	0.54	4.60
46	-	-
47	0.60	5.10
48	0.55	4.71
Average	0.56	4.73
Standard Deviation	0.02	0.19

5.3 Monotonic Tension

Specimens from each of the three panels to be used in testing were subjected to a monotonic tension to failure test at a constant displacement rate of 0.05 mm/sec to determine baseline material properties at 1200°C. The results of these tests can be found in Table 5 and shown in a stress-strain curve in Figure 7. The average elastic modulus was 217.3 GPa, the average ultimate tensile strength (UTS) was 249.8 MPa, and the average failure strain was 0.274%. The proportional limit of each of the stress-strain curves was also determined. This is defined as the point where the stress-strain curve departs from linearity [7: 41] as seen in Figure 7. Although minor variability between panels, the proportional limit has a standard deviation of less than 2% meaning each of the panels' matricies began microcracking and transferring the load to the reinforcing fibers (as discussed in Section 2.1) at nearly the same stress level. The average proportional limit was 137.5 MPa (55% UTS).

Table 5: Tensile Properties of Hi-Nicalon/PyC/HyprSiC composite at 1200°C in laboratory air at constant displacement rate of 0.05 mm/sec

Specimen	Elastic Modulus (GPa)	Proportional Limit (MPa)	Ultimate Strength (MPa)	Failure Strain (%)
14	226.0	139.0	253.1	0.258
38	249.0	140.0	259.8	0.273
45	224.0	135.0	240.5	-
48	170.0	136.0	245.6	0.290
Average	217.3	137.5	249.8	0.274

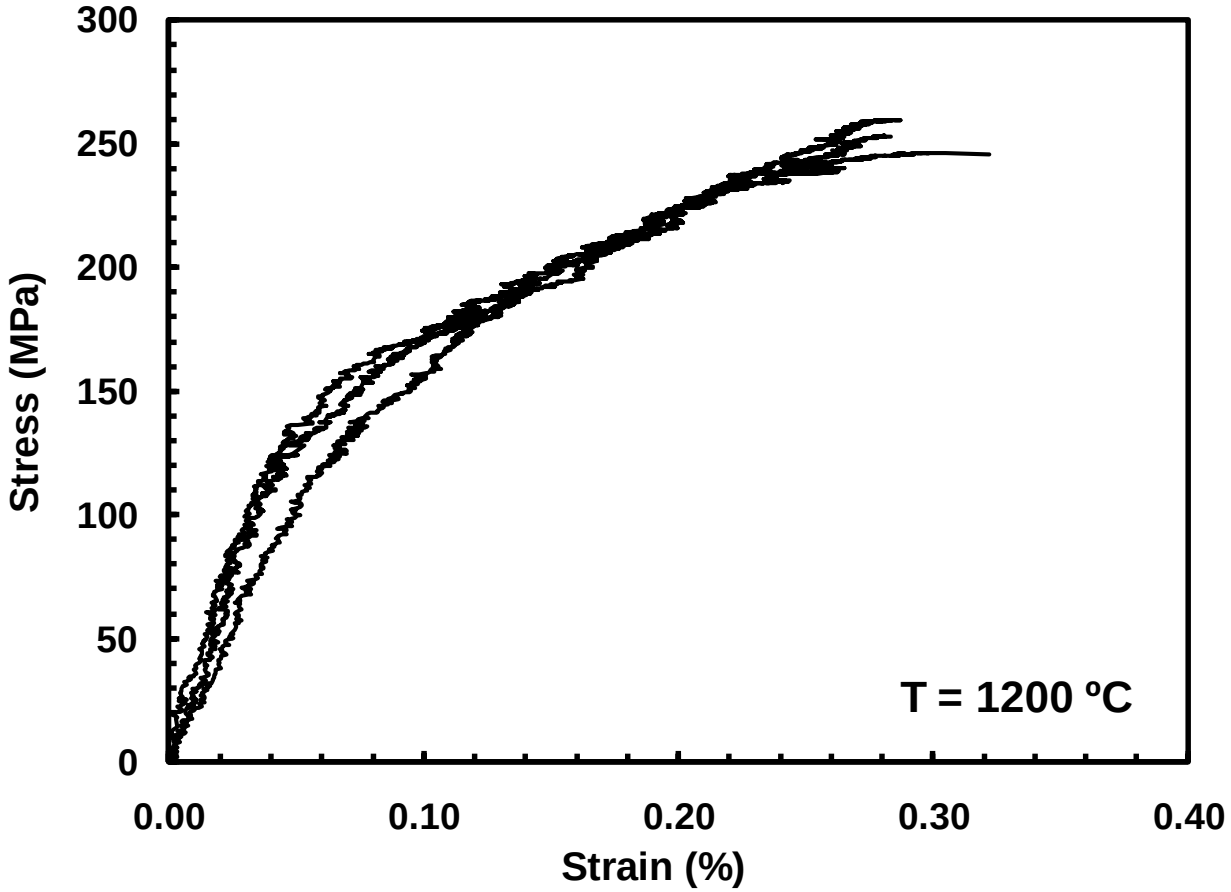

Figure 7: Tensile Stress-Strain of Hi-Nicalon/PyC/HyprSiC composite at 1200°C in laboratory air

The tensile properties were compared to that of the unnotched specimen [7] and can be found in Table 6. The stress-strain curves can also be seen as a means of comparison in Figure 8. It is seen that the notched specimen has a greater elastic modulus and proportional limit, but a lower ultimate strength and failure strain than that of the unnotched specimen tested by Delapasse [7]. The average proportional limit of the notched specimen is roughly 55% of the ultimate strength, whereas it is only 38% for the unnotched specimen's average ultimate strength. The notched specimen had a greater average density than that of the unnotched

specimen, explaining the stiffer matrix in the notched specimen. With a stiffer matrix, elastic modulus and proportional limit will be higher.

Table 6: **Summary of average tensile properties for notched and unnotched Hi-Nicalon/PyC/HyprSiC composite at 1200°C in laboratory air at constant displacement rate of 0.05 mm/sec. Data for unnotched Hi-Nicalon/PyC/HyprSiC from Delapasse [7].**

Hi-Nicalon/PyC/HyprSiC	Elastic Modulus (GPa)	Proportional Limit (MPa)	Ultimate Strength (MPa)	Failure Strain (%)
Notched	217.3	137.5	249.8	0.274
Unnotched	206.3	116.3	306.8	0.686

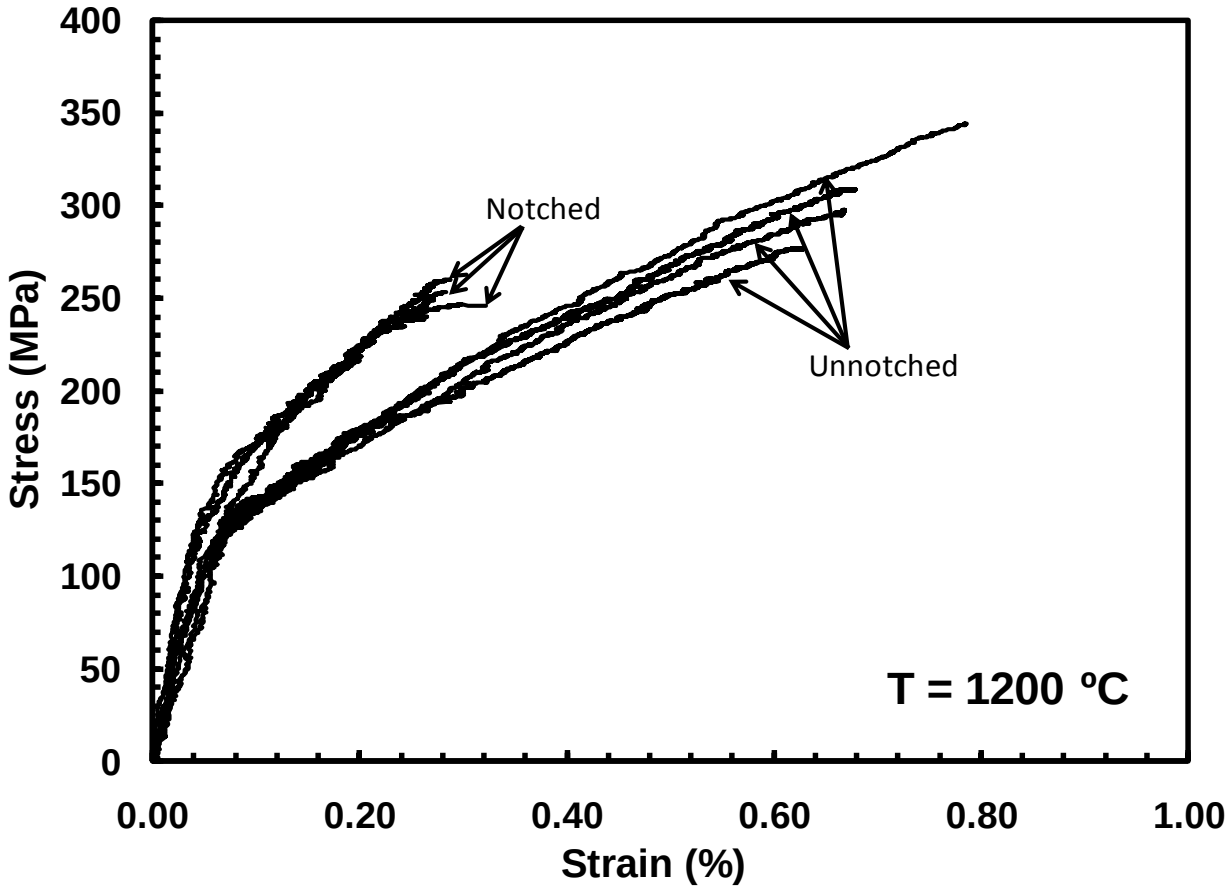

Figure 8: **Tensile stress-strain curves for notched and unnotched Hi-Nicalon/PyC/HyprSiC composite at 1200°C in laboratory air at constant displacement rate of 0.05 mm/sec. Data for unnotched Hi-Nicalon/PyC/HyprSiC from Delapasse [7].**

5.4 Tension-Tension Fatigue Test at 1200˚C in Air

Tension-tension fatigue tests were conducted at frequencies of 0.1 Hz, 1.0 Hz, and 10 Hz at 1200°C in air with an R-ratio of 0.05. A run-out condition was achieved at a stress level of 100 MPa for 1.0 Hz, 80 MPa at 0.1Hz, and 140 MPa at 10 Hz. The maximum cyclic stress ranged from 80 MPa to 140 MPa (32 to 56% UTS) at 0.1 Hz, 100 MPa to 140 MPa (40 to 56% UTS) at 1.0 Hz, and 140 MPa (56% UTS) for 10 Hz. Table 7 summarizes the results of fatigue testing in air. A stress versus cycles to failure (S-N) curve can be seen in Figure 9.

Table 7: Summary of fatigue results for Hi-Nicalon/PyC/HyprSiC composite at 1200°C in laboratory air.

Test Environment	Max Stress (MPa)	Cycles to Failure (N)	Time to Failure (h)	Failure Strain (%)
Fatigue at 0.1 Hz				
Laboratory Air	140	29,694	82.5	
Laboratory Air	120	22,195	61.7	0.59
Laboratory Air	100	51,738	143.7	0.67
Laboratory Air	80	100,000[a]	277.8	0.53
Fatigue at 1.0 Hz				
Laboratory Air	140	43,116	12.0	0.78
Laboratory Air	140	105,421	29.3	0.99
Laboratory Air	130	104,000	28.9	0.77
Laboratory Air	120	113,522	31.5	0.98
Laboratory Air	120	77,575	21.5	0.82
Laboratory Air	100	200,000[a]	55.6[a]	0.26
Fatigue at 10 Hz				
Laboratory Air	140	200,000[a]	5.6[a]	0.45

[a]Run-out, faiulre of the specimen did not occur when test was terminated

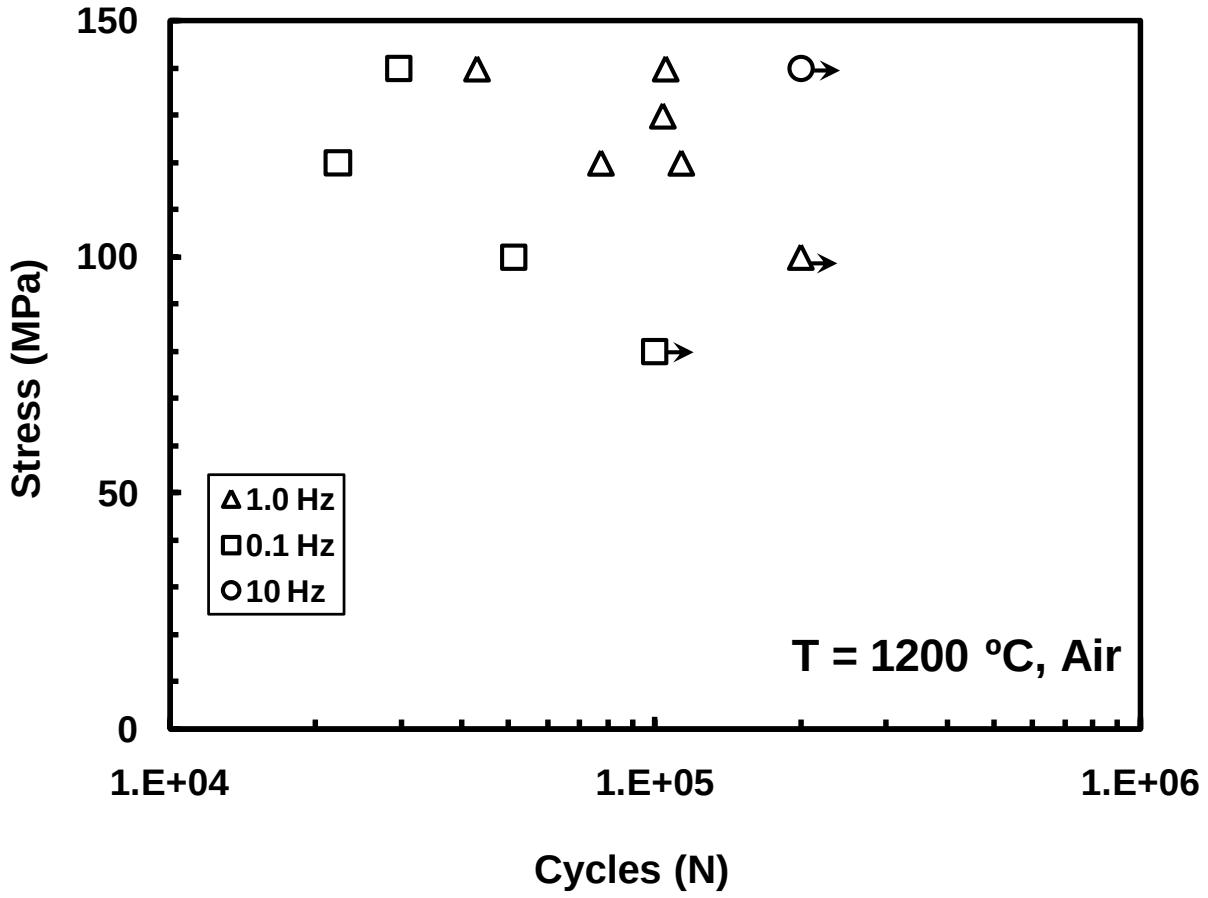

Figure 9: Fatigue S-N curve for Hi-Nicalon/PyC/HyprSiC composite at 1200°C in laboratory air.

The data in Table 7 and Figure 9 suggests that loading frequency as well as stress level has a significant effect on fatigue performance in air. The fatigue limit increased with increasing frequency with run-out being achieved at 80 MPa at 0.1 Hz, 100 MPa at 1.0 Hz, and 140 MPa at 10 Hz. Each frequency tested demonstrates a quasi-linear regression with increasing stress. Based on the presented results, as well as those reported by Delapasse [7], run-out is achieved at higher stress levels at greater fatigue frequencies.

When considering fatigue life, time to failure is important to take into account to gain a better understanding of how long the tested specimens were exposed to extreme environmental

effects. Figure 10 shows fatigue stress as a function of time to failure. This plot shows that all specimens at lower frequencies have longer fatigue lifetimes than those tested at higher frequencies at the same stress levels. The same quasi-linear regression seen in the S-N graph is demonstrated by this plot as well.

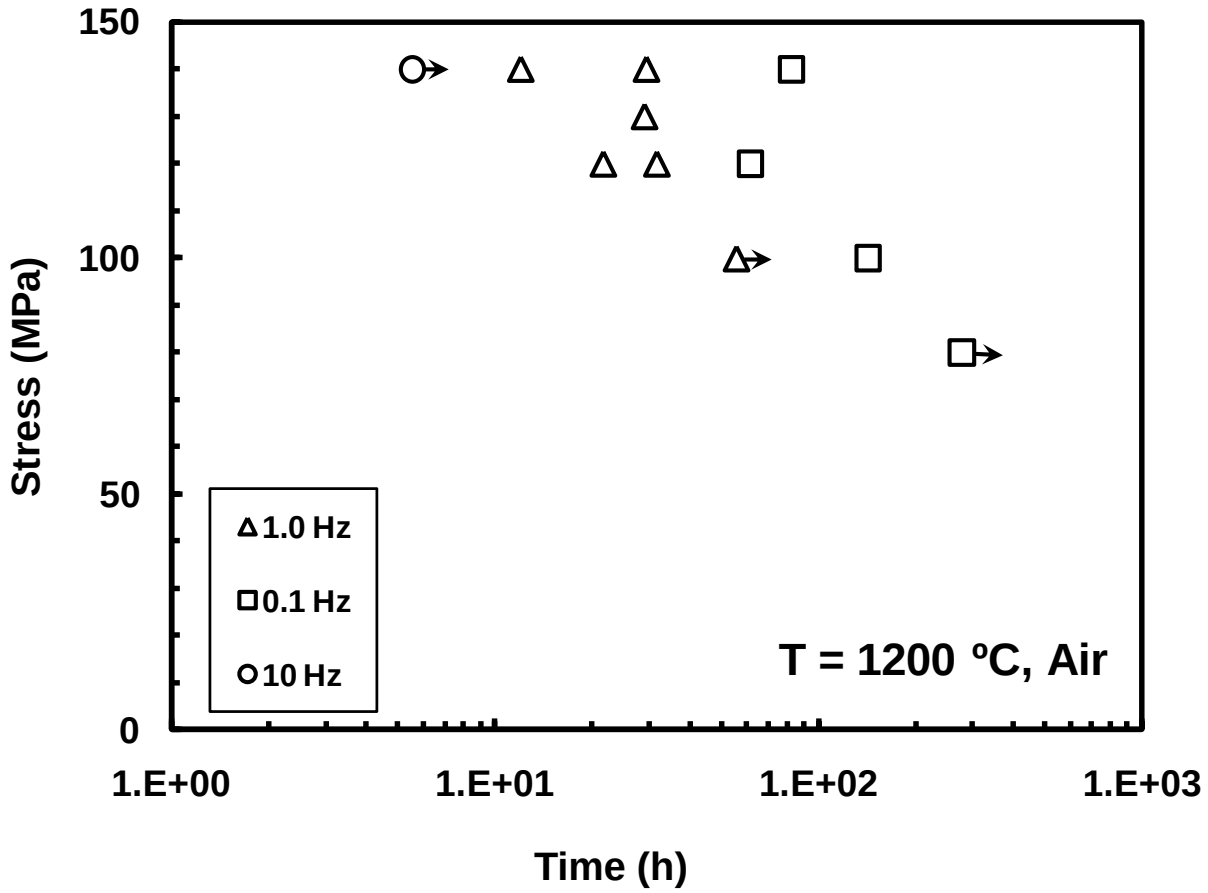

Figure 10: Fatigue stress vs. time to failure for Hi-Nicalon/PyC/HyprSiC composite at 1200°C in laboratory air.

Fatigue results were compared to the unnotched Hi-Nicalon/PyC/HyprSiC composite obtained from [7] in Figure 11 and Figure 12 to explore the effect of a center hole. Run-out was achieved for both notched and unnotched specimens at 100 MPa at 1.0 Hz and 140 MPa at 10 Hz.

The unnotched specimen had longer fatigue cycles-to-failure at all stress levels tested at a frequency of 0.1 Hz. The notched specimen, however, demonstrated greater fatigue life cycles-to-failure at 1.0 Hz at stress levels of 130 MPa and 140 MPa.

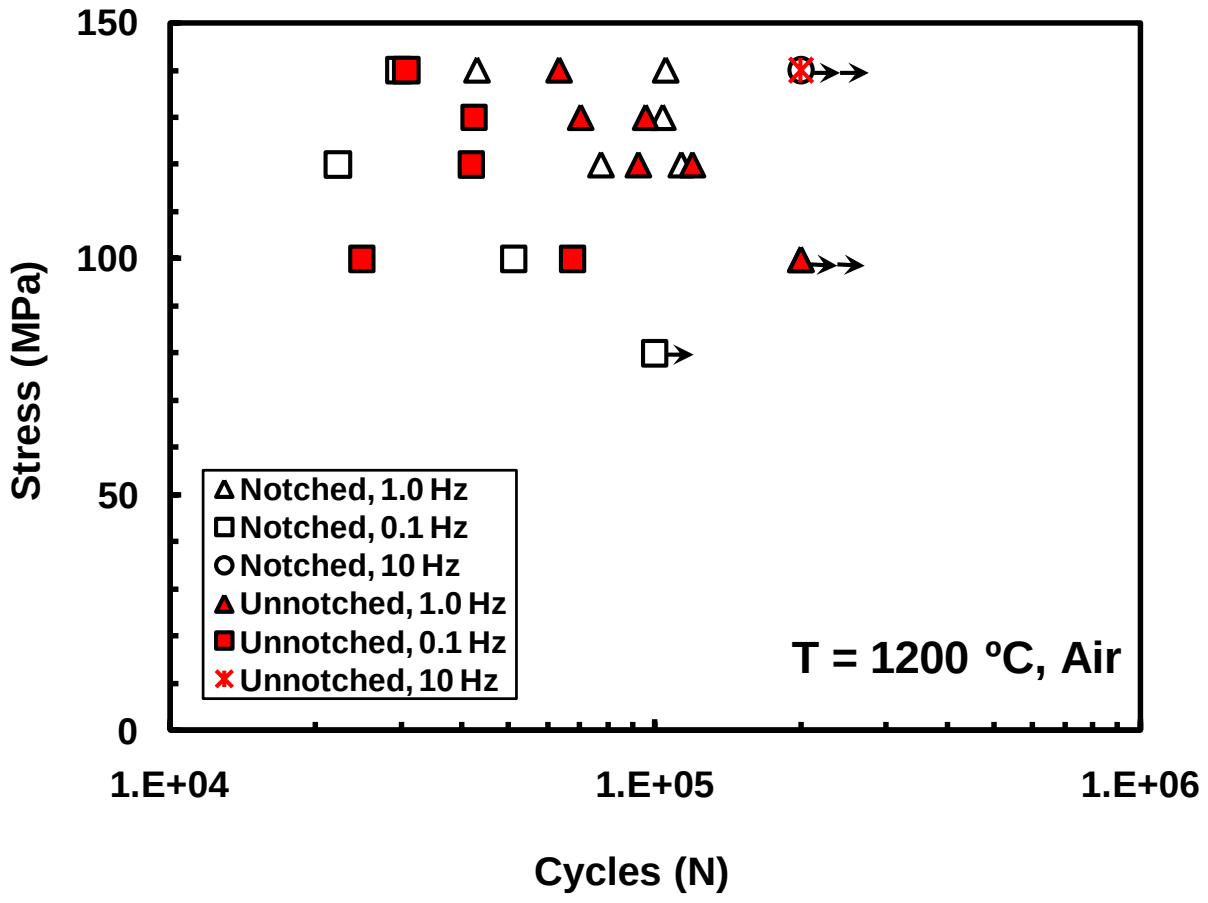

Figure 11: Fatigue S-N curve for notched and unnotched Hi-Nicalon/PyC/HyprSiC composite at 1200°C in laboratory air. Data for unnotched Hi-Nicalon/PyC/HyprSiC from Delapasse [7].

The fatigue stress as a function of time to failure for the notched specimen is compared to the unnotched data from [7] and can be seen in Figure 12. Both the notched and unnotched specimen show time-to-failure increases with decreased loading frequency.

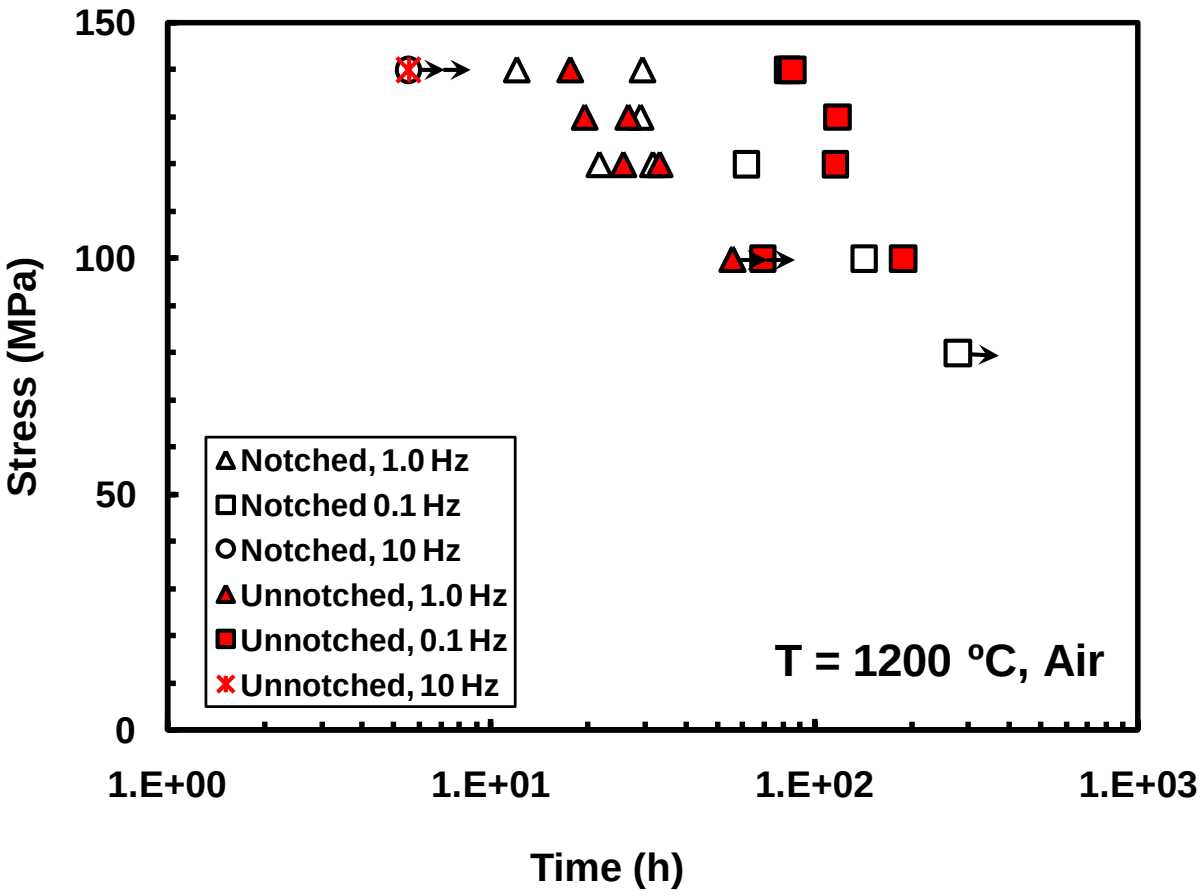

Figure 12: Fatigue stress vs. time to failure for notched and unnotched Hi-Nicalon/PyC/HyprSiC composite at 1200°C in laboratory air. Data for unnotched Hi-Nicalon/PyC/HyprSiC from Delapasse [7].

Damage development during fatigue cycling was also analyzed for this study by examining the reduction in stiffness (hysteresis modulus). This was determined from the maximum and minimum stress-strain data points for each load cycle. Figure 13 shows normalized modulus evolution with cycles. Elastic modulus (E) was normalized by the modulus at the first cycle. Modulus decreased in all specimens tested in air at 1200°C. The specimen tested at 1.0 Hz at 130 MPa showed the greatest reduction in modulus with a decrease of nearly 63%.

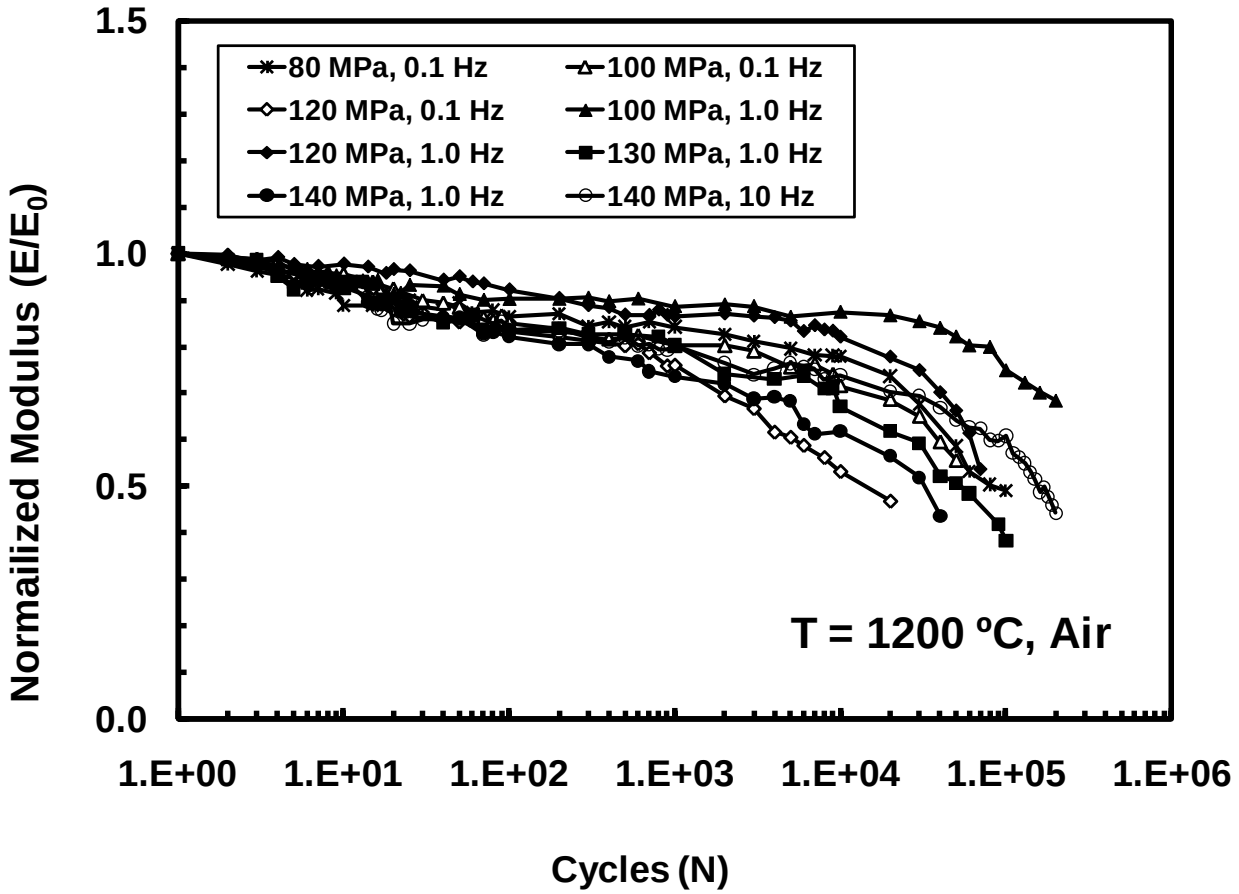

Figure 13: Normalized modulus vs. fatigue cycles for Hi-Nicalon/PyC/HyprSiC composite at 1200°C in laboratory air.

Modulus evolution with fatigue cycles was also compared to the unnotched Hi-Nicalon/PyC/HyprSiC composite presented by Delapasse [7] in Figure 14. Again, the notched

specimens had a greater density than that of the unnotched specimens. With a stiffer (denser) matrix (notched) modulus losses are not expected to be as large as those seen in the unnotched material. The notched specimen shows a greater loss of modulus initially (<1,000 cycles), but the unnotched specimen shows much greater losses in modulus overall. The greatest loss of modulus seen was also in the specimen tested at 1.0 Hz at 130 MPa with a decrease in modulus of nearly 86%. All unnotched specimens show a greater loss in modulus when compared to the notched specimen tested in the same condition in air.

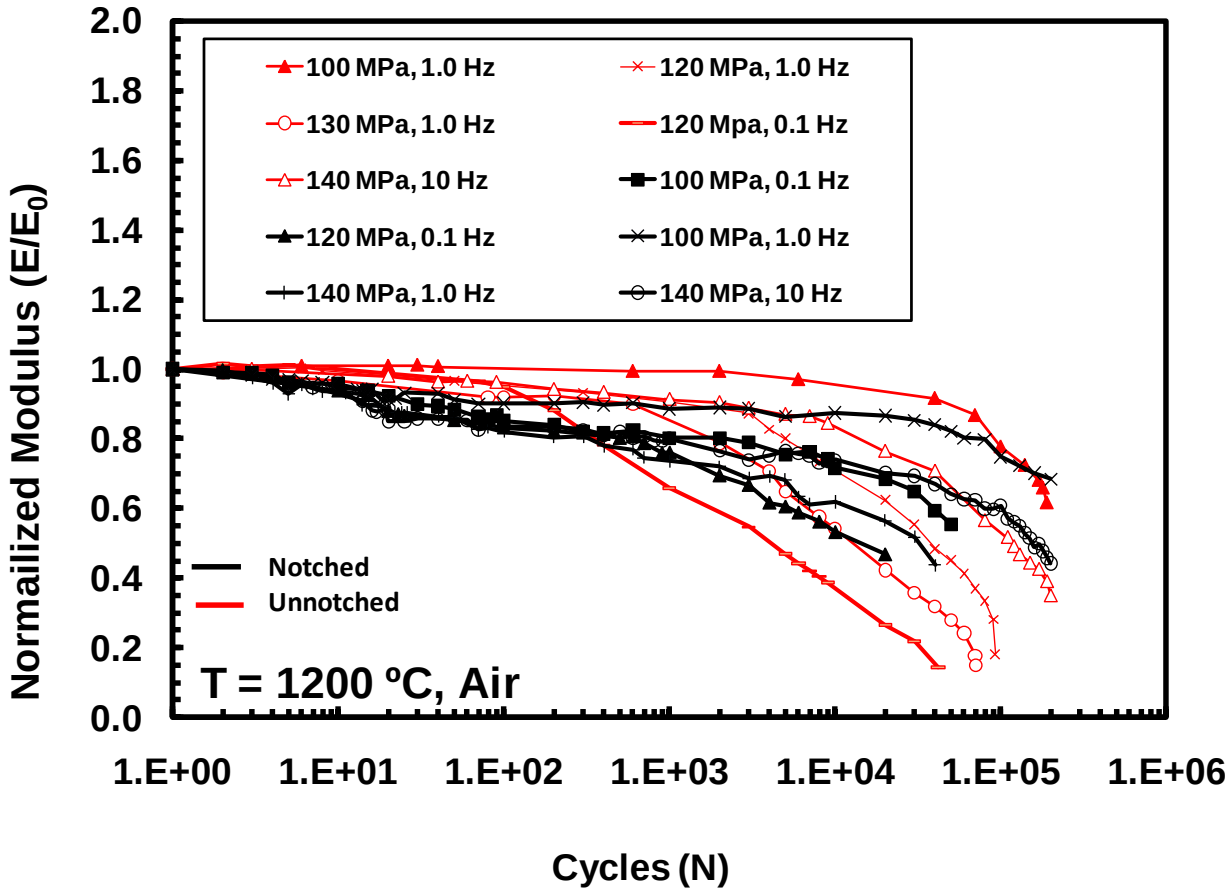

Figure 14: Normalized modulus vs. fatigue cycles for notched and unnotched Hi-Nicalon/PyC/HyprSiC composite at 1200°C in laboratory air. Data for unnotched Hi-Nicalon/PyC/HyprSiC from Delapasse [7].

Figure 15 presents accumulated strains as functions of fatigue cycles. A general trend of minor strain accumulation can be seen, with all specimens having accumulated strains below 0.35%. Strain accumulation appears to be dependent on both loading frequency and maximum fatigue stress level. The amount of accumulated strain increases with decreasing frequency (0.1 Hz) and increasing maximum fatigue stress level.

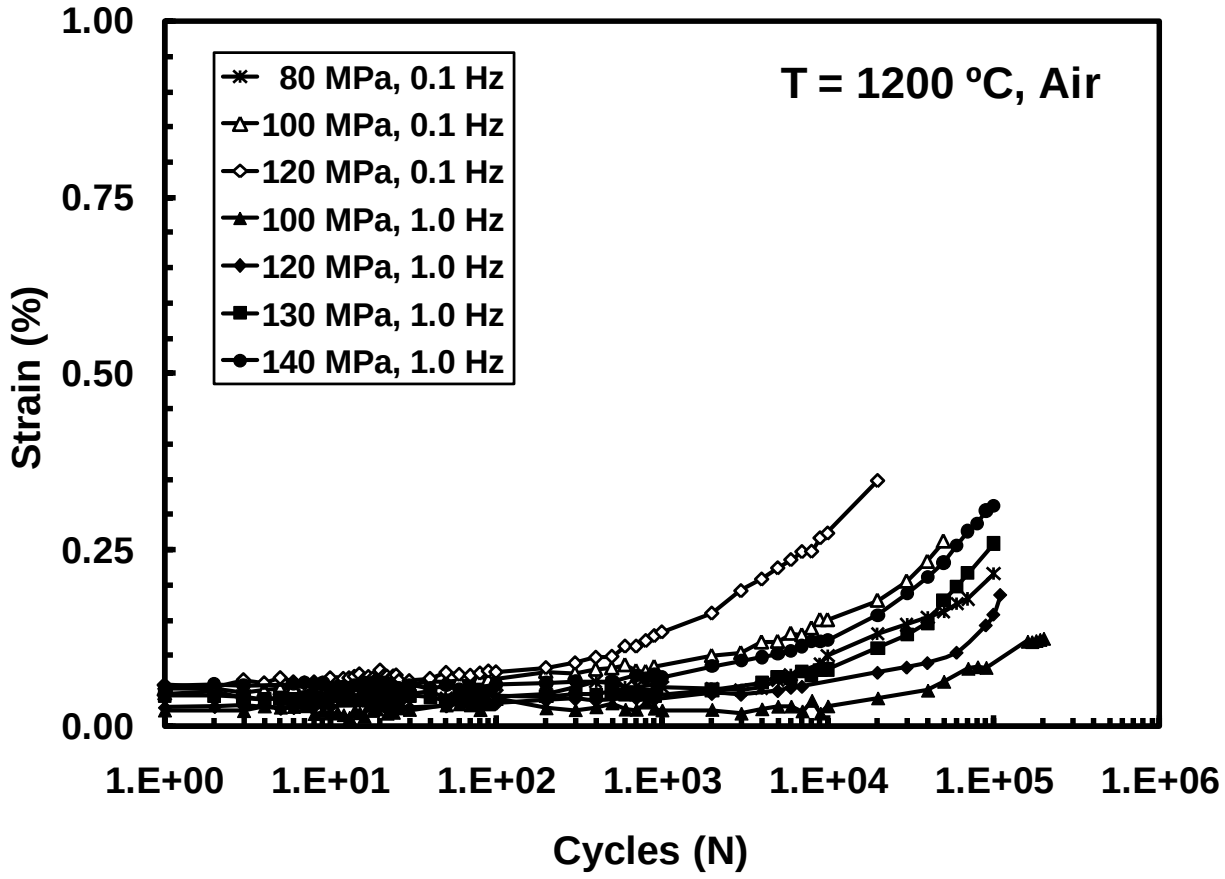

Figure 15: Accumulated strain vs. fatigue cycles for Hi-Nicalon/PyC/HyprSiC composite at 1200°C in laboratory air.

Strain accumulation with fatigue cycles is compared with the results obtained for the unnotched Hi-Nicalon/PyC/HyprSiC composite by Delapasse [7] in Figure 16. It can be seen from

this chart that the unnotched specimen exhibited much greater accumulated strains. Strains accumulated for the unnotched specimen range from 0.14% (100 MPa at 1.0 Hz) to 2.01% (120 MPa at 0.1 Hz) - much greater than those seen in the notched specimen. Loading frequency had a significant effect on accumulated strain in the unnotched specimen. Greater strains were realized in specimens tested at 0.1 Hz, compared to the strains of those tested at 1.0 Hz and 10 Hz- similar to the trends seen in the notched specimens.

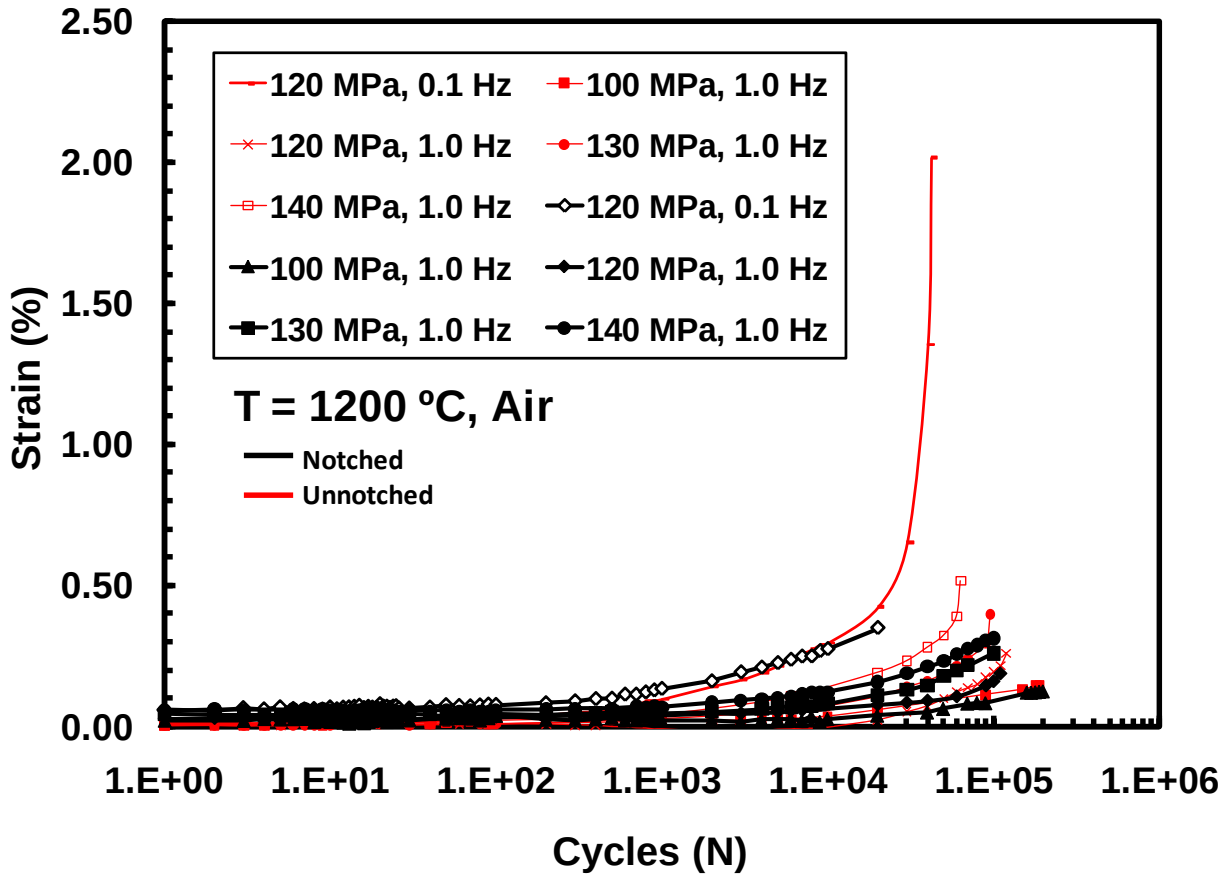

Figure 16: Accumulated strain vs. fatigue cycles for notched and unnotched Hi-Nicalon/PyC/HyprSiC composite at 1200°C in laboratory air. Data for unnotched Hi-Nicalon/PyC/HyprSiC from Delapasse [7].

Evolution of the hysteresis response of Hi-Nicalon/PyC/HyprSiC with fatigue cycles can be seen in Figure 17 and Figure 18 which show hysteresis stress-strain cyclic loops for tests conducted in laboratory air at 140 MPa, at 10 Hz and 1.0 Hz, respectively. Strain ratcheting, defined as progressive increase in accumulated strain with increasing cycles, continues throughout cycling. The initial modulus of cycle 2 is greater than that of all other cycles, showing a softening of the modulus and the onset of permanent strain with increasing cycles. The evolution of stress-strain hysteresis response of specimen 47 seen in Figure 17 shows modulus retention of 44% at run-out ($2x10^5$ cycles), while specimen 33, shown in Figure 18, has modulus retention of 35% at cycle 100,000. The permanent strain for the specimen tested at 140 MPa at 10 Hz (Figure 17) was roughly 0.09% while the permanent strain of the specimen tested at the same stress level at 1.0 Hz (Figure 18) had demonstrated a permanent strain of 0.19%.

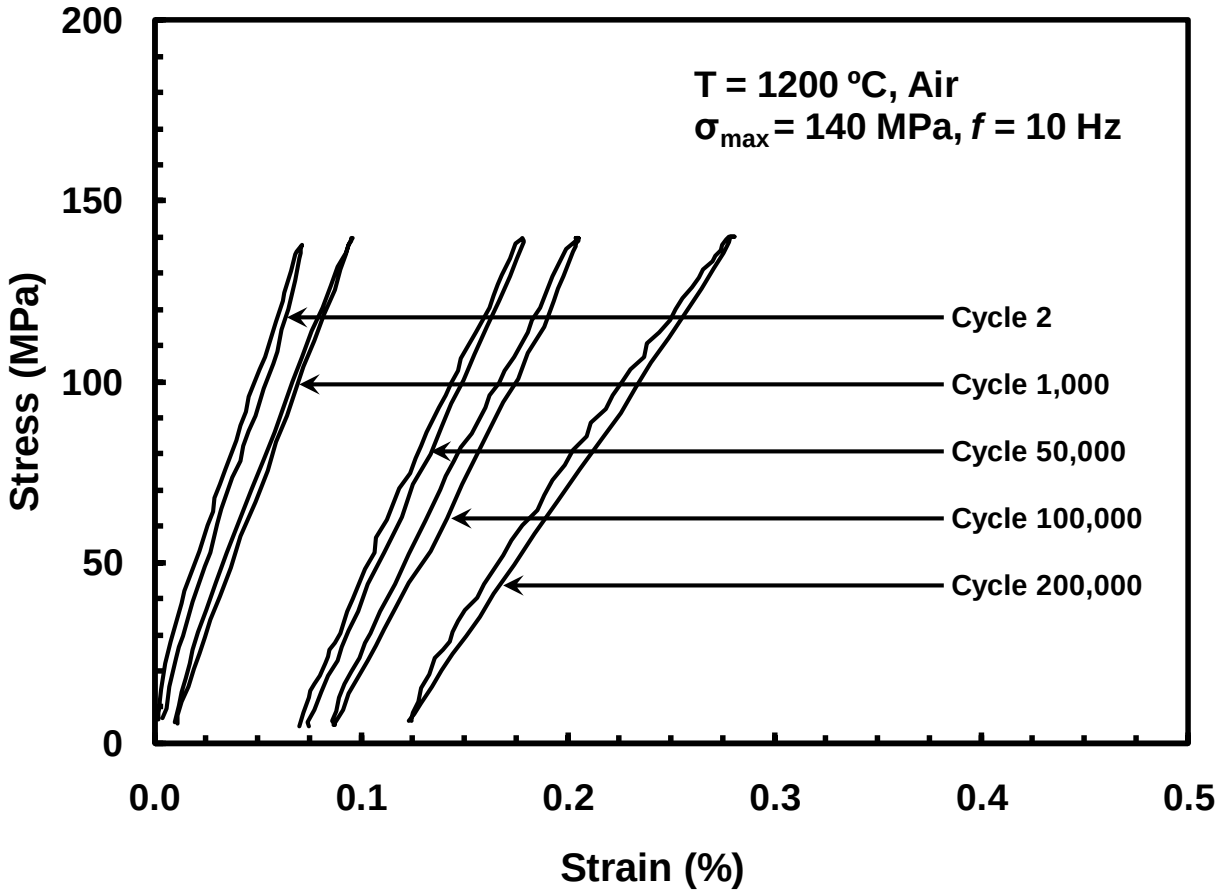

Figure 17: Evolution of stress-strain hysteresis response of Hi-Nicalon/PyC/HyprSiC composite at 1200°C in laboratory air at 10 Hz and σ_{max}= 140 MPa.

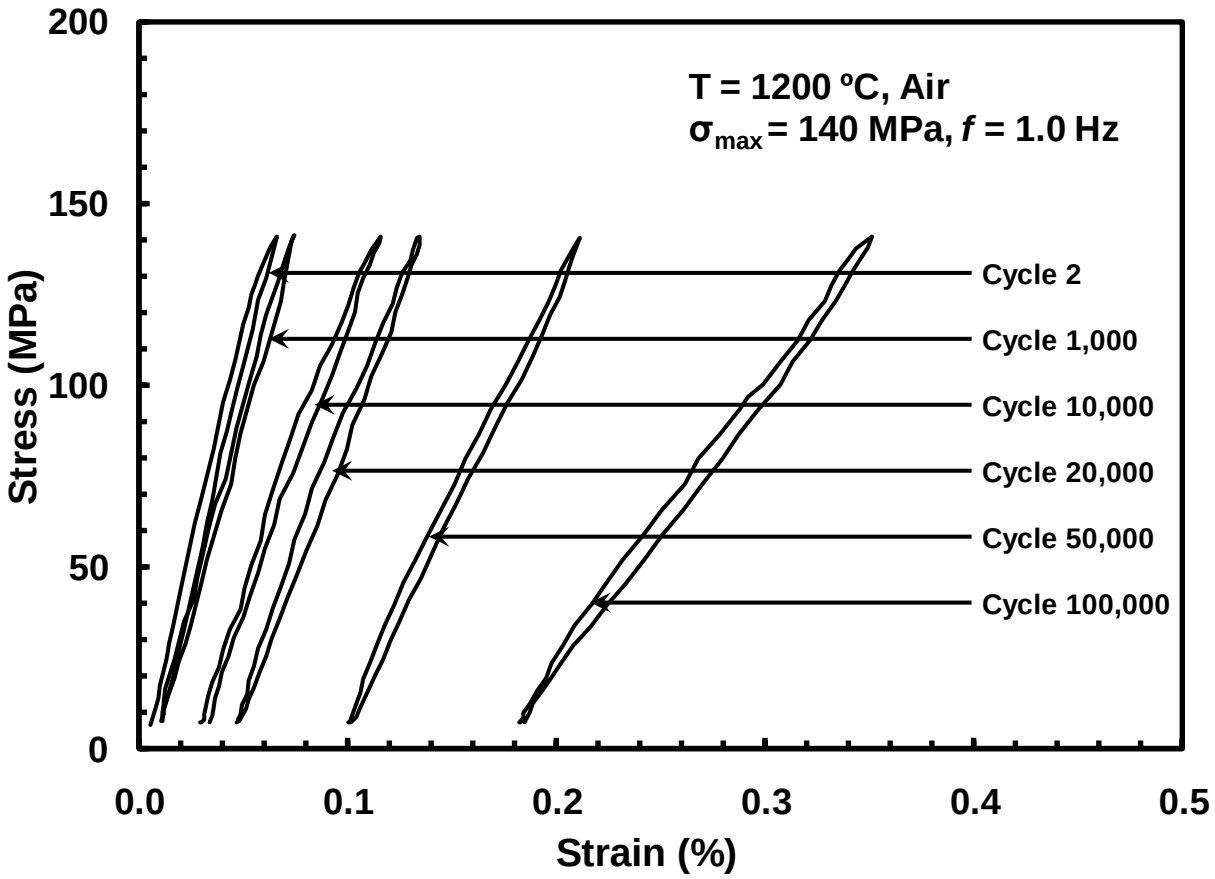

Figure 18: Evolution of stress-strain hysteresis response of Hi-Nicalon/PyC/HyprSiC composite at 1200°C in laboratory air at 1.0 Hz and σ_{max}= 140 MPa.

5.5 Tension-Tension Fatigue at 1200˚C in Steam

Tension-tension fatigue tests were also conducted at both 1.0 Hz and 0.1 Hz at 1200°C in steam. The same R-ratio of 0.05 was used. A run-out condition was achieved at all frequencies tested: at a stress level of 100 MPa at 1.0 Hz and 0.1 Hz and at a stress level of 140 MPa at 10 Hz. The maximum cyclic stress ranged from 100 MPa to 140 MPa (40 to 56% UTS) for all tests in steam. Table 8 presents the results of steam testing with air results included as a means of comparison. A stress versus cycles to failure (S-N) curve can be seen in Figure 19.

Table 8: Summary of fatigue results for Hi-Nicalon/PyC/HyprSiC composite at 1200°C in laboratory air and steam.

Test Environment	Max Stress (MPa)	Cycles to Failure (N)	Time to Failure (h)	Failure Strain (%)
Fatigue at 0.1Hz				
Laboratory Air	140	29,694	82.5	-
Laboratory Air	120	22,195	61.7	0.59
Laboratory Air	100	51,738	143.7	0.67
Laboratory Air	80	100,000[a]	277.8[a]	0.53
Steam	140	17,150	47.6	0.90
Steam	140	6,898[b]	19.2[b]	0.17
Steam	120	44,515	123.7	-
Steam	100	100,000[a]	277.8[a]	0.42
Fatigue at 1.0Hz				
Laboratory Air	140	43,116	12.0	0.78
Laboratory Air	140	105,421	29.3	0.99
Laboratory Air	130	104,000	28.9	0.77
Laboratory Air	120	113,522	31.5	0.98
Laboratory Air	120	77,575	21.5	0.82
Laboratory Air	100	200,000[a]	55.6[a]	0.26
Steam	140	74,280	20.6	0.88
Steam	130	115,050	32.0	0.61
Steam	120	177,335	49.3	1.09
Steam	100	200,000[a]	55.6[a]	0.17
Fatigue at 10 Hz				
Laboratory Air	140	200,000[a]	5.6[a]	0.45
Steam	140	26,485	0.7	-

[a]Run-out, faiulre of the specimen did not occur when test was terminated

[b]Failure of the specimen occurred due to equipment malfunction

Figure 19 shows S-N curves for the notched specimen tested in 1200°C laboratory air and steam at all frequencies tested.

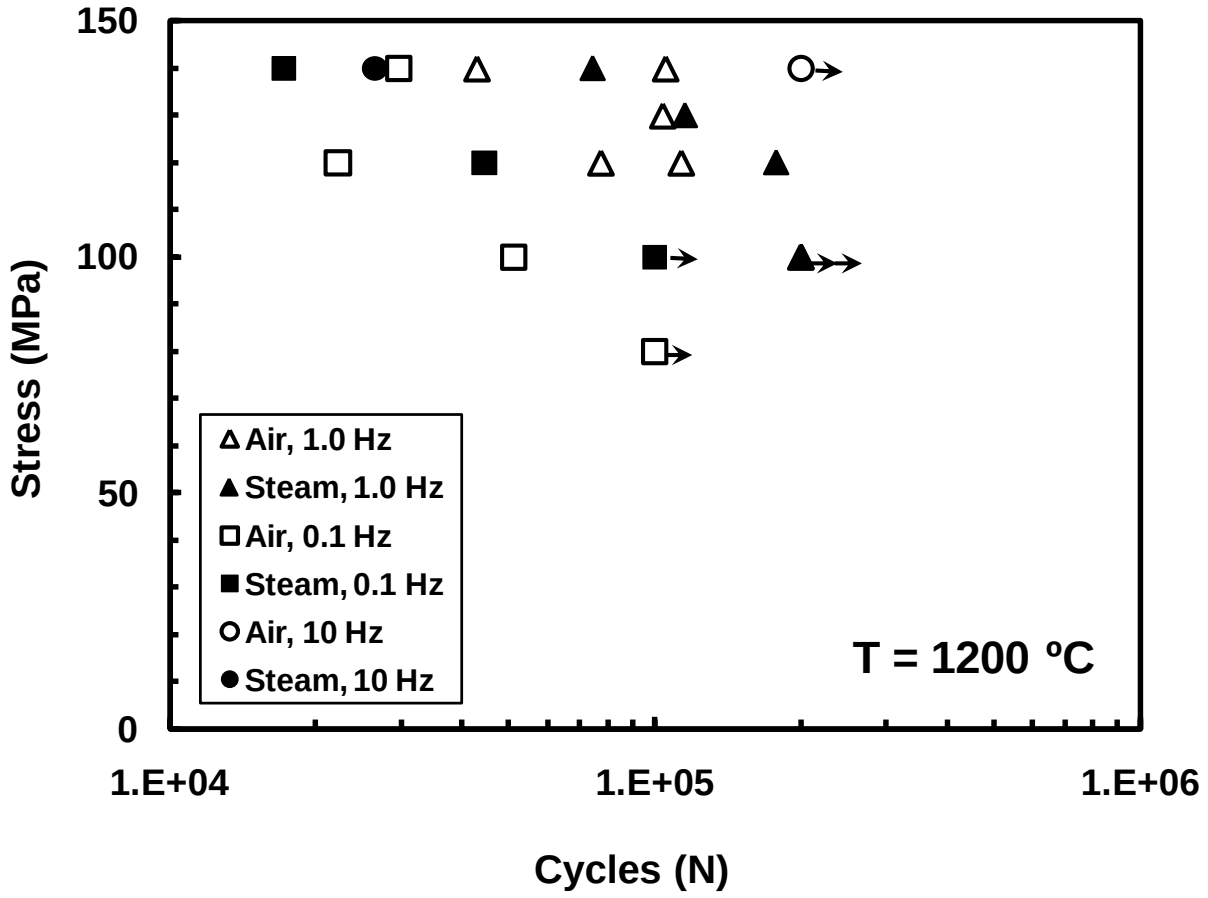

Figure 19: Fatigue S-N curves for Hi-Nicalon/PyC/HyprSiC composite at 1200°C in laboratory air and steam.

Figure 20 shows stress as a function of time-to-failure for tests conducted at 1200°C in both laboratory air and steam. It can be seen that specimens tested at 10 Hz in 1200°C air performed better than those in steam. Specimens tested in steam outperformed those tested in air at 0.1 Hz at stress levels of 100 MPa and 120 MPa and at 1.0 Hz at stress levels of 120 MPa and 130 MPa.

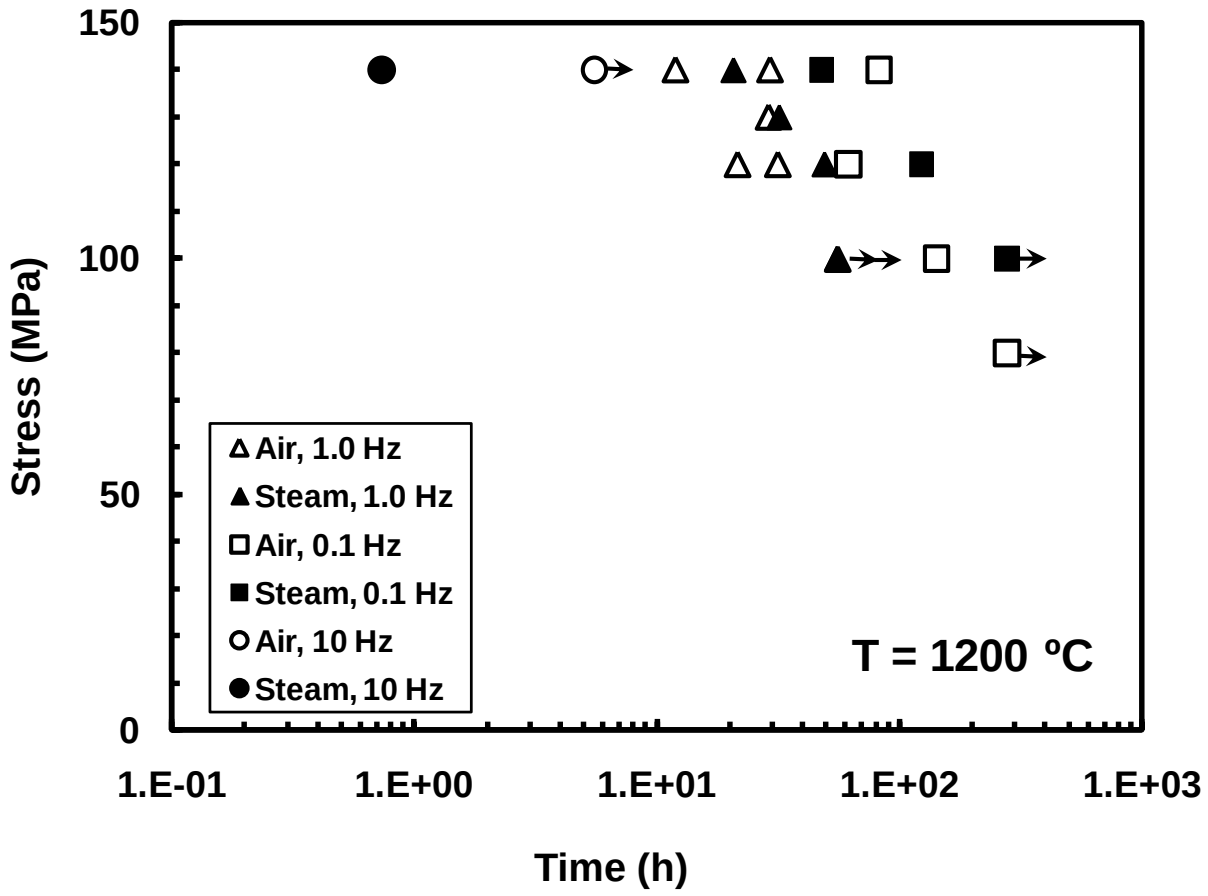

Figure 20: Fatigue stress vs. time to failure for Hi-Nicalon/PyC/HyprSiC composite at 1200°C in laboratory air and steam.

The fatigue results obtained for the notched Hi-Nicalon/PyC/HyprSiC composite at 1200°C in steam are compared to the unnotched results reported by Delapasse [7] in Figure 21. The notched specimens performed better in steam at 1.0 Hz, while the unnotched specimens outperformed the notched specimens in fatigue life overall at the other frequencies tested.

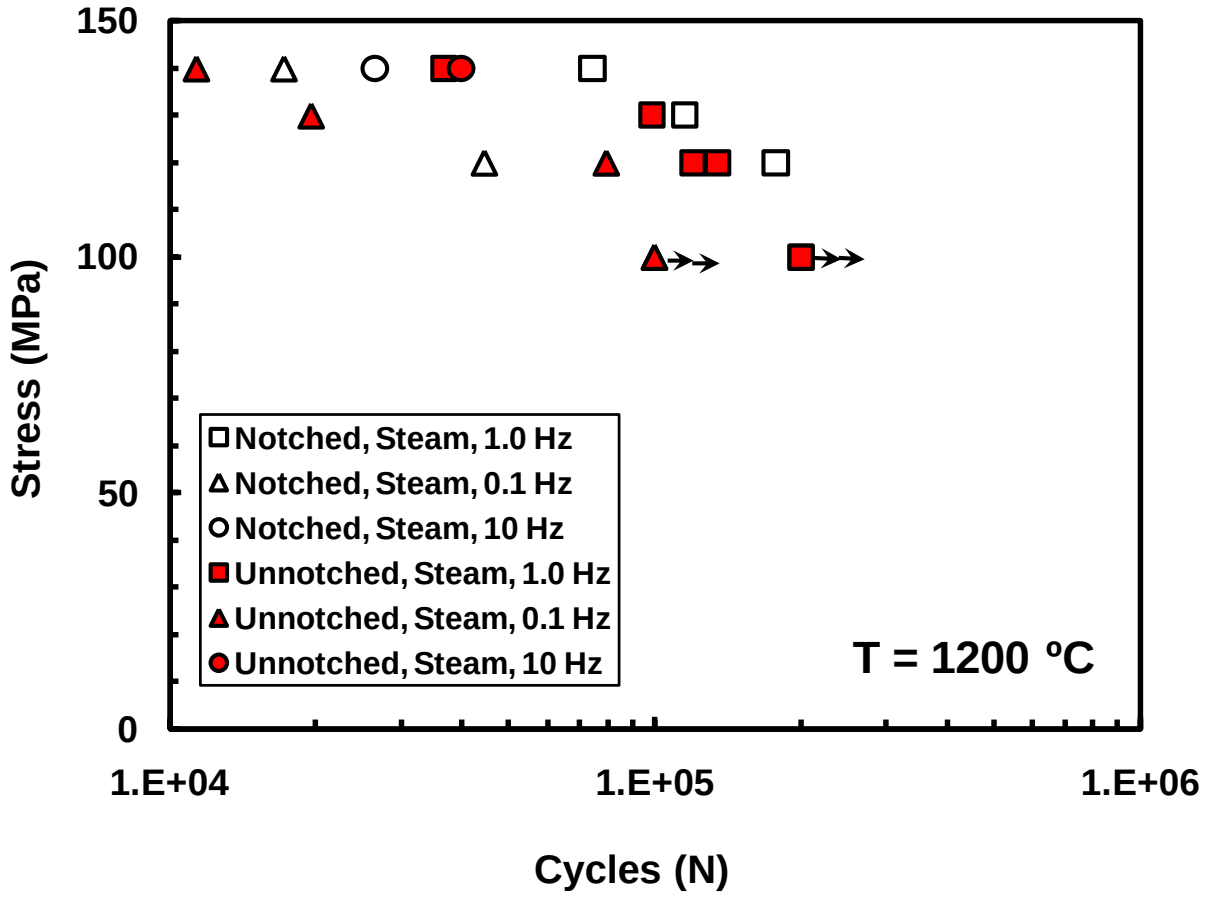

Figure 21: Fatigue S-N curves for notched and unnotched Hi-Nicalon/PyC/HyprSiC composite at 1200°C in steam. Data for unnotched Hi-Nicalon/PyC/HyprSiC from Delapasse [7].

Fatigue stress plotted as a function of time to failure is plotted in Figure 22 for both notched and unnotched specimens tested in 1200°C steam. This plot confirms the analysis above for the S-N curve.

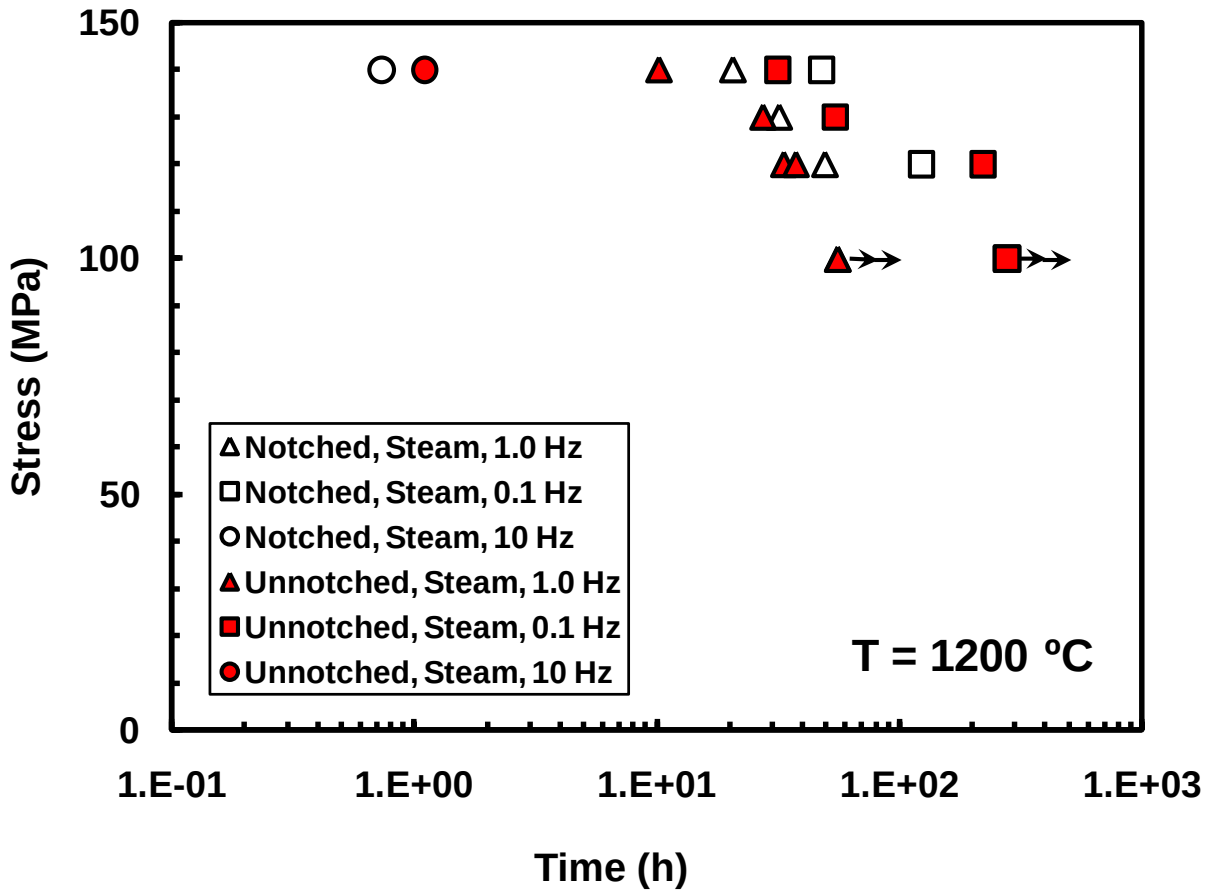

Figure 22: Fatigue stress vs. time to failure for notched and unnotched Hi-Nicalon/PyC/HyprSiC composite at 1200°C in steam. Data for unnotched Hi-Nicalon/PyC/HyprSiC from Delapasse [7].

The change in hysteresis modulus with fatigue cycling at 1200°C in steam was analyzed. Again, this is determined from the maximum and minimum stress-strain data points for a load cycle. Figure 23 presents elastic modulus as a function of fatigue cycles, where the modulus is normalized by that of the first cycle. All specimens tested show a decrease in modulus at failure suggesting fiber damage. Without damage to the fibers, the strains produced at given stress levels would remain the same (causing the modulus to remain the same). Since this is not the case, it is believed that there is damage to the fibers.

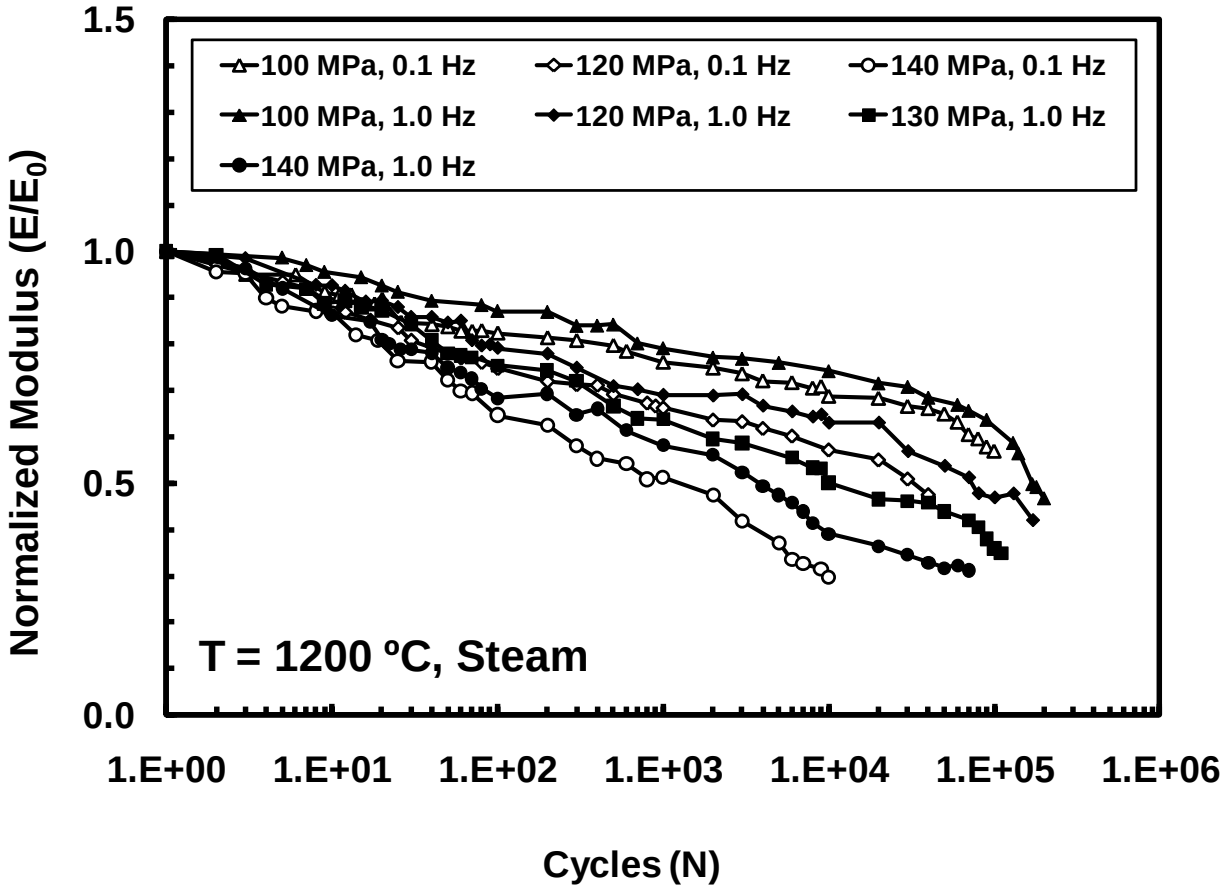

Figure 23: Normalized modulus vs. fatigue cycles for Hi-Nicalon/PyC/HyprSiC composite at 1200°C in steam.

Figure 24 shows the normalized modulus vs. fatigue cycles in both steam and air as a means of comparison. It can be seen that there is a greater loss in modulus in specimens tested in steam. The greatest reduction in modulus is realized by the specimen tested at 140 MPa at 0.1 Hz in steam with a loss of approximately 70% of modulus at failure. It can also be seen that specimens tested at maximum stress levels greater than the proportional limit experience the greatest loss in modulus.

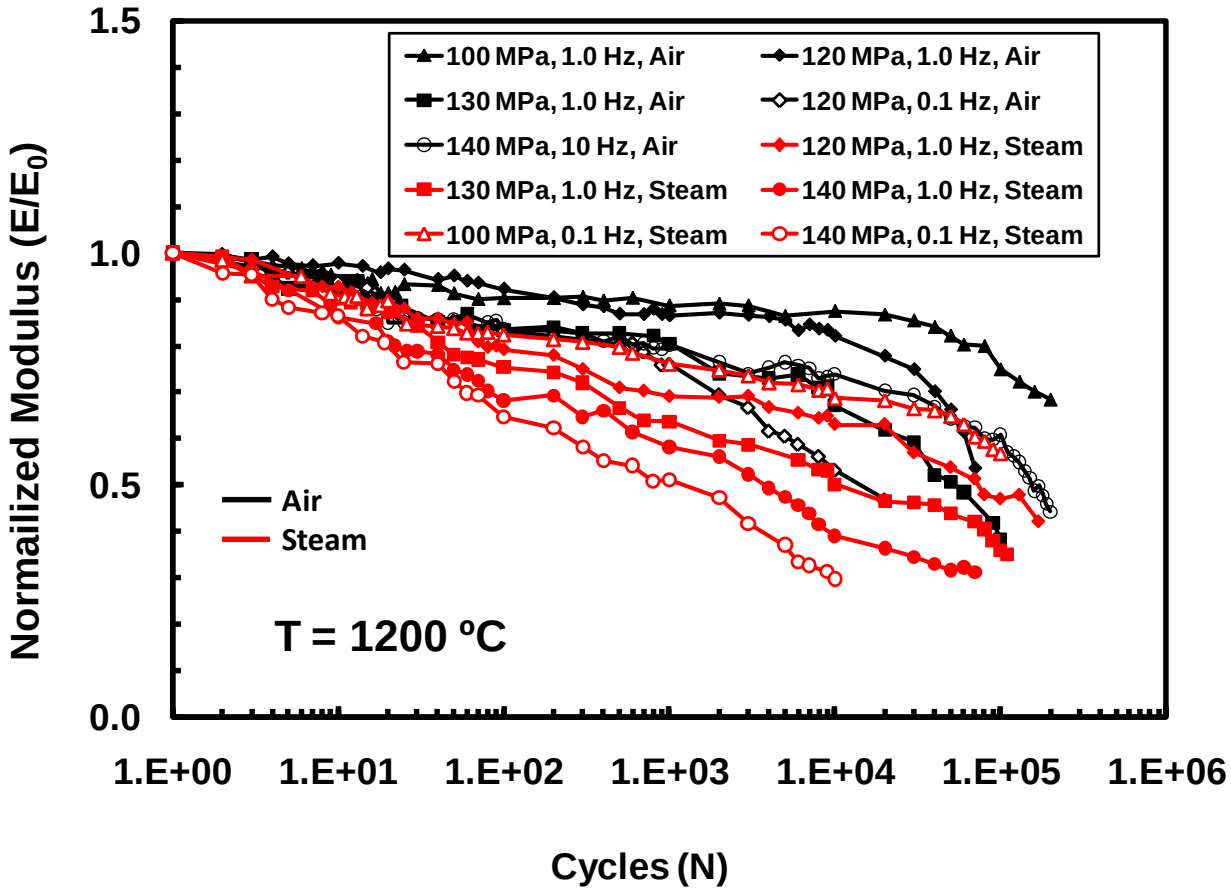

Figure 24: Normalized modulus vs. fatigue cycles for Hi-Nicalon/PyC/HyprSiC composite at 1200°C in air and steam.

Modulus evolution with fatigue cycles at 1200°C in steam was also compared to the unnotched Hi-Nicalon/PyC/HyprSiC composite by Delapasse [7] in Figure 25. Although both the notched and unnotched specimens showed a loss in modulus, the notched specimen showed a greater reduction when comparing similar cases (i.e. similar frequency and maximum stress level).

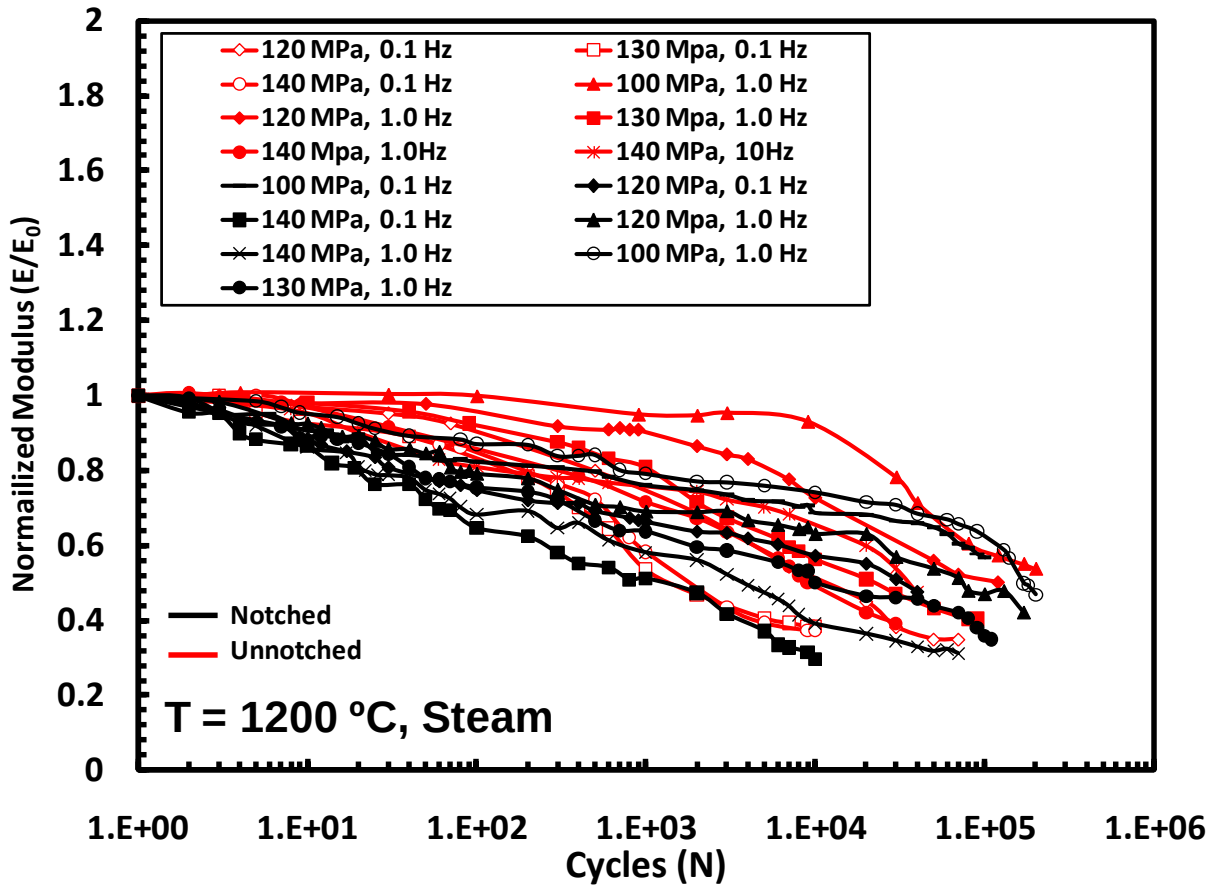

Figure 25: Normalized modulus vs. fatigue cycles for notched and unnotched Hi-Nicalon/PyC/HyprSiC composite at 1200°C in steam. Data for unnotched Hi-Nicalon/PyC/HyprSiC from Delapasse [7].

Figure 26 shows accumulated strain of all specimens tested at 1200°C in steam as a function of fatigue cycles. It can be seen that like the specimens tested in air, strain

accumulation increases with increasing maximum fatigue stress level and decreasing fatigue frequency. The maximum strain accumulated, however is much higher that of the specimens tested in air, as seen in Figure 27.

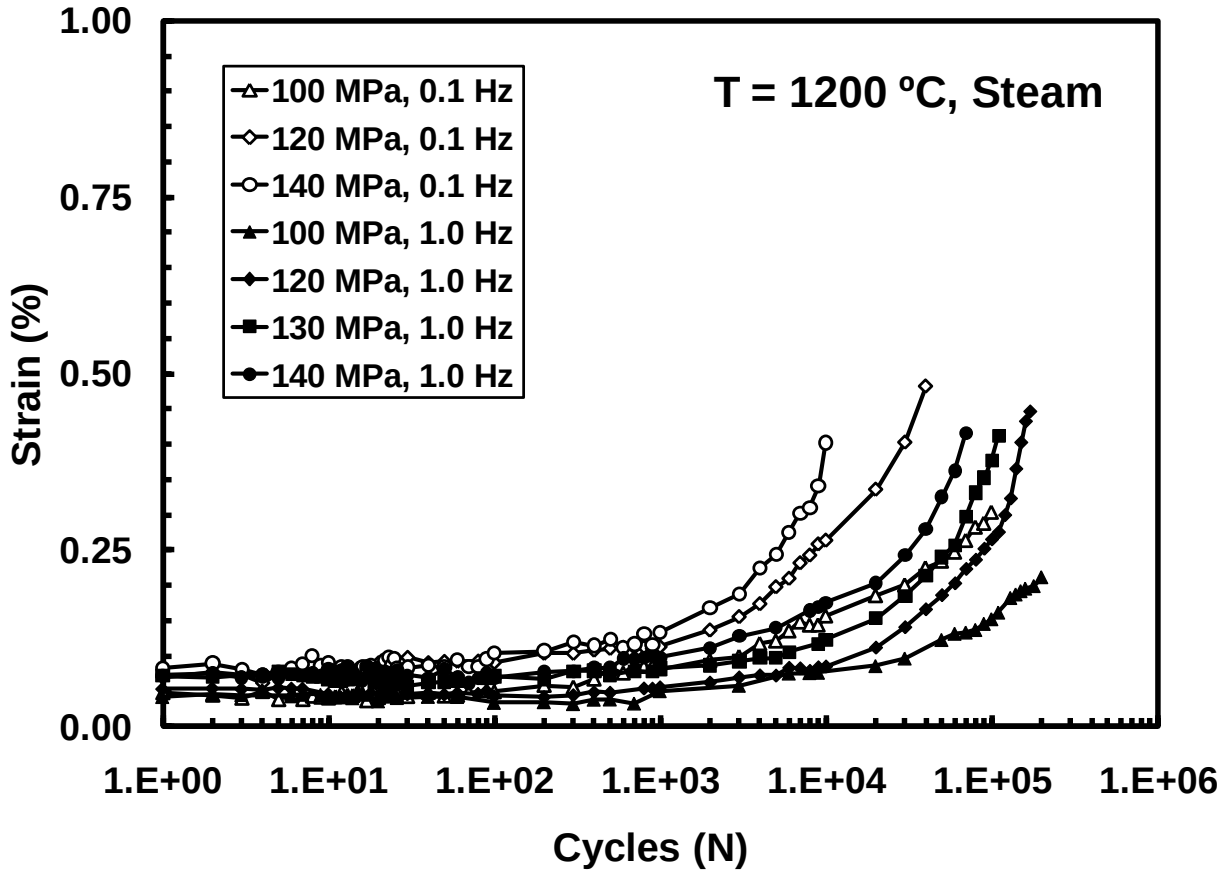

Figure 26: Accumulated strain vs. fatigue cycles for notched Hi-Nicalon/PyC/HyprSiC composite at 1200°C in steam.

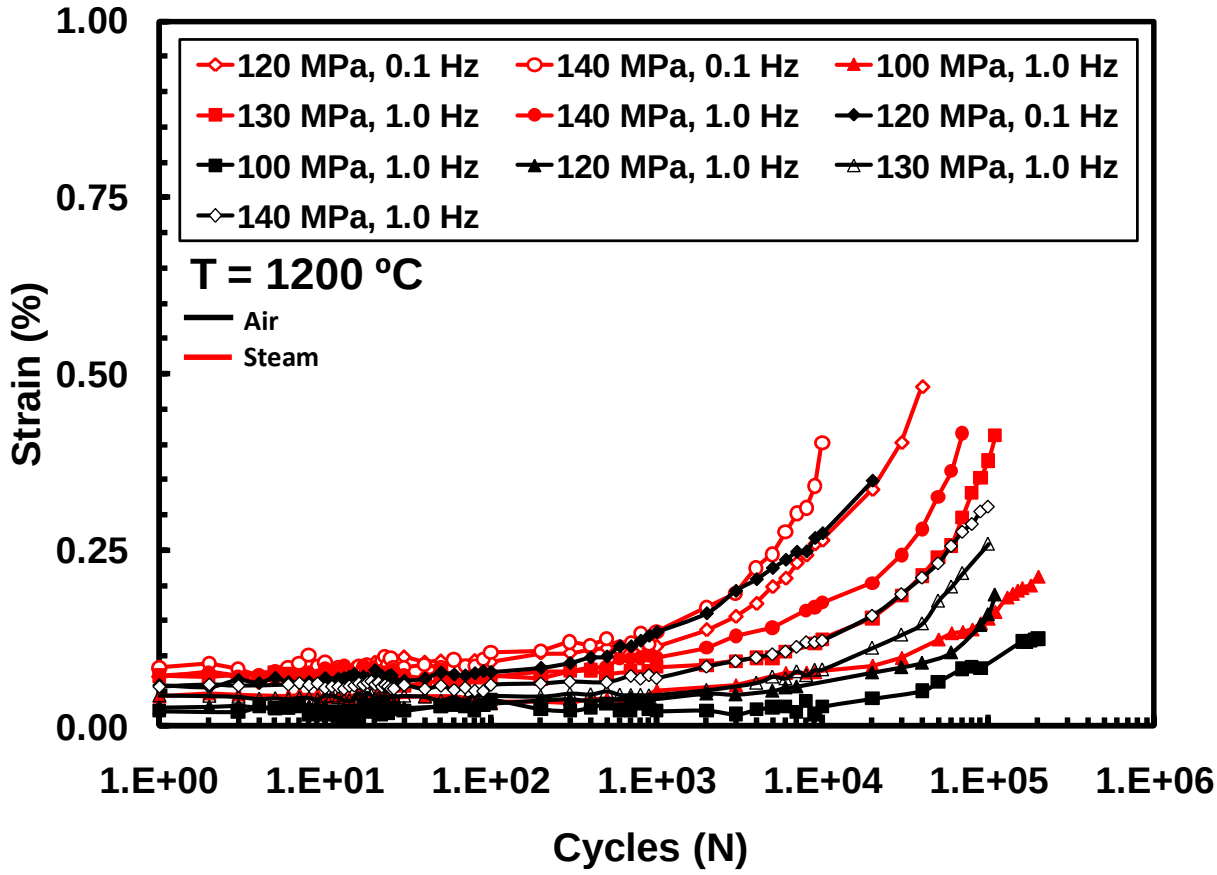

Figure 27: Accumulated strain vs. fatigue cycles for notched Hi-Nicalon/PyC/HyprSiC composite at 1200°C in air and steam.

Figure 28 presents a comparison of accumulated strain as a function of fatigue cycles of both the notched and unnotched specimens. It can be seen that the unnotched specimens achieved greater accumulated strains, while still demonstrating similar trends: increased strain accumulation with increasing maximum fatigue stress levels and decreasing fatigue frequency.

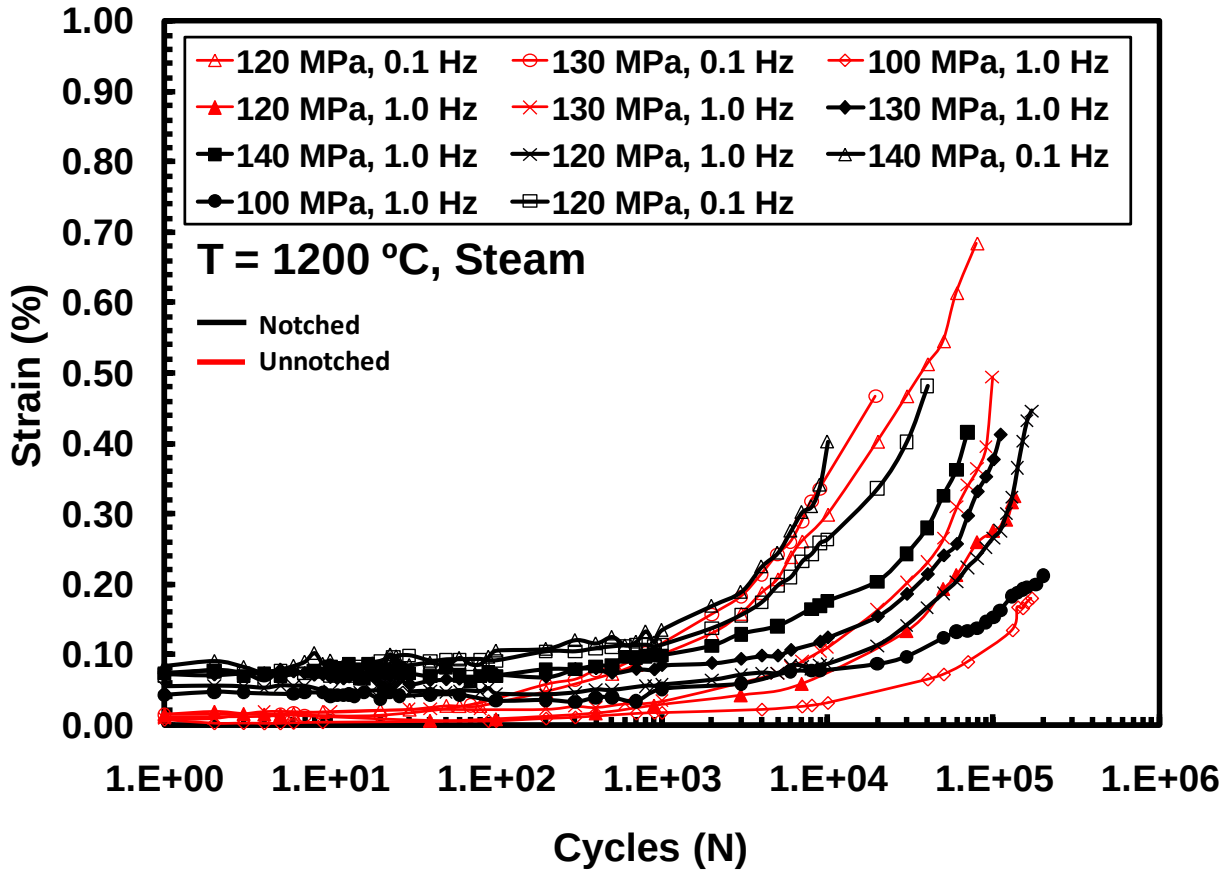

Figure 28: Accumulated strain vs. fatigue cycles for notched and unnotched Hi-Nicalon/PyC/HyprSiC composite at 1200°C in steam. Data for unnotched Hi-Nicalon/PyC/HyprSiC from Delapasse [7].

Figure 30 and Figure 29 show the evolution of the stress-strain hysteresis for two specimens tested at 140 MPa with a frequency of 1.0 Hz in steam and in air, respectively. These confirm the softening of the modulus with increasing cycles. The evolution of stress-strain hysteresis response seen in Figure 30 shows modulus retention of roughly 45% at cycle 100,000 for the specimen tested in steam, while the specimen tested in air, shown in Figure 29, has a modulus retention of nearly 35% at cycle 100,000. Permanent strain for the specimen tested at in steam (Figure 30) was roughly 0.26% while the permanent strain of the specimen tested in air

under similar test conditions (140 MPa, 1.0 Hz) shows a permanent strain of 0.18% in air. This suggests greater strains are accumulated in steam, than in air.

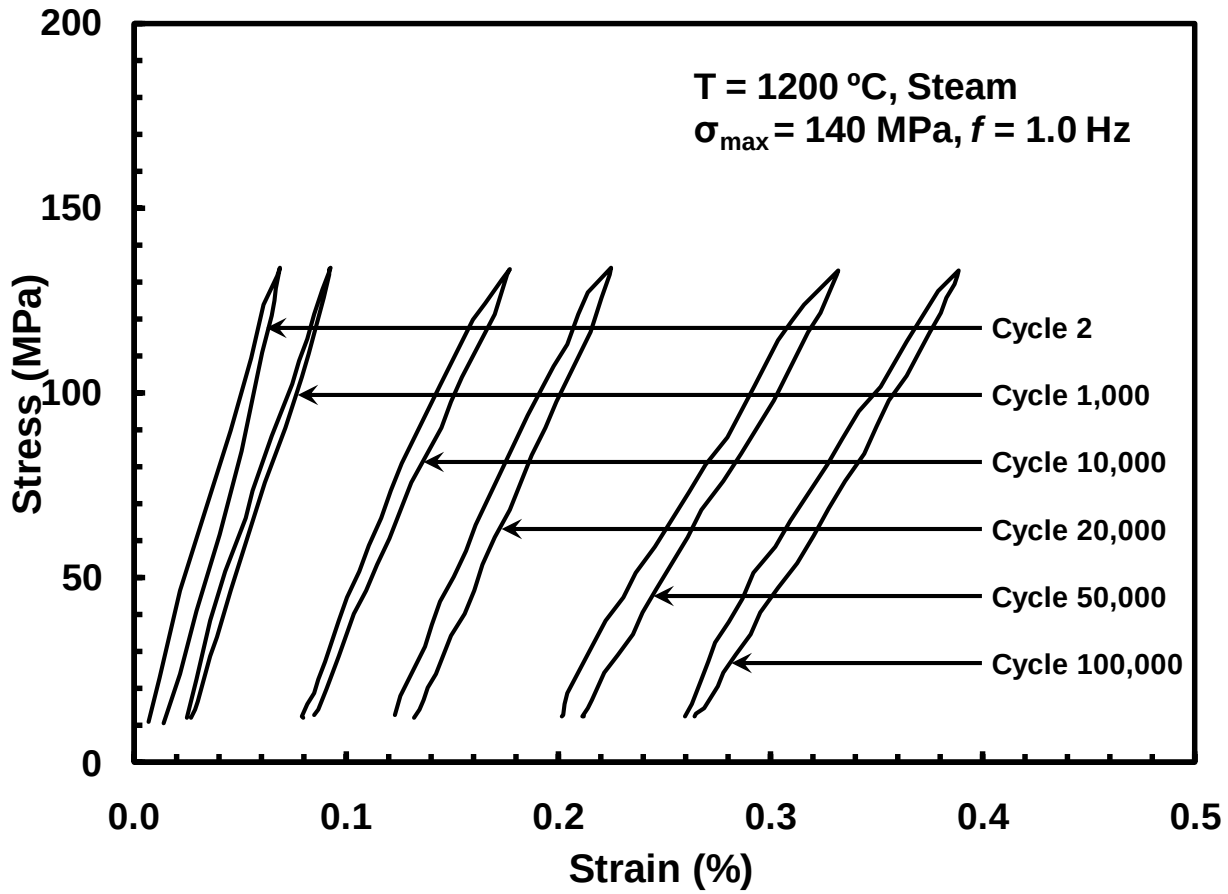

Figure 29: Evolution of stress-strain hysteresis response of Hi-Nicalon/PyC/HyprSiC composite at 1200°C in steam at 1.0 Hz and σ_{max}= 140 MPa.

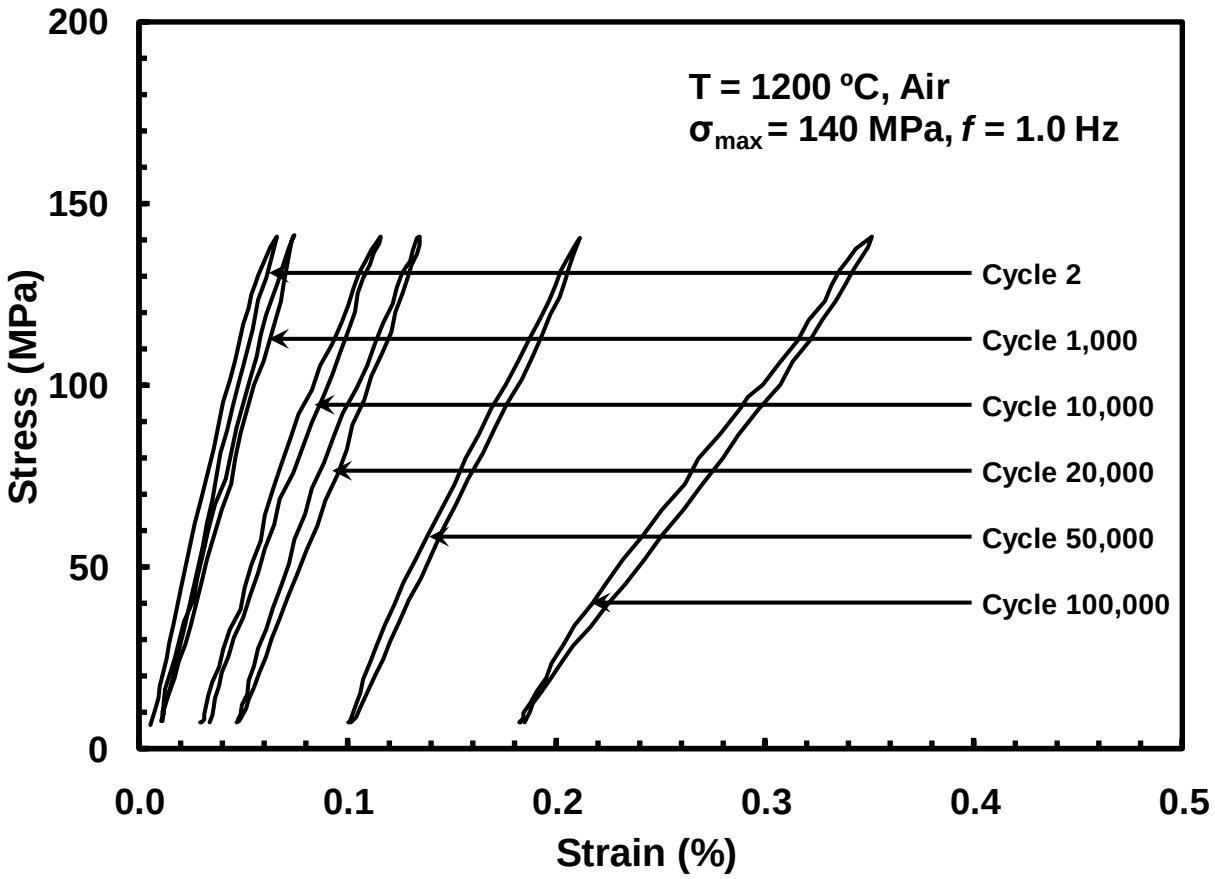

Figure 30: Evolution of stress-strain hysteresis response of Hi-Nicalon/PyC/HyprSiC composite at 1200°C in air at 1.0 Hz and σ_{max}= 140 MPa.

5.6 Effect of Prior Fatigue on Tensile Properties and Tensile Stress-Strain Behavior

All specimens achieving run-out were subjected to a monotonic tension to failure test upon completion of fatigue cyclic loading to determine retained material properties. Retained strength and stiffness values are shown in Table 9. All specimens lost at least 13% of their strength. Strength retention was calculated by comparing the failure strength of the run-out specimen to the ultimate tensile strength (UTS) of the panel (derived from the initial

tension tests of the as-processed material) that the specimen was pulled from. For pre-fatigued tensile tests in air at 1200°C, 73.8% of strength was retained at 0.1 Hz and 80 MPa, 81% of strength was retained at 1.0 Hz and 100 MPa, and 79.7% of strength was retained at 10 Hz and 140 MPa. For pre-fatigued tensile tests in steam at 1200°C, 82.1% of strength was retained at 0.1 Hz and 100 MPa, 87% of strength was retained at 1.0 Hz and 100 MPa, and no run-out condition was achieved at 10 Hz. For tests at 0.1 Hz and 1.0 Hz, the specimens in steam retained more of their strength. All specimens except the specimen tested at 80 MPa and 0.1 Hz in 1200°C laboratory air showed a reduction in modulus.

Table 9: Retained tensile properties of Hi-Nicalon/PyC/HyprSiC specimens subjected to prior fatigue in laboratory air and steam at 1200°C.

Fatigue Stress (MPa)	Fatigue Environment	Retained Strength (MPa)	Strength Retention (%)	Retained Modulus (GPa)	Modulus Retention (%)	Strain at Failure (%)
Prior Fatigue at 0.1 Hz						
80	Laboratory Air	186.9	73.8	406.2	179.7	0.293
100	Steam	213.2	82.1	152.7	61.3	0.423
Prior Fatigue at 1.0 Hz						
100	Laboratory Air	210.3	81.0	209.5	84.1	0.259
100	Steam	211.4	87.0	205.4	91.7	0.174
Prior Fatigue at 10 Hz						
140	Laboratory Air	193.7	79.7	78.2	34.9	0.447

The tensile stress-strain curves of both the as-processed and pre-fatigued specimens tested in air and steam are presented in Figure 31 and Figure 32, respectively. The specimens tested at 0.1 Hz and 1.0 Hz achieving run-out demonstrate a similar bi-linear appearance as the as-processed material with an apparent proportional limit. The curve showing the 10 Hz pre-

fatigued specimen in Figure 31 does not show a clear departure from linearity, assumingly caused by significant damage to the matrix. This observation also explains the great loss in modulus. It is interesting to note the loss in modulus and strength due to fiber damage in the specimen. It is hypothesized that subcritical crack growth in the fibers caused failure of the specimens by providing a pathway for the oxidative environment to attack the fiber, causing the observed loss of strength in specimens achieving run-out.

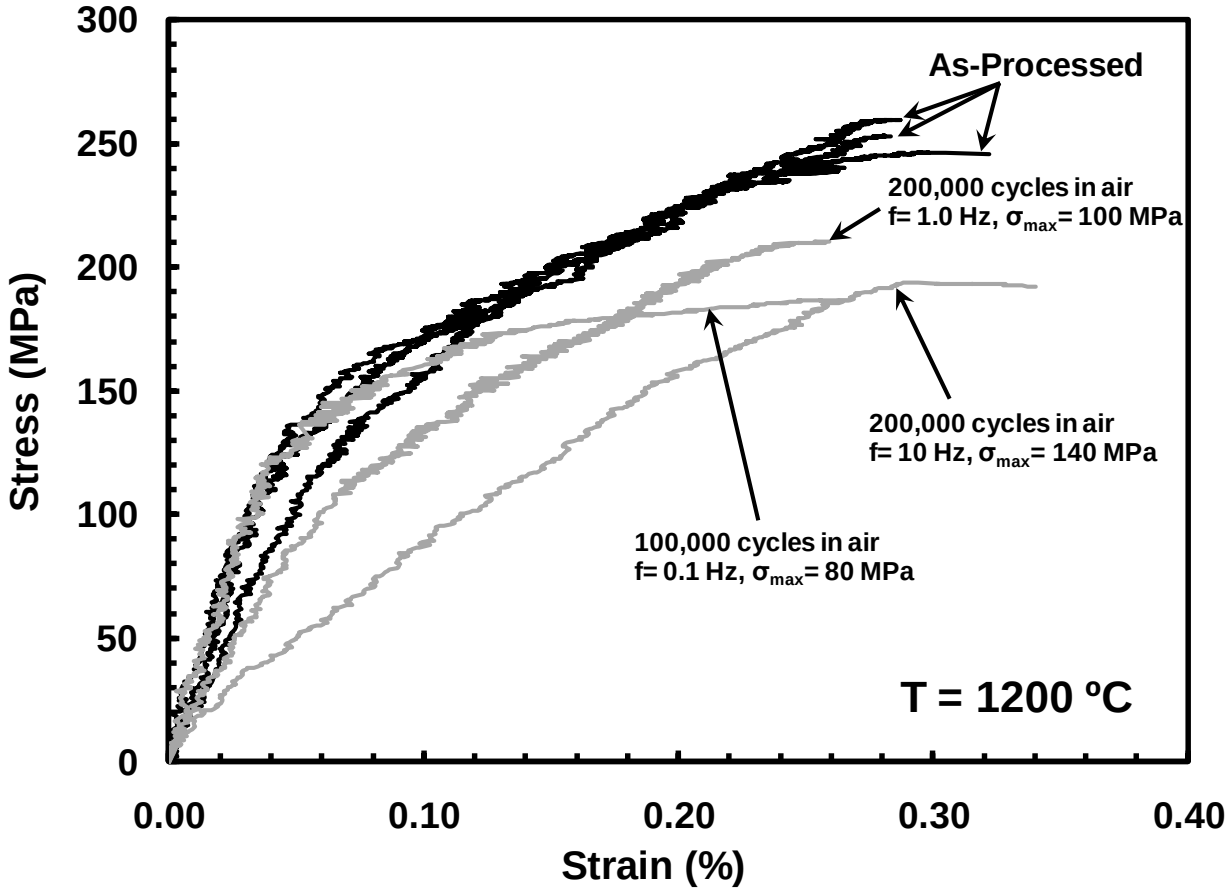

Figure 31: Tensile stress-strain curves obtained for Hi-Nicalon/PyC/HyprSiC specimens subjected to prior fatigue in air at 1200°C. Tensile stress-strain curves for the as-processed specimens are shown for comparison.

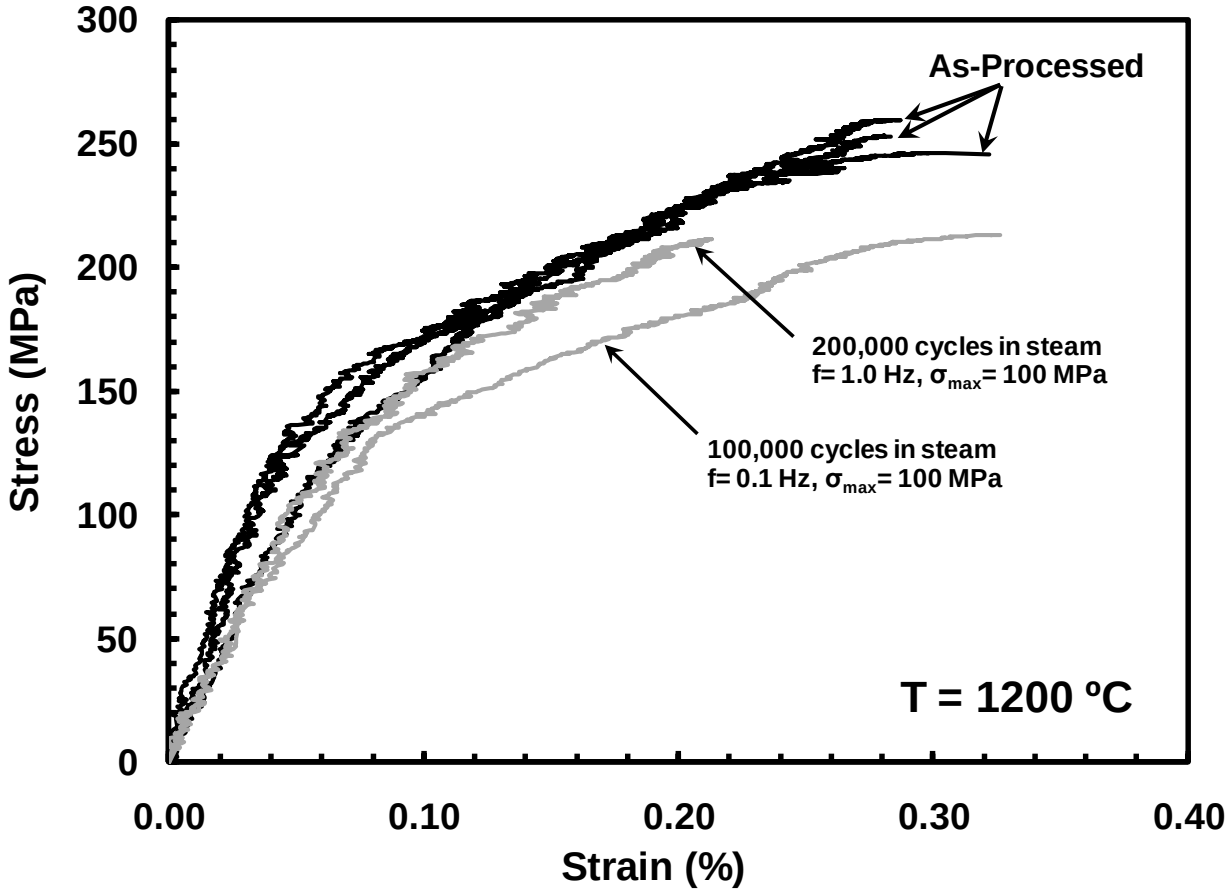

Figure 32: Tensile stress-strain curves obtained for Hi-Nicalon/PyC/HyprSiC specimens subjected to prior fatigue in steam at 1200°C. Tensile stress-strain curves for the as-processed specimens are shown for comparison.

The retained tensile properties of the notched specimen were compared to those of the unnotched specimen reported by Delapasse [7] in Table 10. The notched specimen had greater strength retention at all frequencies tested. The notched specimen also had greater modulus retention at 1.0 Hz, but lower modulus retention at both 0.1 Hz and 10 Hz

Table 10: Retained tensile properties for notched and unnotched Hi-Nicalon/PyC/HyprSiC specimens subjected to prior fatigue in laboratory air and steam at 1200°C. Data for unnotched Hi-Nicalon/PyC/HyprSiC from Delapasse [7].

Fatigue Stress (MPa)	Fatigue Environment	Retained Strength (MPa)	Strength Retention (%)	Retained Modulus (GPa)	Modulus Retention (%)	Strain at Failure (%)
Prior Fatigue at 0.1 Hz						
Notched Hi-Nicalon/PyC/HyprSiC						
80	Laboratory Air	186.9	73.8	406.2	179.7	0.293
100	Steam	213.2	82.1	152.7	61.3	0.423
Unnotched Hi-Nicalon/PyC/HyprSiC						
100	Steam	229.4	74.8	129	62.5	0.604
Prior Fatigue at 1.0 Hz						
Notched Hi-Nicalon/PyC/HyprSiC						
100	Laboratory Air	210.3	81.0	209.5	84.1	0.259
100	Steam	211.4	87.0	205.4	91.7	0.174
Unnotched Hi-Nicalon/PyC/HyprSiC						
100	Laboratory Air	130	42.4	171.5	83.1	0.196
100	Steam	183.1	59.7	141.6	68.6	0.345
Prior Fatigue at 10 Hz						
Notched Hi-Nicalon/PyC/HyprSiC						
140	Laboratory Air	193.7	79.7	78.2	34.9	0.447
Unnotched Hi-Nicalon/PyC/HyprSiC						
140	Laboratory Air	186.7	60.9	91.0	44.1	0.374

The retained tensile stress-strain curves for both the notched and unnotched specimens subjected to prior fatigue tested in air and steam can be found in Figure 33 and Figure 34, respectively. It can be seen that both the notched and unnotched specimens exhibit very analogous behavior for similar test conditions (i.e. the notched and unnotched specimens achieving run-out at 10 Hz in air have a severe loss in elastic modulus and achieve the greatest failure strains of all specimens reaching run-out. The unnotched specimens demonstrate a

greater retained failure strain at all frequencies tested in the steam environment).

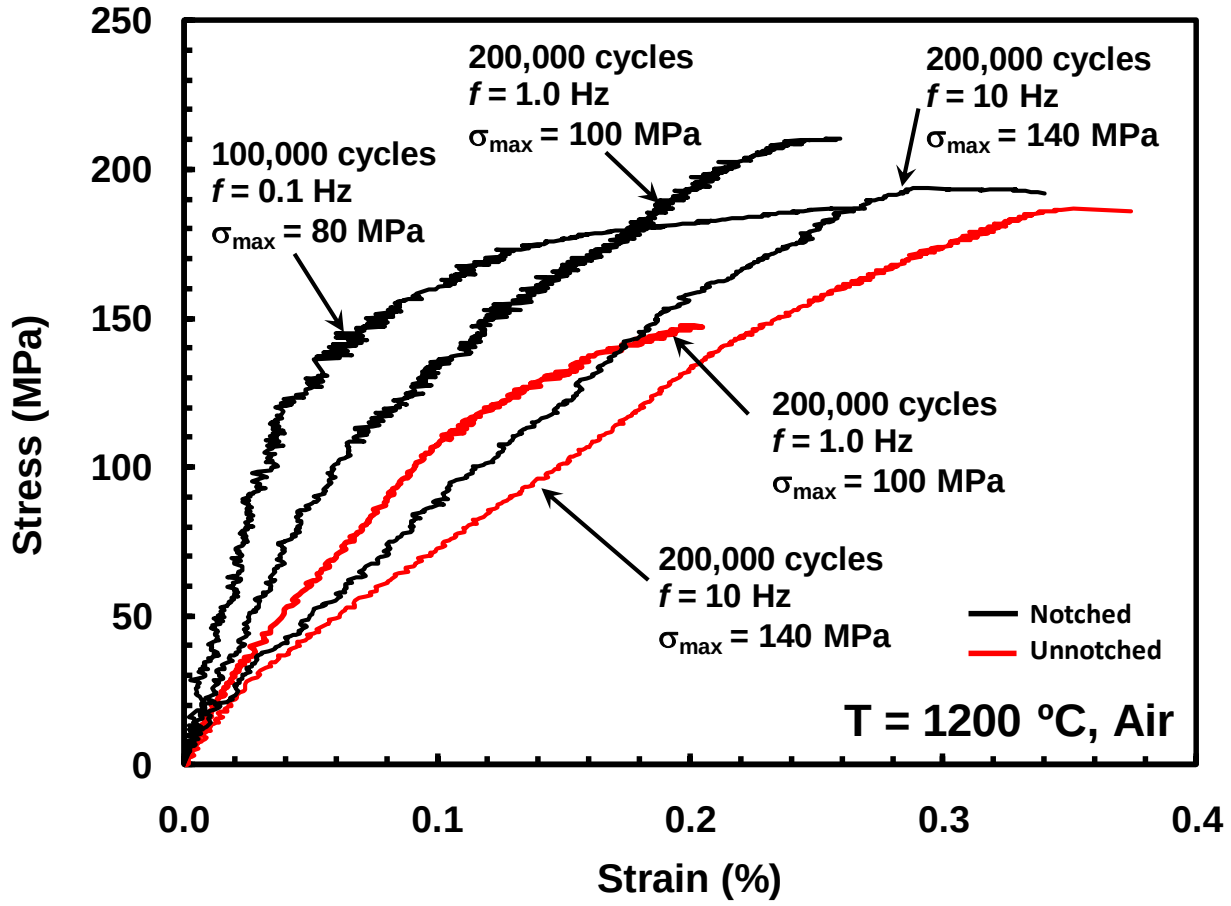

Figure 33: Tensile stress-strain curves obtained for notched and unnotched Hi-Nicalon/PyC/HyprSiC specimens subjected to prior fatigue in air at 1200°C. Data for and unnotched Hi-Nicalon/PyC/HyprSiC from Delapasse [7].

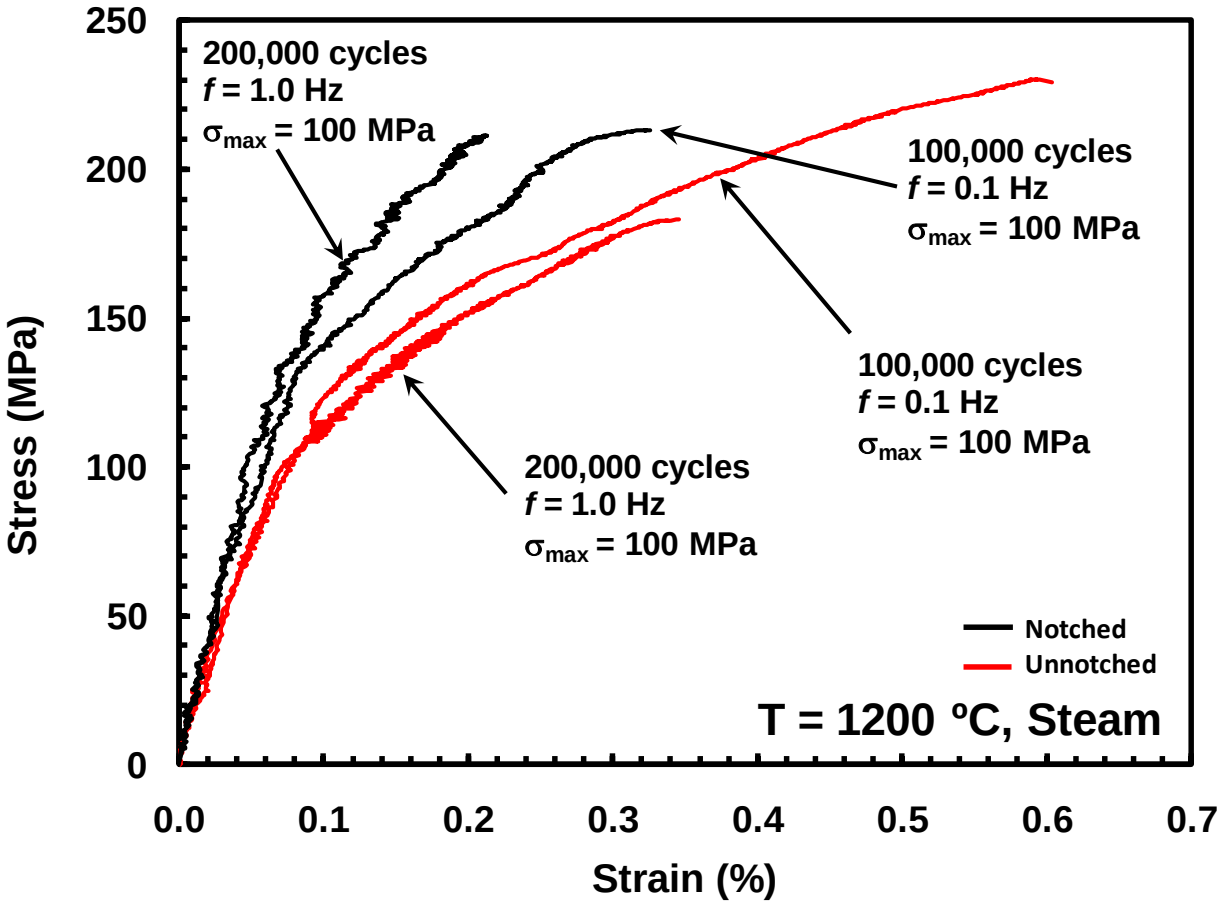

Figure 34: Tensile stress-strain curves obtained for notched and unnotched Hi-Nicalon/PyC/HyprSiC specimens subjected to prior fatigue in air at 1200°C. Data for and unnotched Hi-Nicalon/PyC/HyprSiC from Delapasse [7].

5.7 Microstructural Characterization

The following sections provide a qualitative analysis of the fracture surfaces of select Hi-Nicalon/PyC/HyprSiC failed specimens accomplished using an optical microscope as well as an SEM.

5.7.1 Microstructure of the As-Processed Material

Sections were cut from each of the three panels tested and examined in the SEM. Each of the panels demonstrated similar microstructural characteristics as seen in Figure 35 through Figure 37. Voids between fiber tows can be found throughout each of the three panels tested (Figure 36D). The layered matrix (Figure 35A) as well as the dual-layered PyC and B4C fiber coating (Figure 37D) can also be seen in each of the three panels' SEM micrographs.

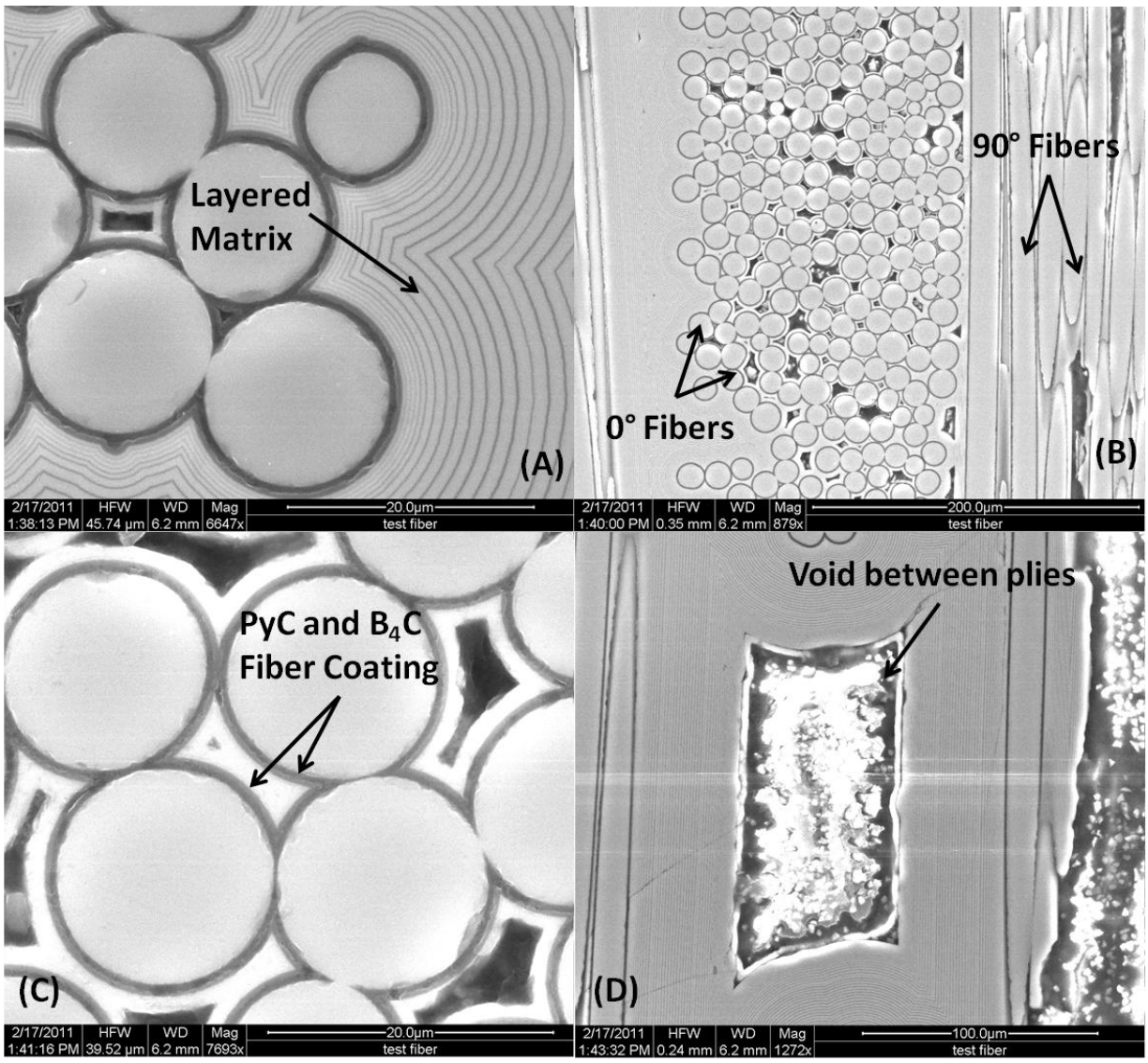

Figure 35: SEM micrographs of the as-processed material from Panel 1 showing: A) the layered matrix structure, B) 0° and 90° fibers, C) duel-layered PyC and B_4C fiber coating, D) a large void between plies.

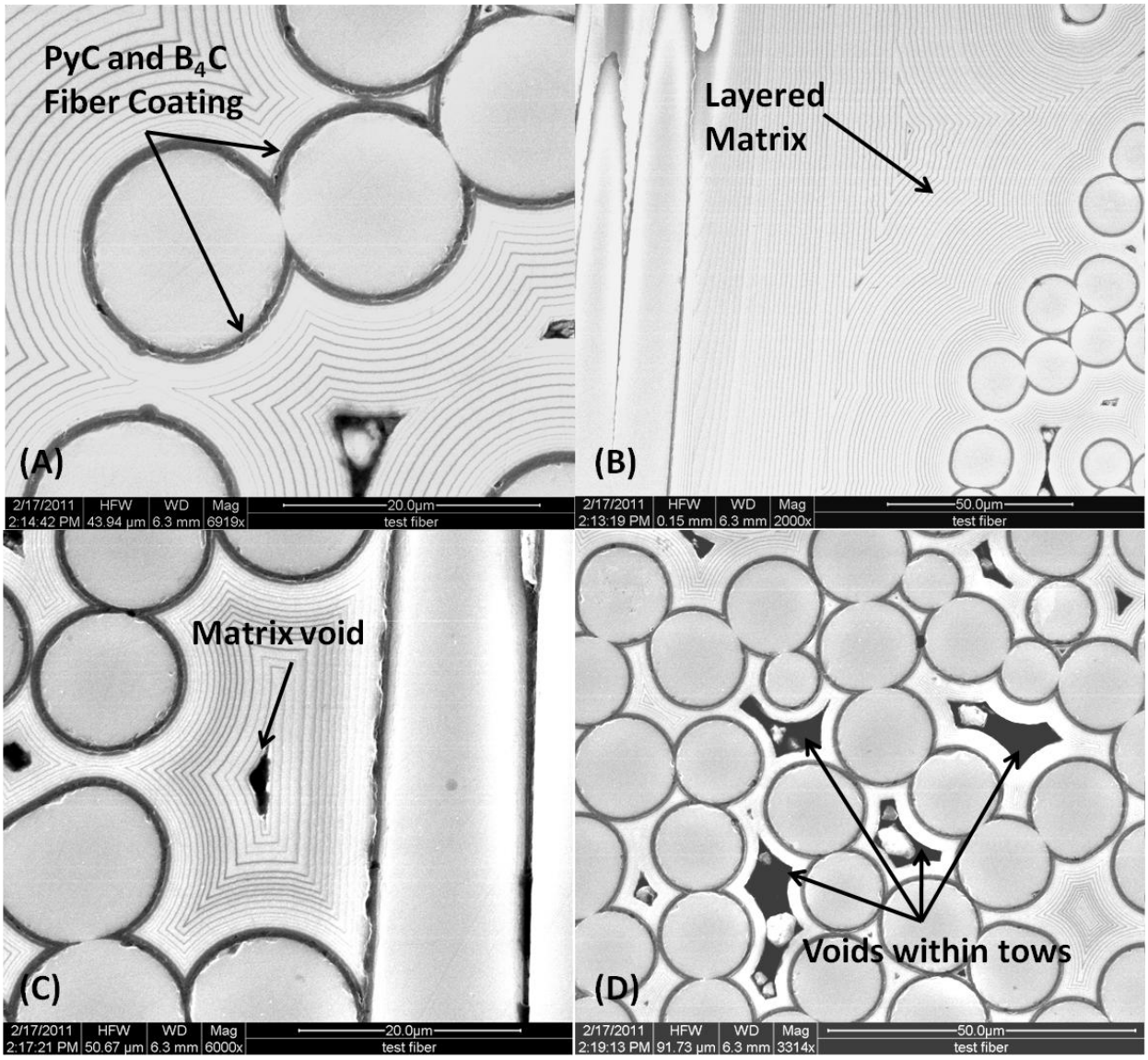

Figure 36: SEM micrographs of the as-processed material from Panel 3 showing: A) duel-layered PyC and B_4C fiber coating, B) the layered matrix, C) a matrix void, D) voids within fiber tows.

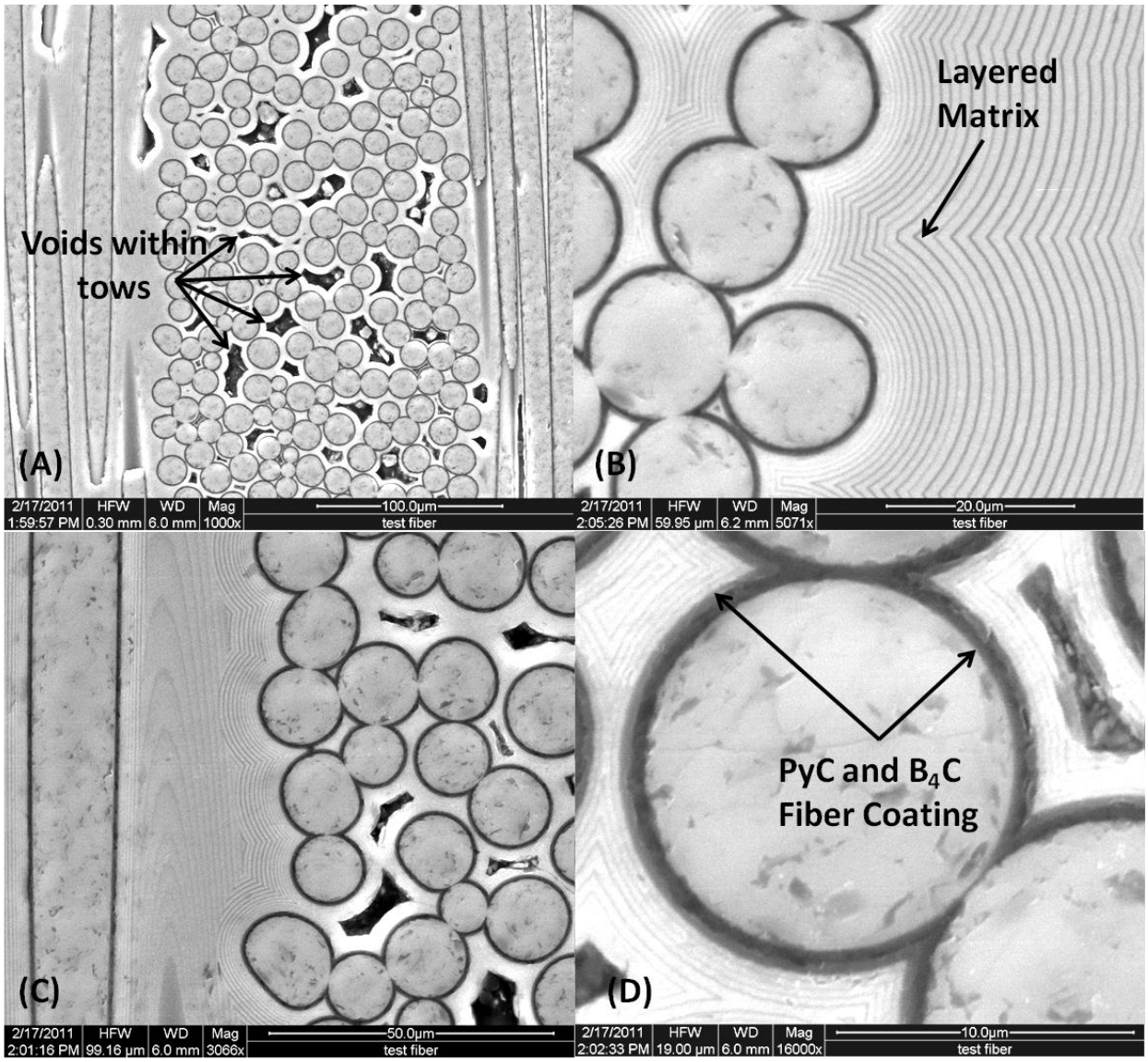

Figure 37: SEM micrographs of the as-processed material from Panel 4 showing A) voids within fiber tows, B) the layered matrix, C) fibers and the layered structure of the matrix, D) duel-layered PyC and B_4C fiber coating.

5.7.2 Microstructure of Specimens Tested in Tension to Failure

The fracture surfaces of the specimens tested in tension to failure were examined using both an optical microscope and a scanning electron microscope (SEM). The optical micrographs can be seen in Figure 38 through Figure 41. Additional optical micrographs can be found in

Appendix A. Fracture of the specimens appears to be nearly linear along 90° fiber tows normal to the loading direction. Minimal fiber pull-out is observed in these figures while little to no oxidation can be seen. This meets expectations due to the small exposure time in the harsh test environment because of the relatively short duration of the tension tests. No signs of delamination can be seen, either.

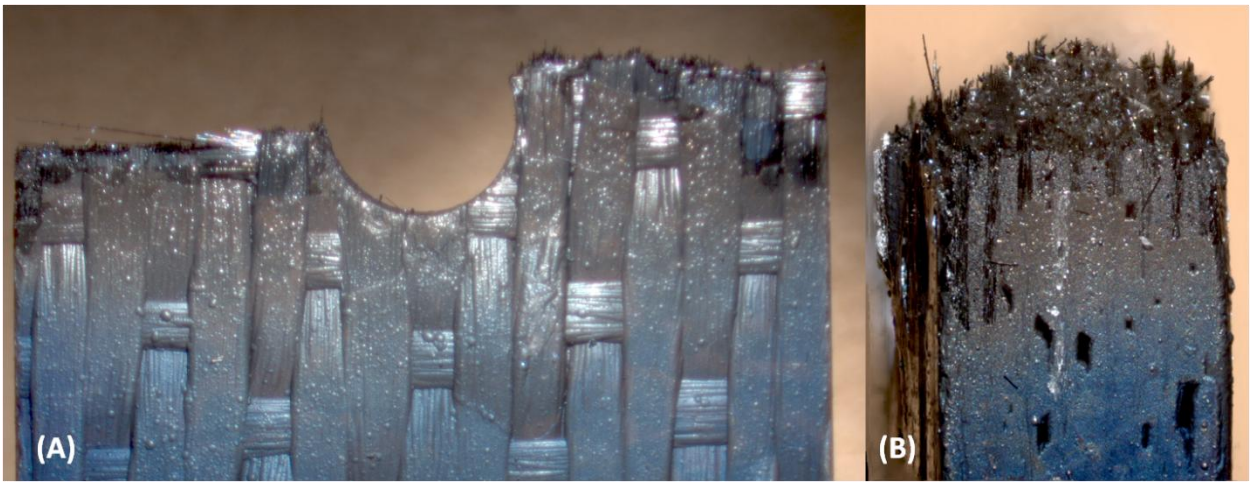

Figure 38: Optical micrographs of the fracture surfaces produced in tensile test to failure conducted at 0.05 mm/s at 1200°C in air on specimen 14.

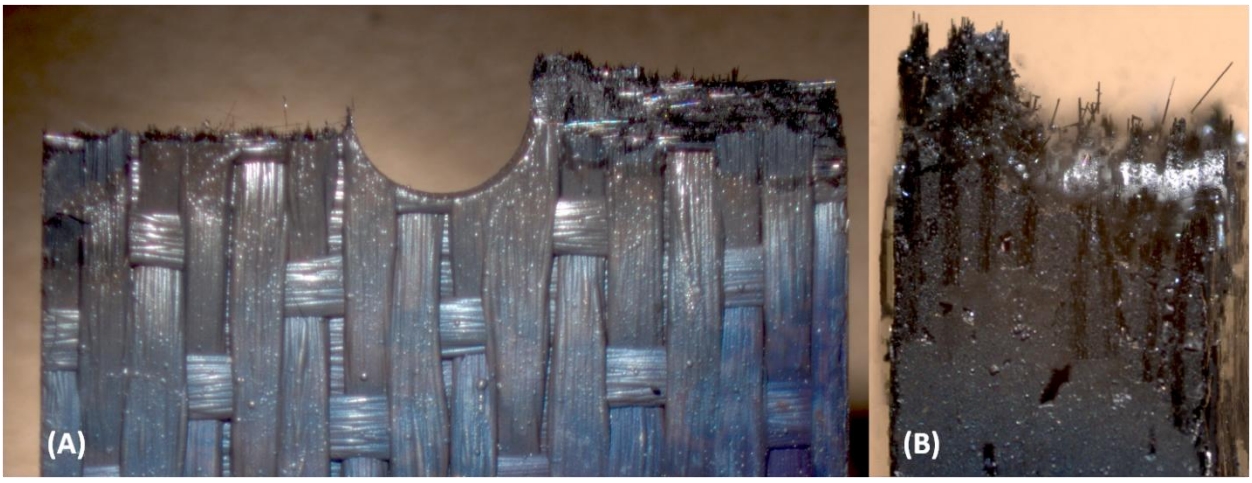

Figure 39: Optical micrographs of the fracture surfaces produced in tensile test to failure conducted at 0.05 mm/s at 1200°C in air on specimen 38.

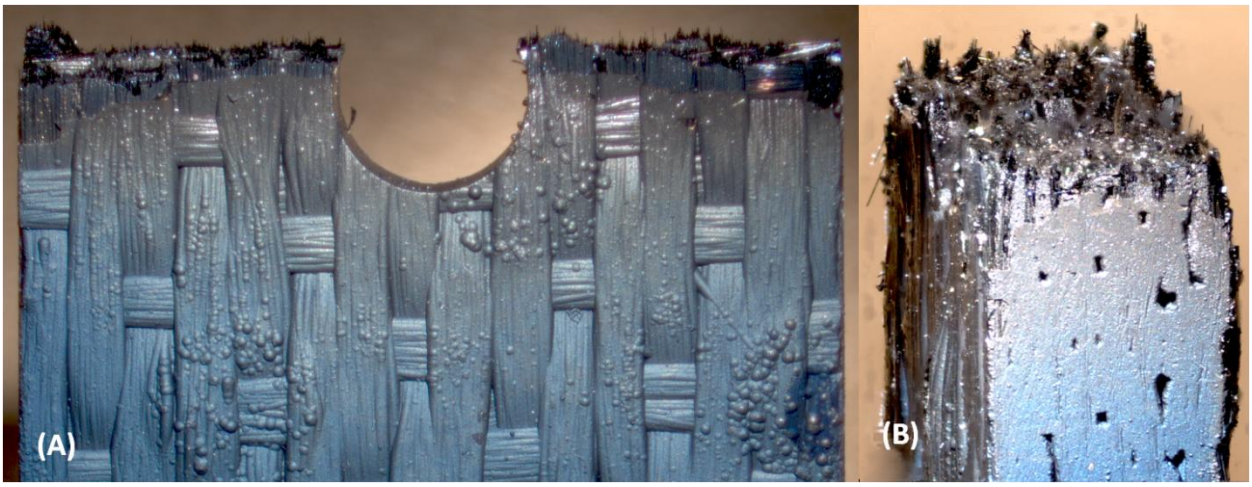

Figure 40: Optical micrographs of the fracture surfaces produced in tensile test to failure conducted at 0.05 mm/s at 1200°C in air on specimen 45.

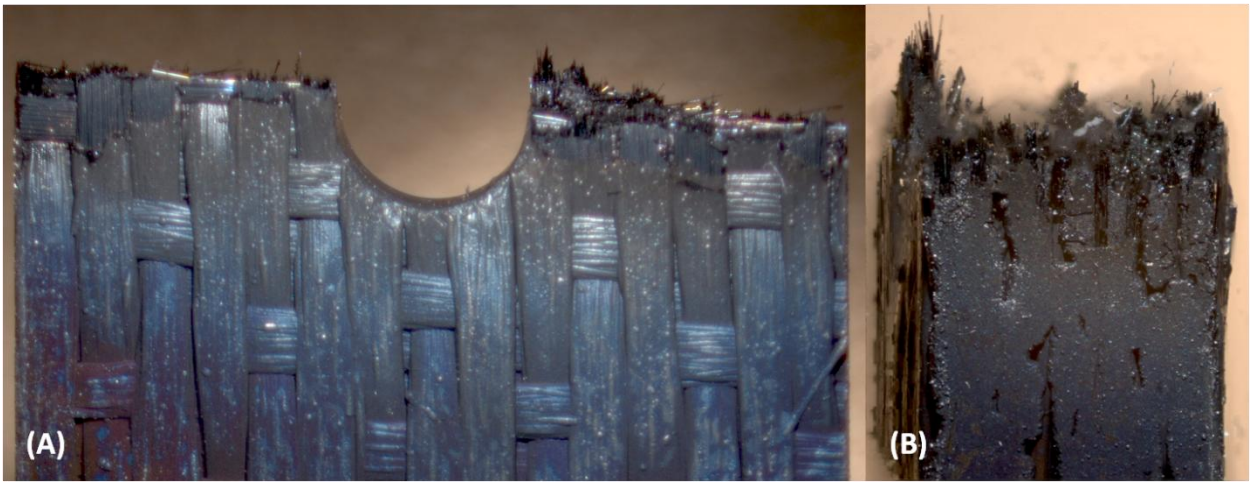

Figure 41: Optical micrographs of the fracture surfaces produced in tensile test to failure conducted at 0.05 mm/s at 1200°C in air on specimen 48.

SEM micrographs of the specimens tested in tension to failure can be seen in Figure 42 through Figure 45 as well as in Appendix B. These micrographs confirm the initial observations from the optical micrographs seen above. All specimens demonstrate a failure mode dominated

by fiber pull-out with minimal oxidation due to the limited exposure time in the (oxidative) test environment, with all tests lasting less than 20 seconds (after warm-up).

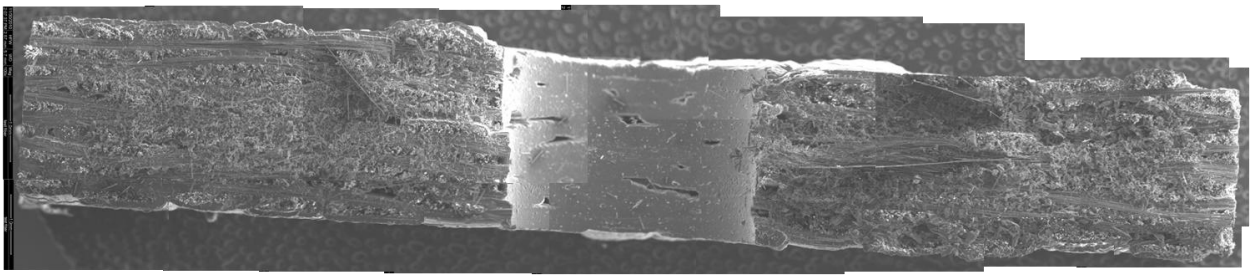

Figure 42: SEM micrograph of the composite fracture surface produced in tensile test to failure conducted at 0.05 mm/s at 1200°C in air on specimen 14.

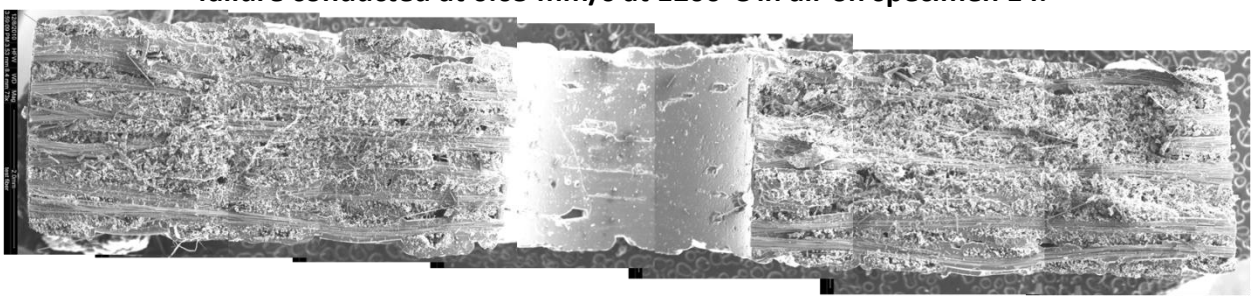

Figure 43: SEM micrograph of the composite fracture surface produced in tensile test to failure conducted at 0.05 mm/s at 1200°C in air on specimen 38.

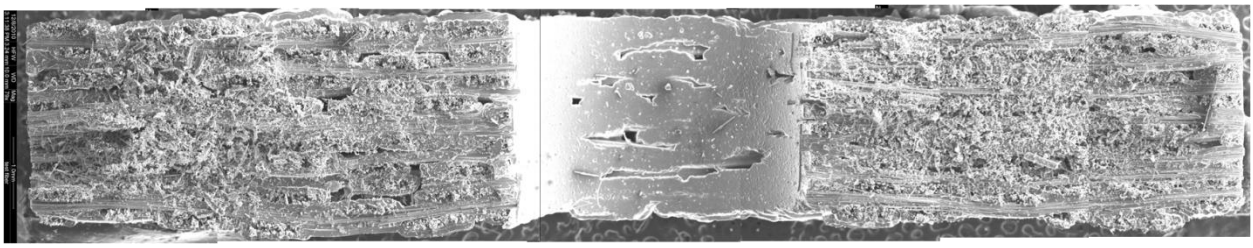

Figure 44: SEM micrograph of the composite fracture surface produced in tensile test to failure conducted at 0.05 mm/s at 1200°C in air on specimen 45.

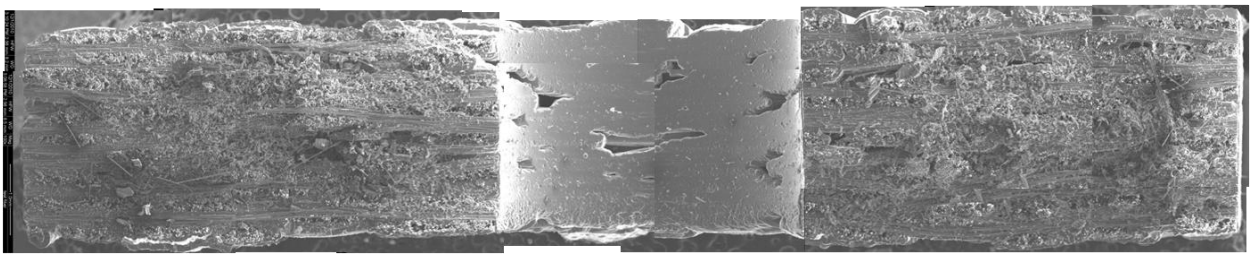

Figure 45: SEM micrograph of the composite fracture surface produced in tensile test to failure conducted at 0.05 mm/s at 1200°C in air on specimen 48.

5.7.3 Microstructure of the Specimens Tested at 0.1 Hz

Optical micrographs of the specimens tested at 0.1 Hz are shown in Figure 46 and Figure 47. Additional optical micrographs can be found in Appendix A.

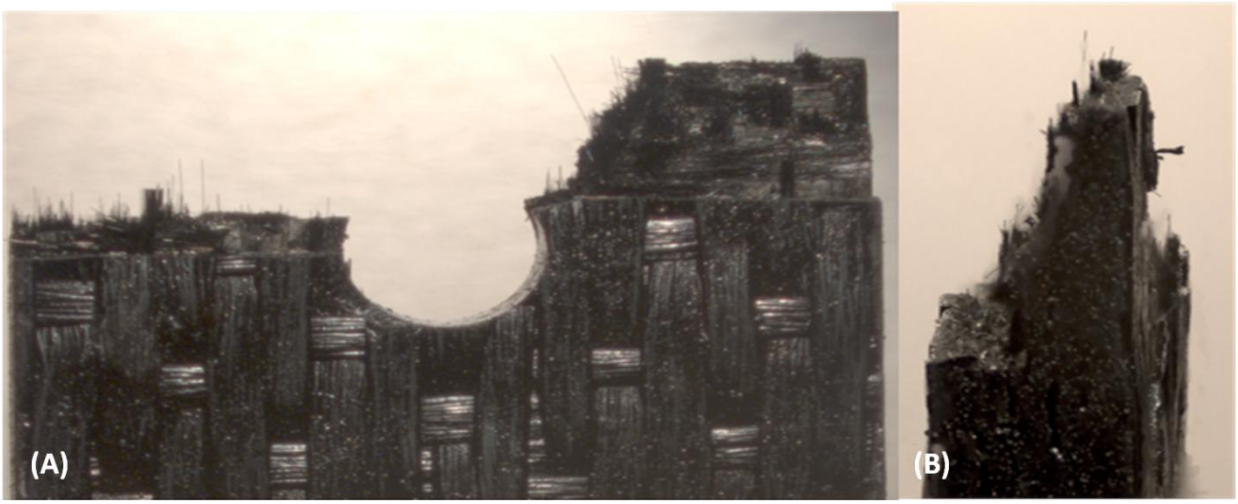

Figure 46: Optical micrographs of the fracture surfaces of specimen 42 tested in fatigue at 0.1 Hz in air at 1200°C. σ_{max} = 140 MPa, N_f = 51,238, t_f = 142.3 h

Figure 47: Optical micrographs of the fracture surfaces of specimen 35 tested in fatigue at 0.1 Hz in steam at 1200°C. σ_{max} = 100 MPa, N_f = 100,000, t_f = 277.8 h

SEM micrographs of specimen 42 tested in fatigue at 0.1 Hz in air at 140 MPa can be found in Figure 48. Large areas of oxidation can be seen in Figure 48A, Figure 48B, and Figure 48C while fiber pull-out can is shown in Figure 48D.

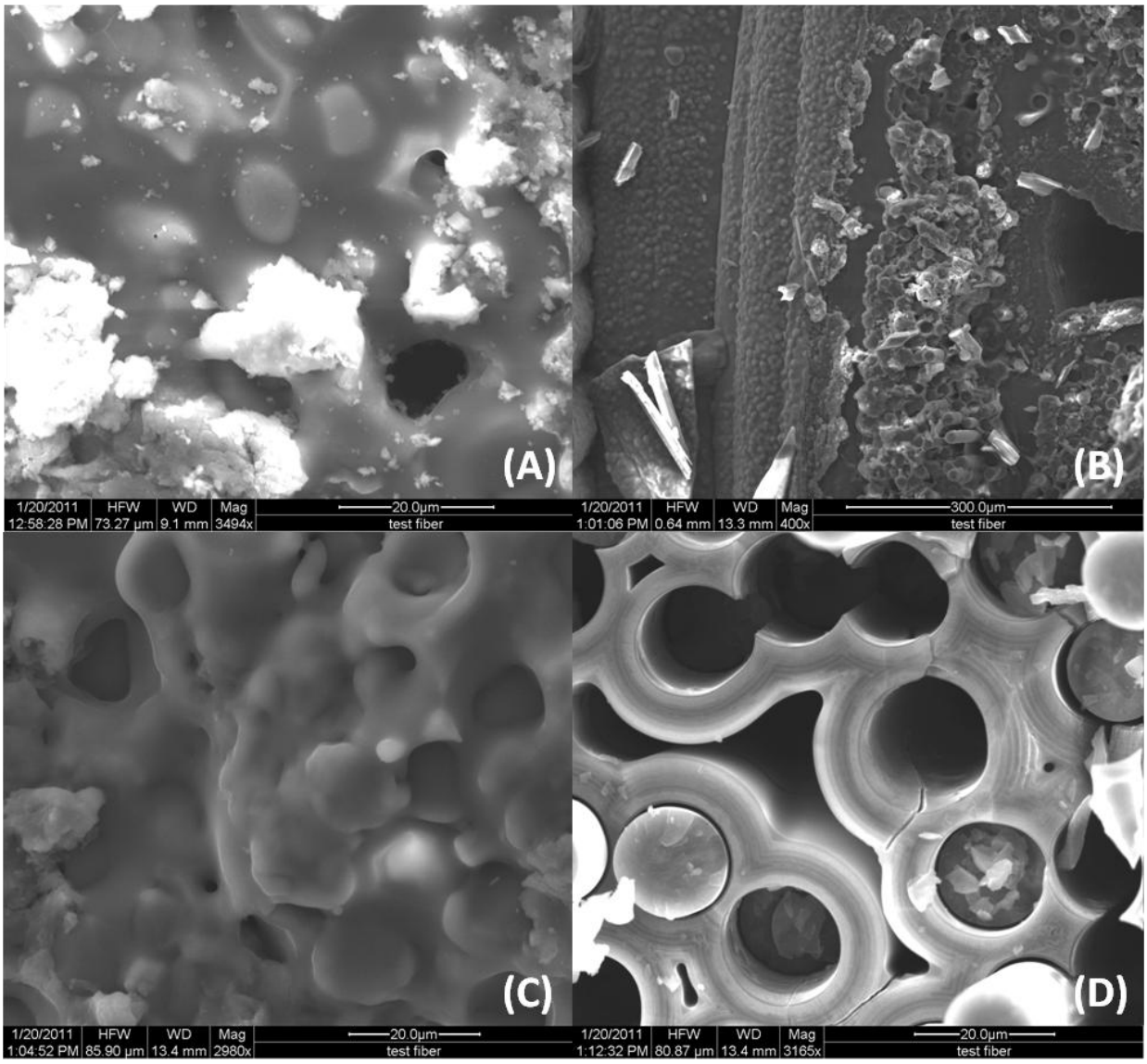

Figure 48: SEM micrographs of the fracture surfaces of specimen 42 tested in fatigue at 0.1 Hz in air at 1200°C. σ_{max} = 140 MPa, N_f = 51,238, t_f = 142.3 h

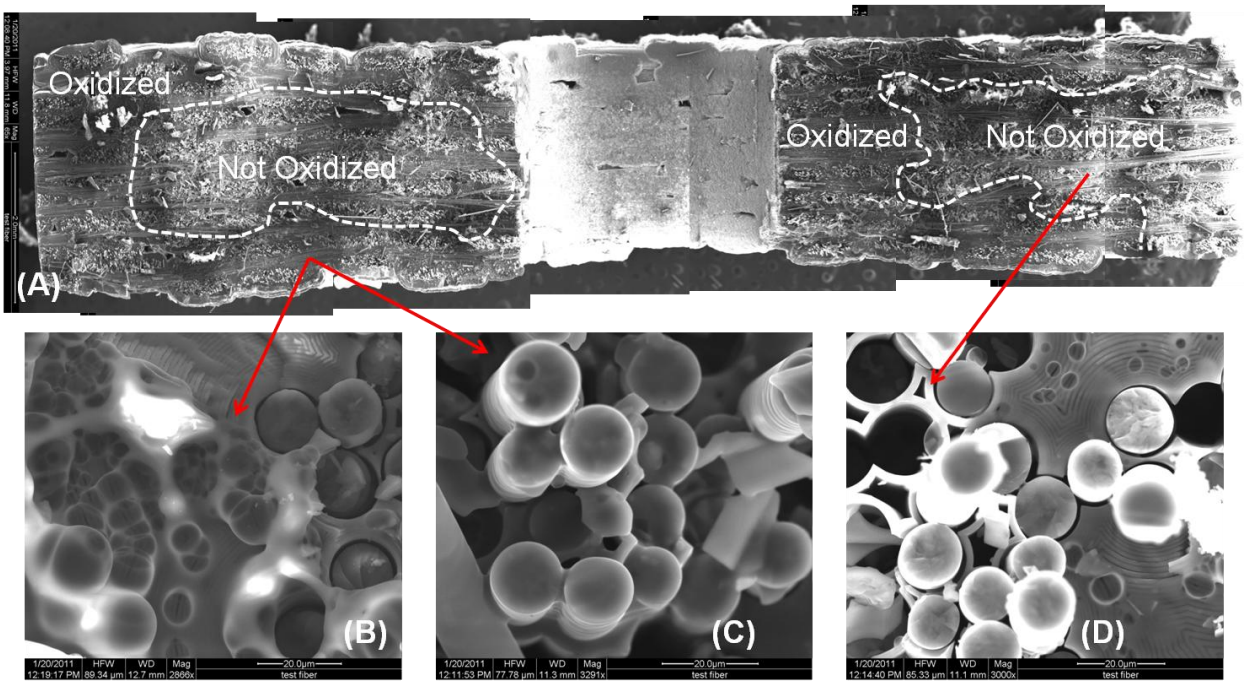

Figure 49: SEM micrographs of the fracture surfaces of specimen 35 tested in fatigue at 0.1 Hz in steam at 1200°C. σ_{max} = 100 MPa, N_f = 100,000, t_f = 277.8 h

Figure 49 shows the composite SEM micrograph of the fracture surface of the specimen reaching run-out in steam at 0.1 Hz. It can be seen from the composite image that nearly half of the fracture surface was oxidized at failure. Figure 49B shows glass formations on the fracture surface appearing as bubbles on the fibers. Figure 49C shows a glassy structure bonding the fibers together. Both of these micrographs show typical oxidized appearance while Figure 49D shows some non-oxidized regions in the left portion of the micrograph. Non-oxidized regions show intact fiber coatings and sharp features on the fracture surfaces. There still appears to be glass formations in the right half of the micrograph.

The specimen depicted in Figure 49 achieved run-out experiencing a loss in strength of nearly 18%. Although the specimen ultimately failed in a tension to failure test, major signs of oxidation can be found throughout its fracture surface.

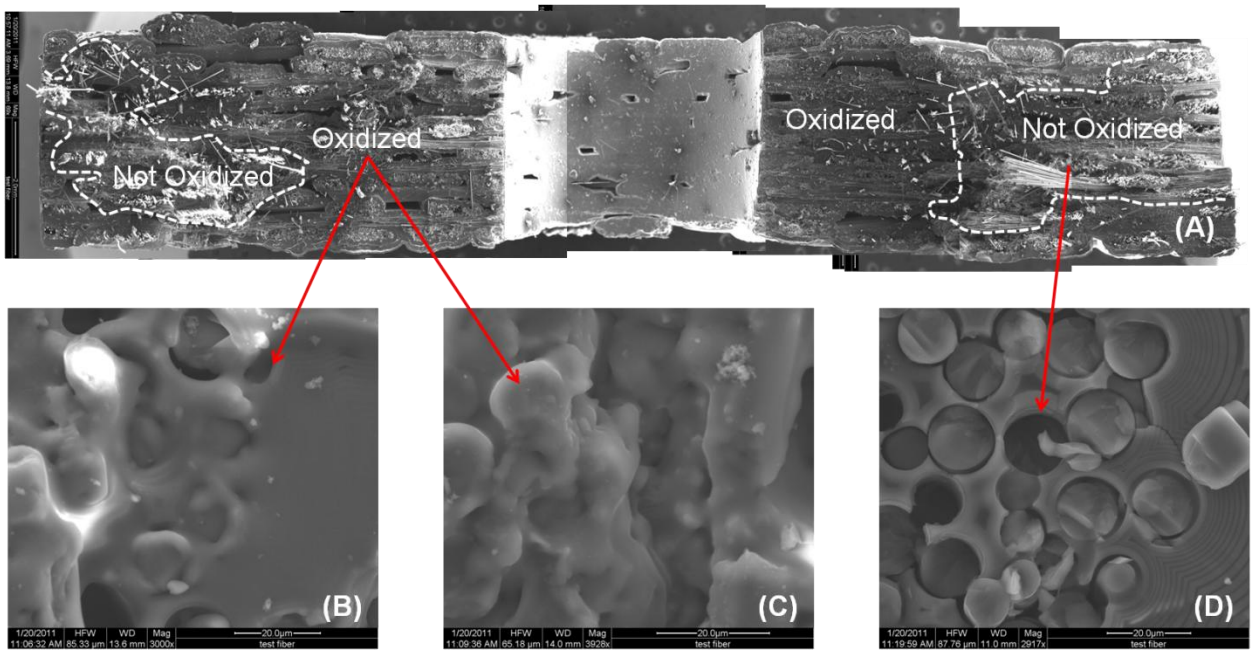

Figure 50: SEM micrographs of the fracture surfaces of specimen 11 tested in fatigue at 0.1 Hz in air at 1200°C. σ_{max} = 120 MPa, N_f = 22,195, t_f = 61.7 h

Figure 50A shows the composite SEM mircograph of the fracture surface of the specimen tested at 0.1 Hz in fatigue at 120 MPa in air. More than half of the fracture surface appears to be oxidized including all of the area surrounding the center-drilled hole. The large areas of oxidation appear to have influenced this specimen's relatively short lifetime; the specimen tested at the same stress level in steam lasted twice as long (123.7 h).

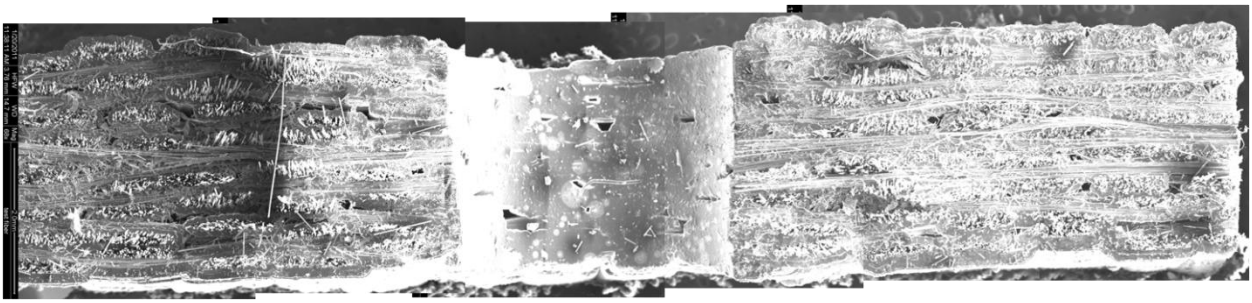

Figure 51: SEM micrograph of the fracture surfaces of specimen 12 tested in fatigue at 0.1 Hz in air at 1200°C. σ_{max} = 80 MPa, N_f = 100,000, t_f = 277.8 h

Figure 51 shows the composite SEM micrograph of the fracture surface of the specimen achieving run-out at 0.1 Hz in air. It is interesting to note that there are very minimal areas of oxidation seen on the fracture surface with the failure mode being primarily fiber pull-out (most likely occurring during the tension to failure test conducted upon completion of fatigue cycling). The areas of oxidation are limited mainly to the outside edges of the fracture surface with nominal oxidation on the interior. When compared to the fracture surface of the specimen achieving run-out at the same frequency in steam (Figure 49) has much greater areas of oxidation.

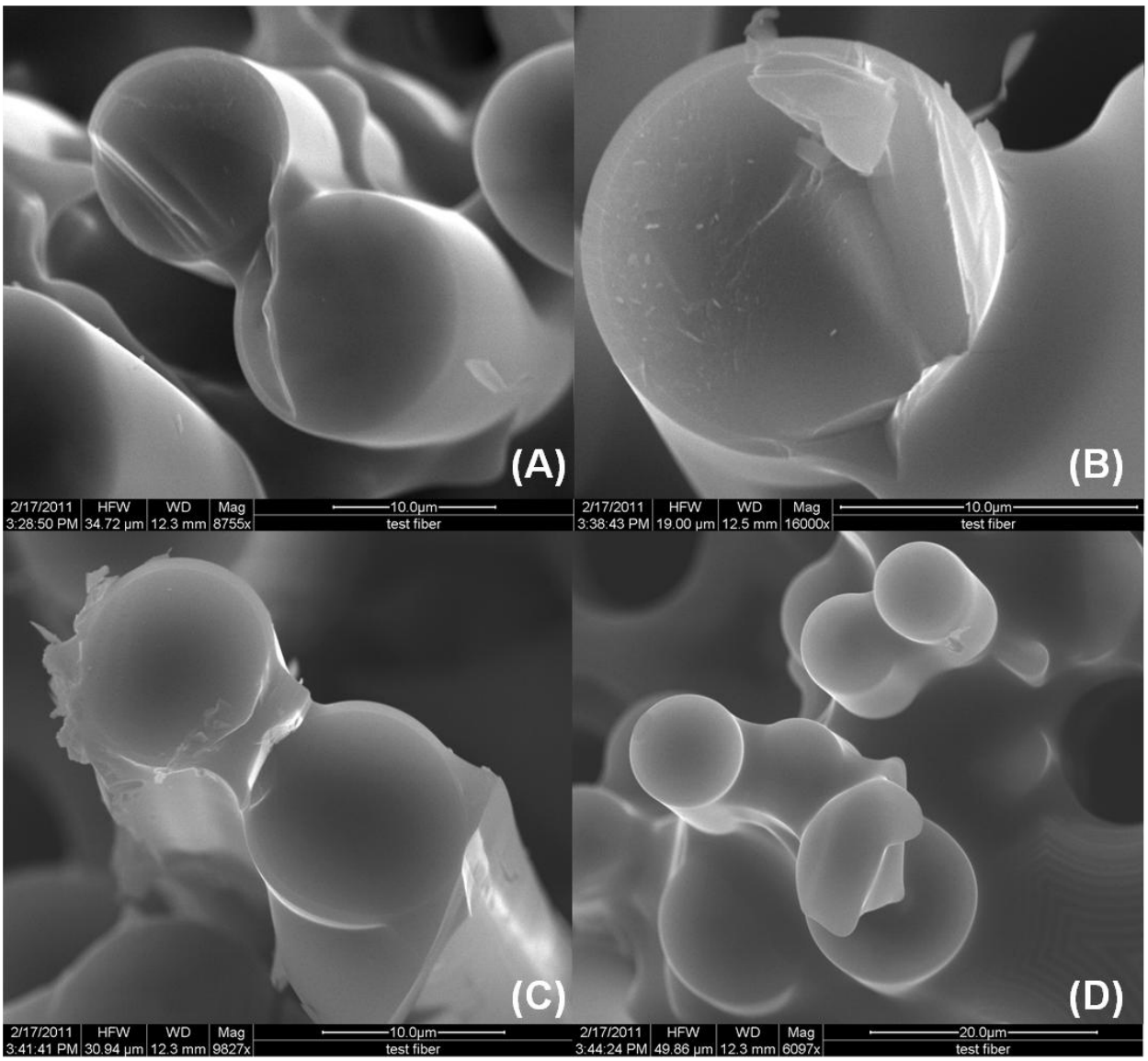

Figure 52: SEM micrographs of the fiber fracture surfaces of specimen 12 tested in fatigue at 0.1 Hz in air at 1200°C. σ_{max} = 80 MPa, N_f = 100,000, t_f = 277.8 h.

Figure 52 shows the fiber fracture surfaces of the specimen achieving run-out in air at 0.1 Hz. The composite micrograph is seen in Figure 51 showing few areas of heavy oxidation. Figure 52A and Figure 52D show areas of fiber oxidation with a smooth, glassy appearance to

the fiber's fracture surface while Figure 52B and Figure 52C show fiber fracture surface with areas of matrix still attached to the fiber.

5.7.4 Microstructure of the Specimens Tested in Fatigue at 1.0 Hz

Optical micrographs of specimens tested at 1.0 Hz at 120 MPa in steam and air can be found in Figure 53 and Figure 54, respectively. A large amount of fiber pull-out is observed in the specimen tested in steam.

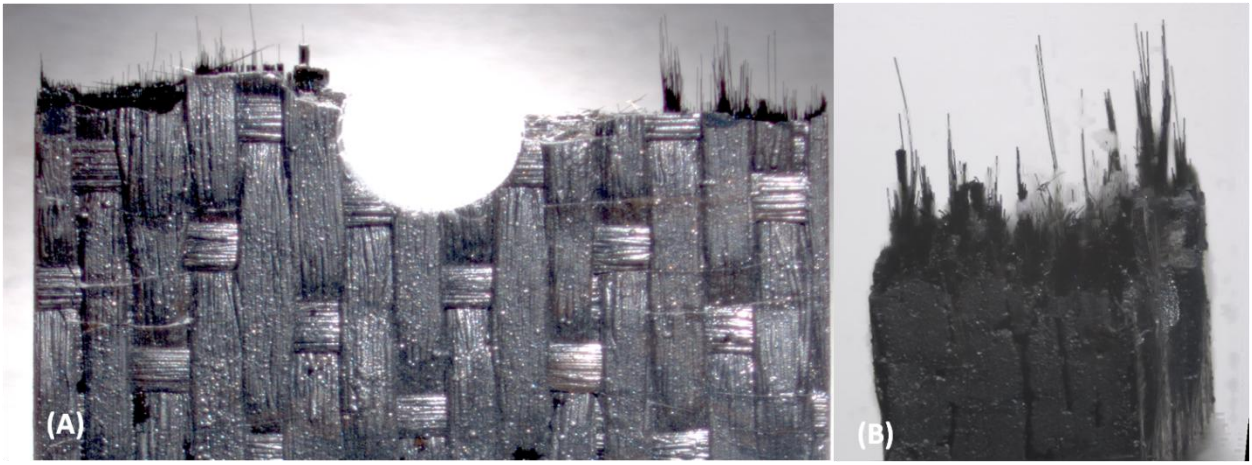

Figure 53: Optical micrographs of the fracture surfaces of specimen 13 tested in fatigue at 1.0 Hz in steam at 1200°C. σ_{max} = 120 MPa, N_f = 177,335, t_f = 49.3 h

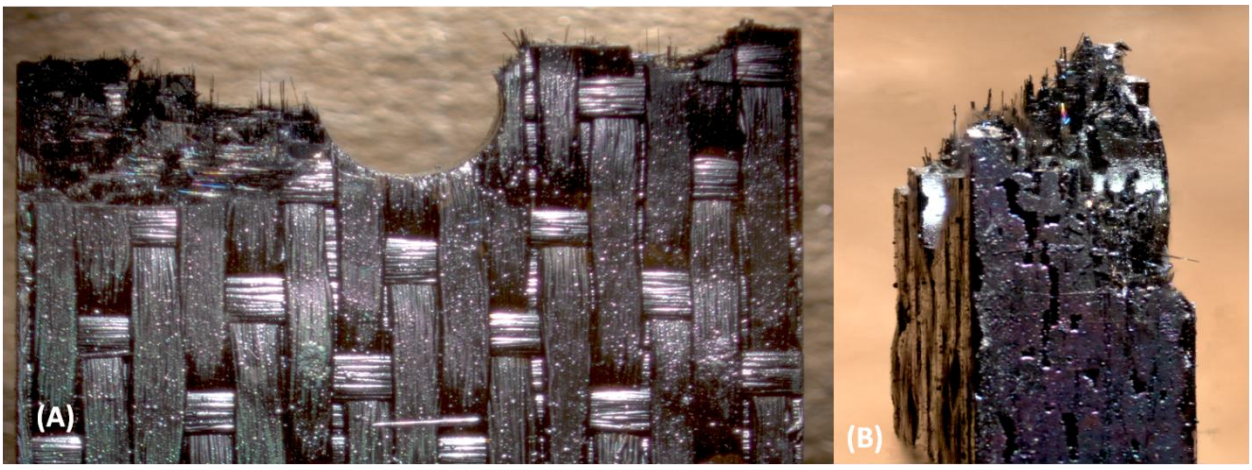

Figure 54: Optical micrographs of the fracture surfaces of specimen 18 tested in fatigue at 1.0 Hz in air at 1200°C. σ_{max} = 120 MPa, N_f = 77,575, t_f = 21.5 h

The SEM micrographs of the two specimens tested at 1.0 Hz seen above can be found in Figure 55 through Figure 58. Figure 55 shows close to half of the fracture surface is oxidized. When examined closer, Figure 56A and Figure 56B show close ups of fiber pull-out while Figure 56C and Figure 56D show areas of fiber oxidation. Oxidation can be seen readily throughout areas of the fracture surface, as shown in Figure 57.

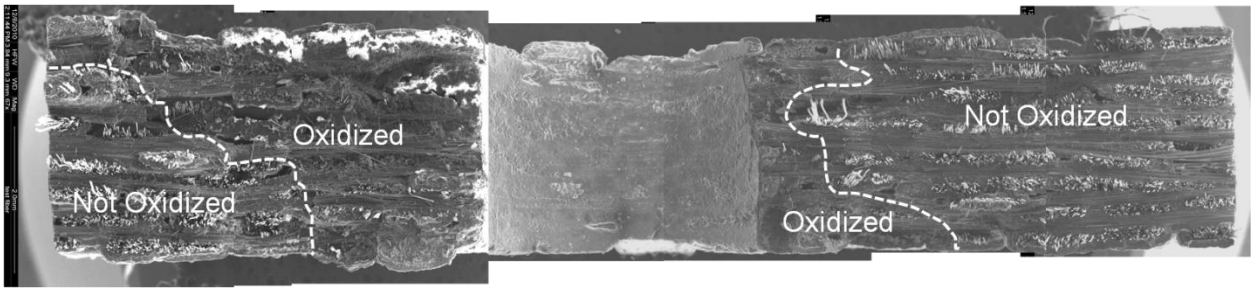

Figure 55: SEM micrograph of the fracture surfaces of specimen 13 tested in fatigue at 1.0 Hz in steam at 1200°C. σ_{max} = 120 MPa, N_f = 177,335, t_f = 49.3 h showing areas of oxidation.

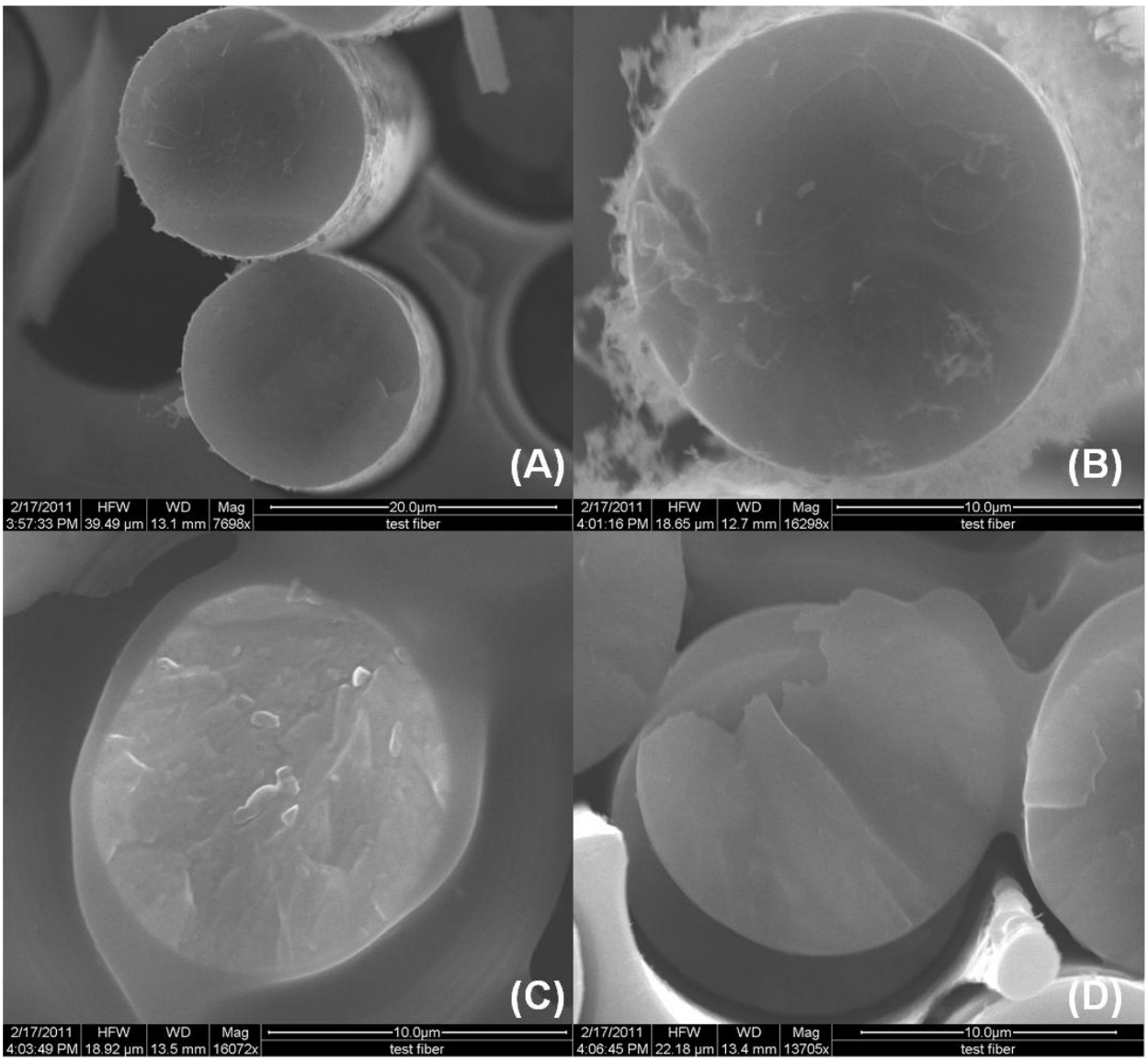

Figure 56: SEM micrographs of the fiber fracture surfaces of specimen 13 tested in fatigue at 1.0 Hz in steam at 1200°C. σ_{max} = 120 MPa, N_f = 177,335, t_f = 49.3 h

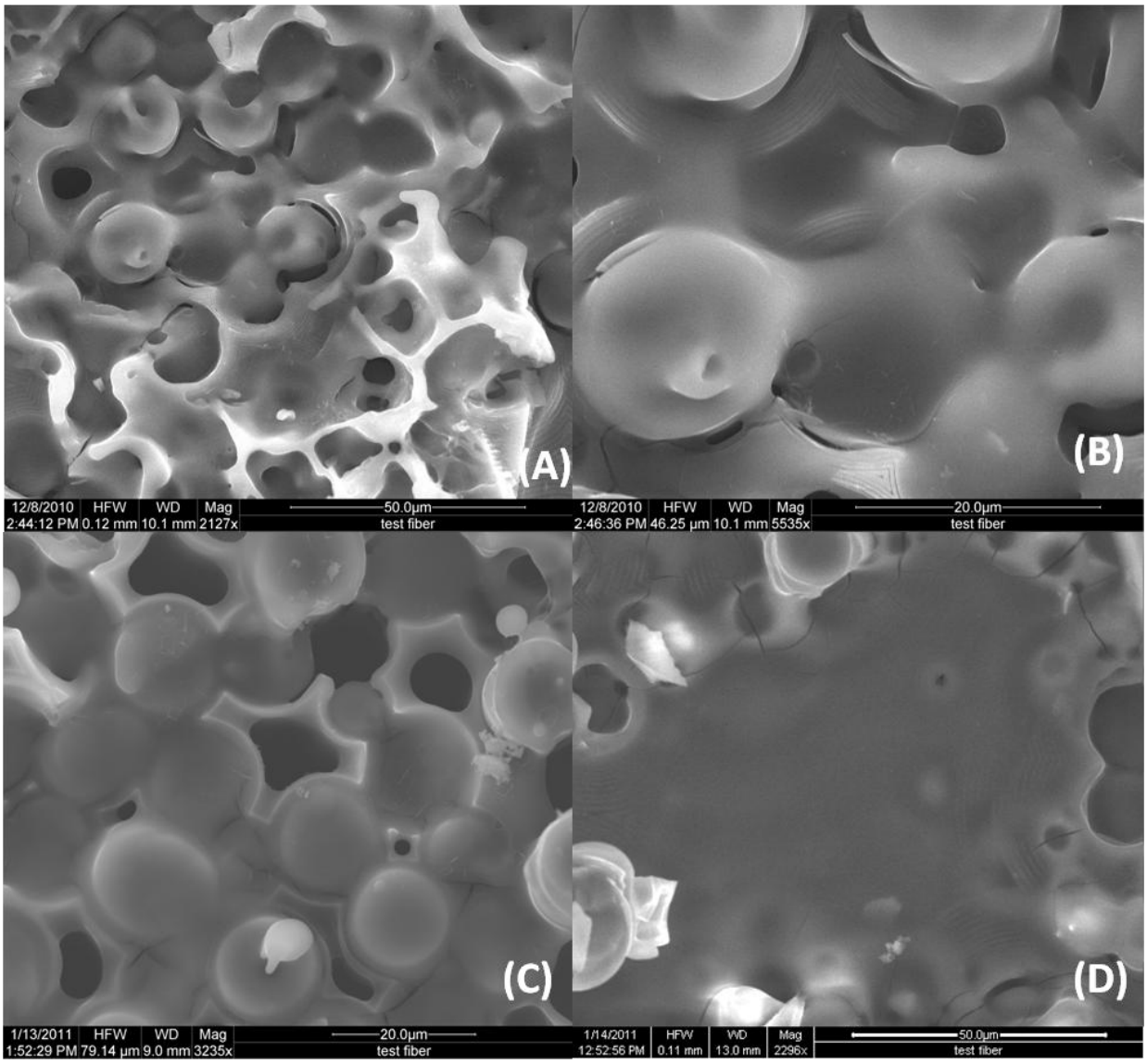

Figure 57: SEM micrographs of the fracture surfaces of specimen 13 tested in fatigue at 1.0 Hz in steam at 1200°C. σ_{max} = 120 MPa, N_f = 177,335, t_f = 49.3 h

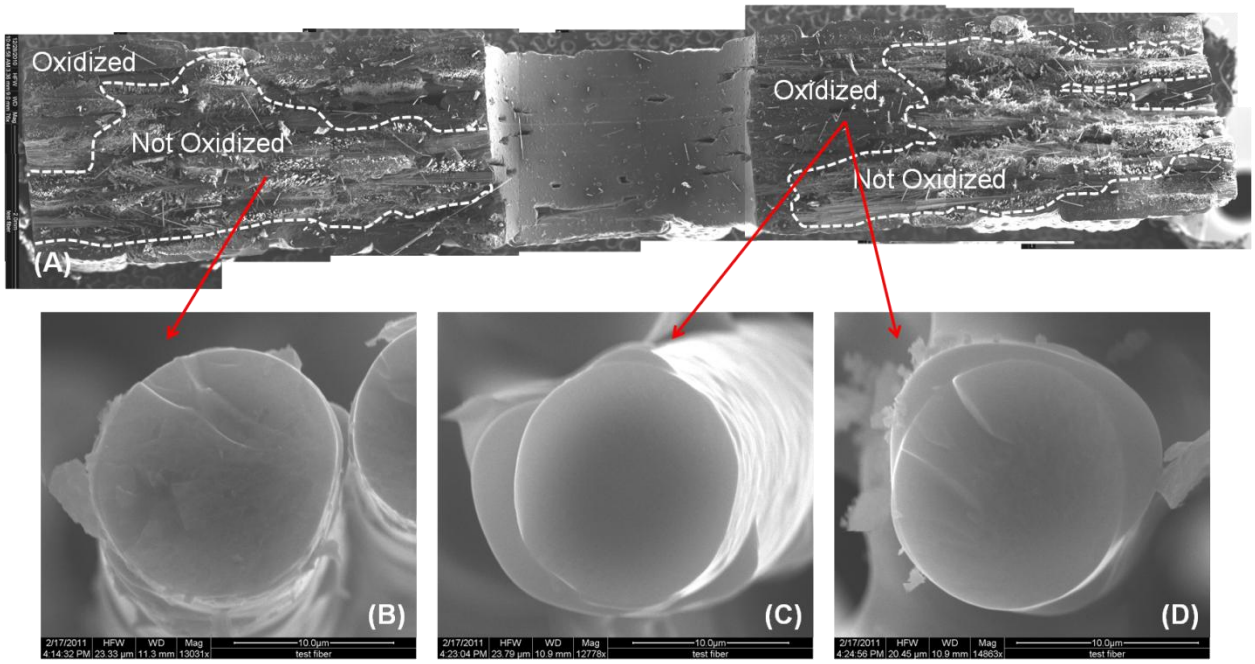

Figure 58: SEM micrographs of the fracture surfaces of specimen 18 tested in fatigue at 1.0 Hz in air at 1200°C. σ_{max} = 120 MPa, N_f = 77,575, t_f = 21.5 h

The specimen tested in air (Figure 58) shows much less oxidation than the specimen tested in steam (Figure 55) at 1.0 Hz at 120 MPa. The fiber fracture surfaces show a nearly smooth fracture surface rather than jagged fracture at the fiber level as seen in Figure 58B, Figure 58C, and Figure 58D.

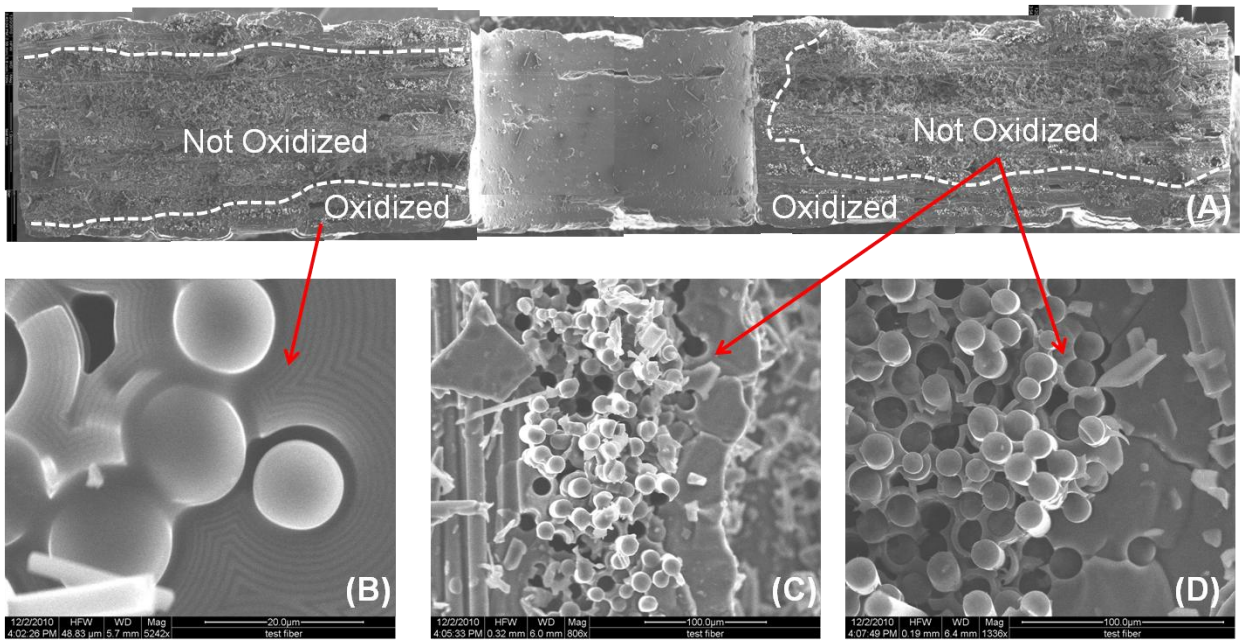

Figure 59: SEM micrographs of the fracture surfaces of specimen 37 tested in fatigue at 1.0 Hz in air at 1200°C. σ_{max} = 100 MPa, N_f = 200,000, t_f = 55.6 h

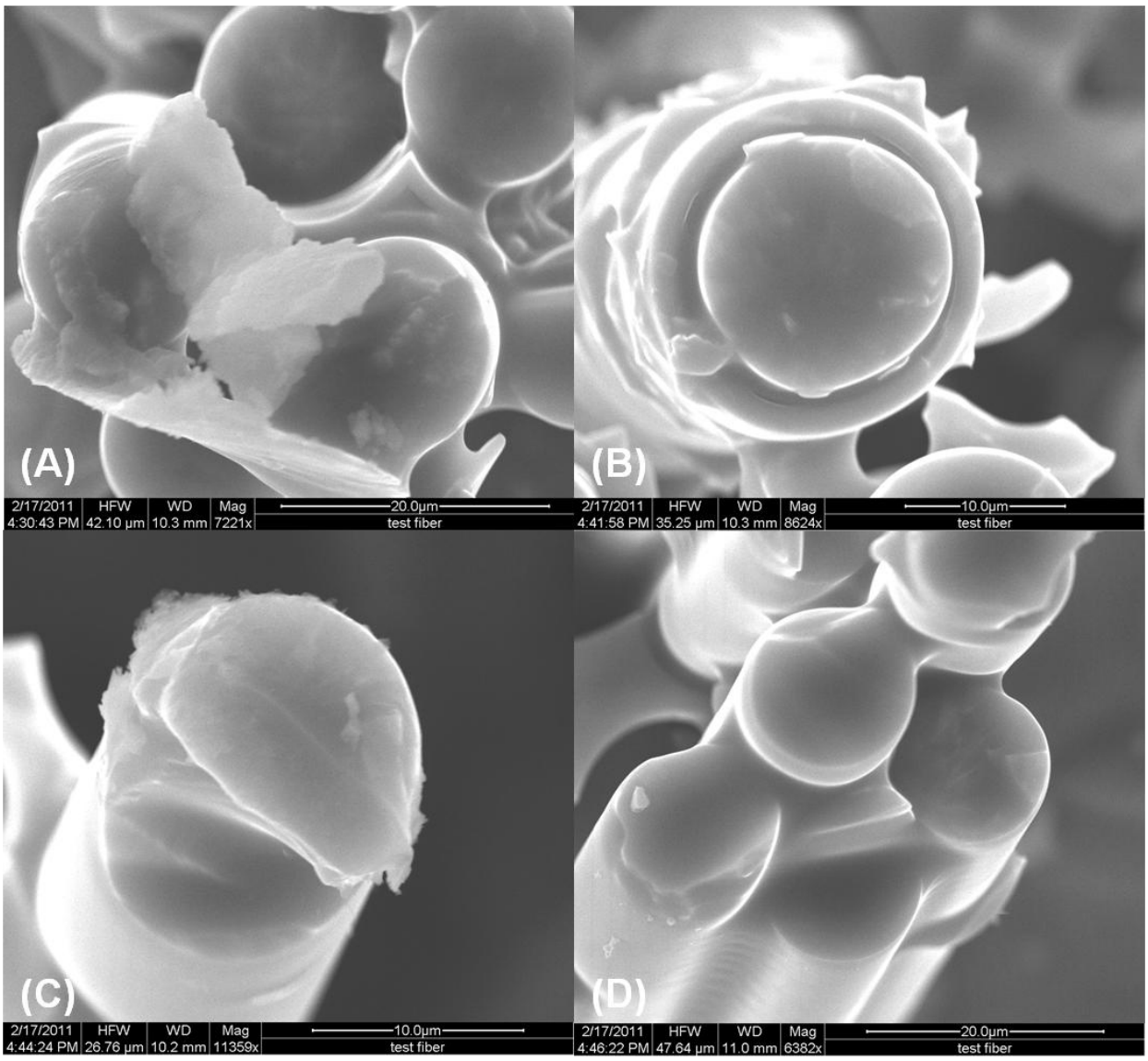

Figure 60: SEM micrographs of the fiber fracture surfaces of specimen 37 tested in fatigue at 1.0 Hz in air at 1200°C. σ_{max} = 100 MPa, N_f = 200,000, t_f = 55.6 h

The SEM micrographs of the fracture surface of the specimen achieving run-out in air at 1.0 Hz can be found in Figure 59. Minor oxidation can be seen in the form of glassy fibers as demonstrated in Figure 59B. The failure mode of this specimen appears to be primarily due to fiber pull-out from the tension to failure test as seen Figure 59C and Figure 59D. The specimen

achieving in run-out in air tested at 0.1 Hz (Figure 51) showed little to no oxidation while this specimen shows a bit more along the edges of the fracture surface.

Fiber fracture surfaces of the specimen reaching run-out at 1.0 Hz in air is seen in Figure 60. Oxidation of these fracture surfaces can be seen in Figure 60A and Figure 60D while Figure 60B and Figure 60C show primarily brittle fracture as a failure mode, with an uneven surface. It is possible that breakage of these fibers throughout the cross section occurred during fatigue, reducing the total number of fibers to carry the load, and thus, reducing retained tensile strength.

When comparing the microstructure of the specimen achieving run-out in air at 1.0 Hz (Figure 59) to that of the specimen achieving run-out in steam at 1.0 Hz, the specimen achieving run-out in steam shows a much greater amount of oxidation, as seen in Figure 61.

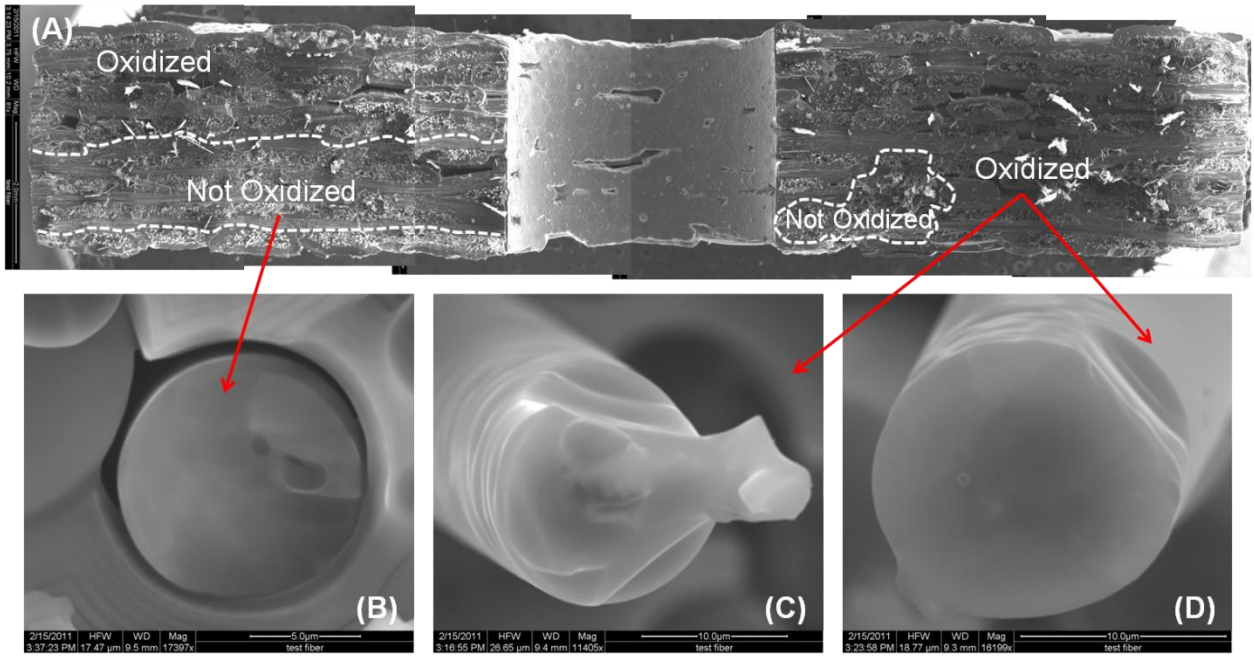

Figure 61: SEM micrographs of the fracture surfaces of specimen 43 tested in fatigue at 1.0 Hz in air at 1200°C. σ_{max} = 100 MPa, N_f = 200,000, t_f = 55.6 h

5.7.5 Microstructure of the Specimens Tested at 10 Hz

Optical micrographs of the specimens tested at 10 Hz in steam and air are shown in Figure 62 and Figure 63, respectively. Both specimens were tested at 140 MPa at 1200°C. Minimal fiber pull-out and no signs of delamination can be seen in both specimens tested. The specimen tested in steam (Figure 62) shows a "cleaner" break with a more level appearance on the fracture surface than that of the specimen tested in air (Figure 63).

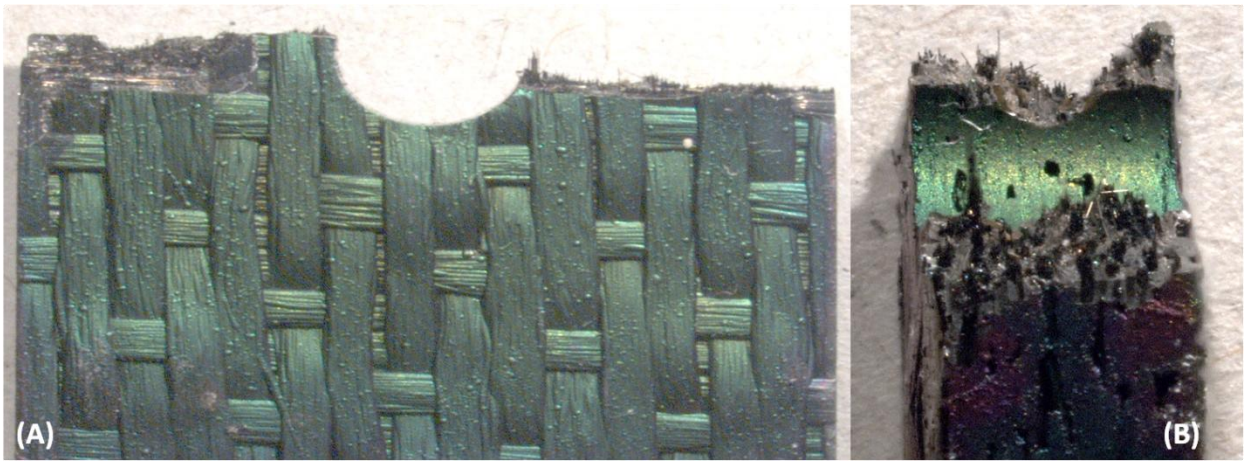

Figure 62: Optical micrographs of the fracture surfaces of specimen 46 tested in fatigue at 10 Hz in steam at 1200°C. σ_{max} = 140 MPa, N_f = 26,485, t_f = 0.7 h

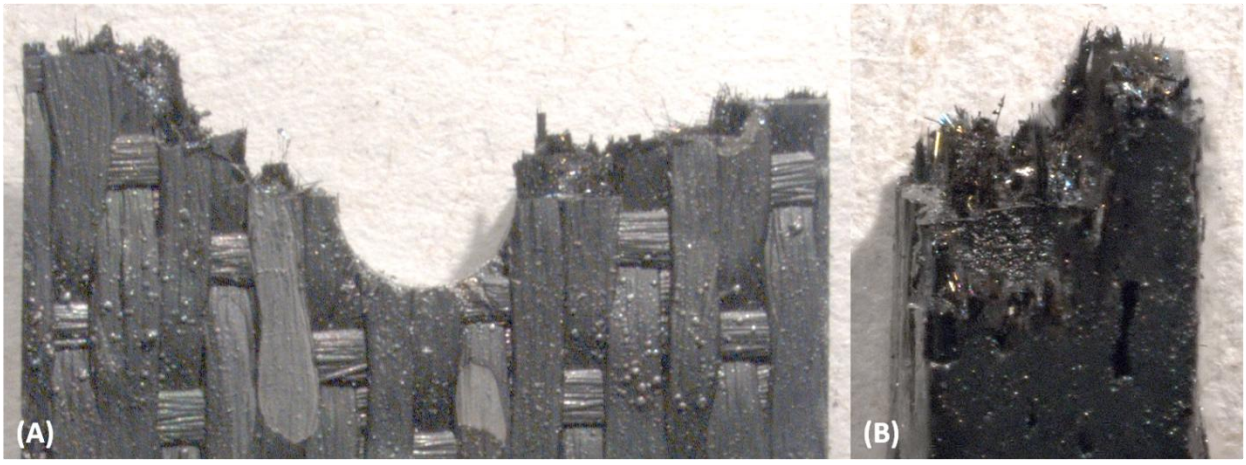

Figure 63: Optical micrographs of the fracture surfaces of specimen 47 tested in fatigue at 10 Hz in air at 1200°C. σ_{max} = 140 MPa, N_f = 200,000, t_f = 5.6 h

SEM micrographs of the two specimens tested at 10 Hz can be found in Figure 64 through Figure 67. The specimen tested in steam seen in Figure 64 shows a fracture surface nearly entirely oxidized, while the fracture surface of the specimen tested in air (Figure 66) shows about half of the fracture surface oxidized.

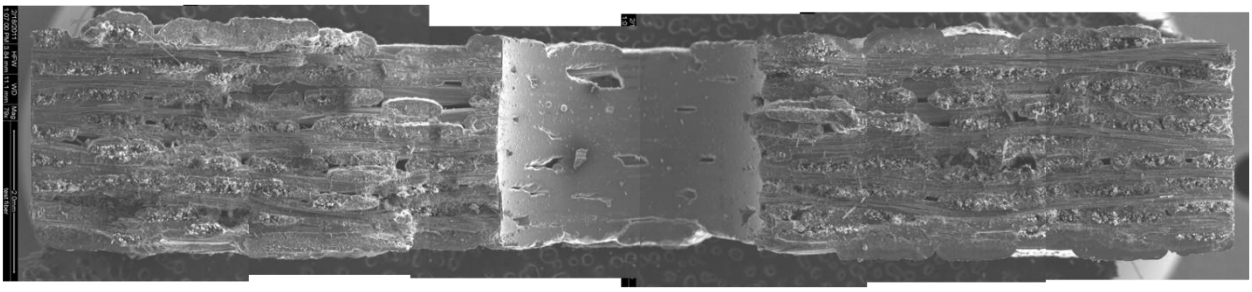

Figure 64: SEM micrograph of the fracture surface of specimen 46 tested in fatigue at 10 Hz in steam at 1200°C. σ_{max} = 140 MPa, N_f = 26,485, t_f = 0.7 h

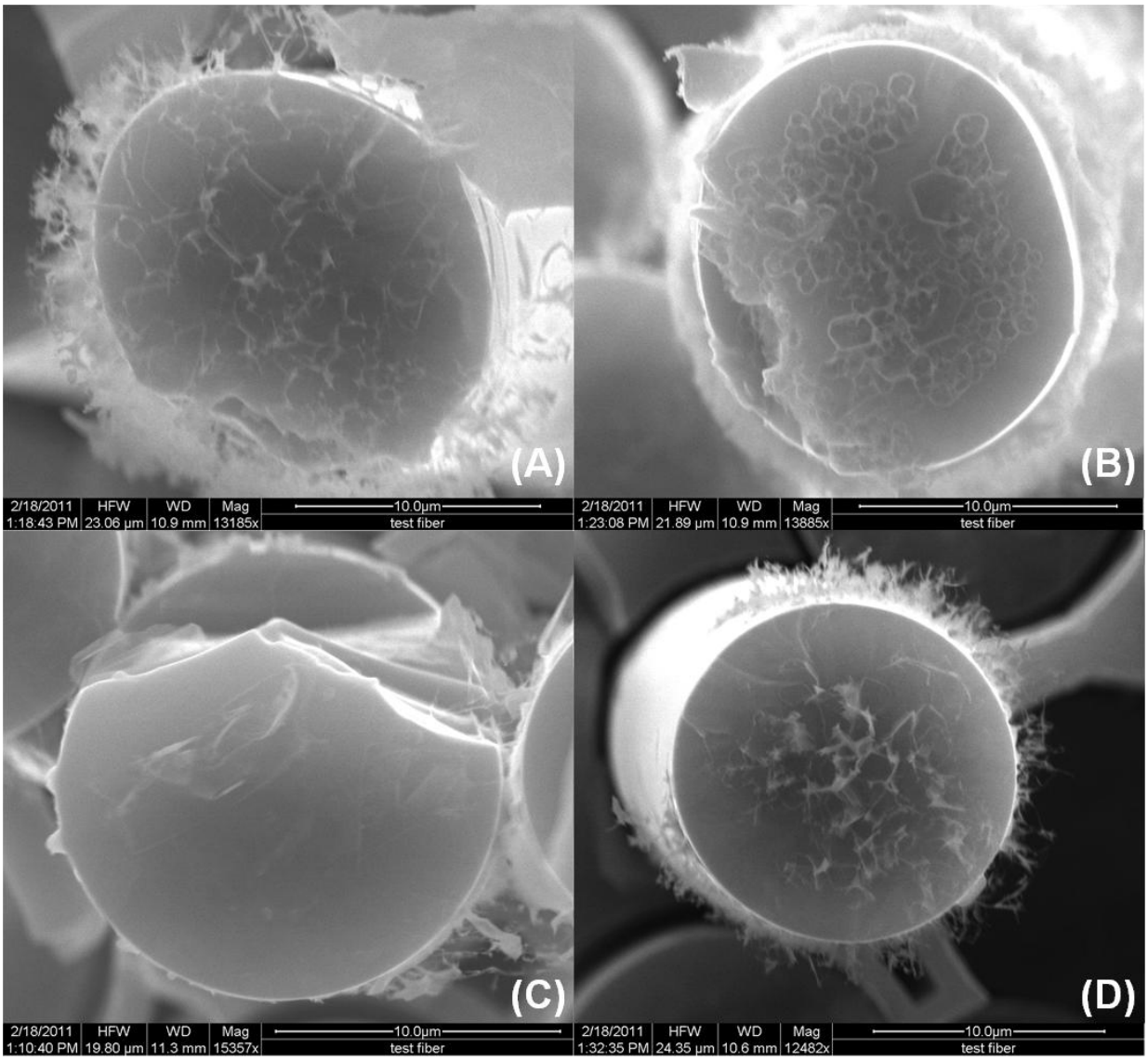

Figure 65: SEM micrographs of the fiber fracture surfaces of specimen 46 tested in fatigue at 10 Hz in steam at 1200°C. σ_{max} = 140 MPa, N_f = 26,485, t_f = 0.7 h

The micrographs seen in Figure 65 show glass formations on the fracture surface of the fibers of the specimen tested in steam at 10 Hz. Figure 65C shows fiber damage with minimal oxidation, but small glass formations are seen surrounding the fiber. It appears as if the entire fiber interface has been removed, causing for such a heavily oxidized fracture surface.

When comparing these micrographs to those of the specimen tested in air, which achieved run-out, there is a stark difference. Although a smoothed over, glassy appearance on the fiber fracture surface can be seen in Figure 67, no jagged glass formations (like the ones seen in Figure 65) are seen. Although the specimen in air was exposed to the test environment much longer before reaching failure (5.6 h), the fibers carried the load much longer. When the fibers are as damaged as seen in the specimen tested in steam (Figure 65), the specimen is bound to fail in a relatively short period of time- in this case, less than one hour.

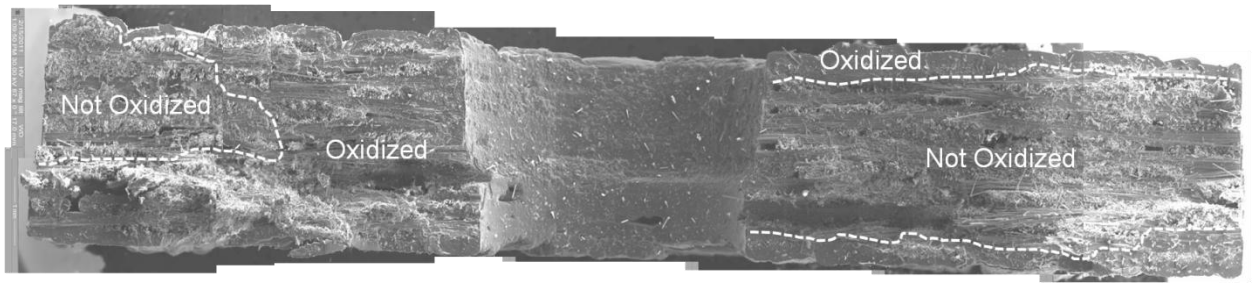

Figure 66: SEM micrograph of the fracture surface of specimen 47 tested in fatigue at 10 Hz in air at 1200°C. σ_{max} = 140 MPa, N_f = 200,000, t_f = 5.6 h

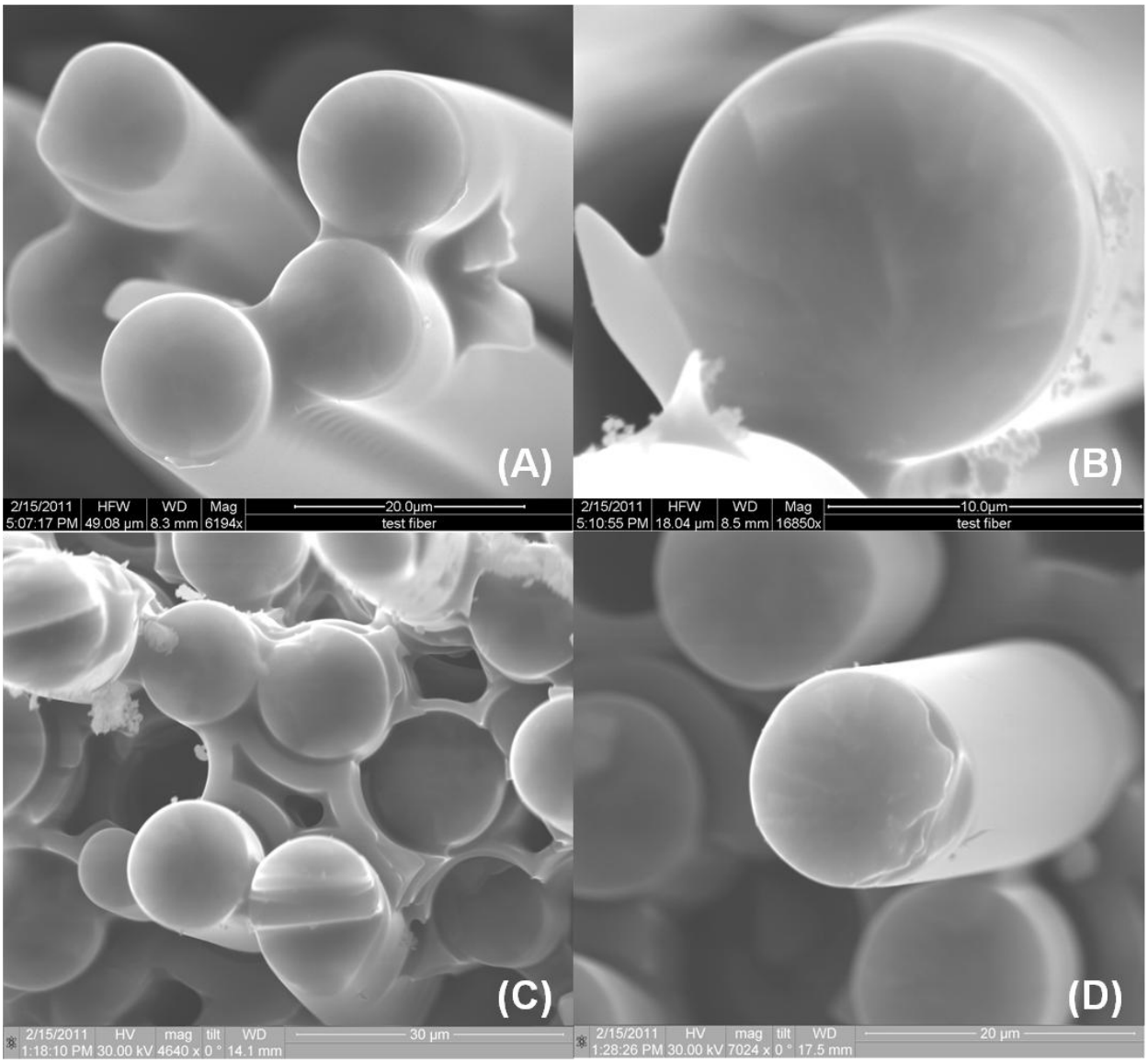

Figure 67: SEM micrographs of the fiber fracture surfaces of specimen 47 tested in fatigue at 10 Hz in air at 1200°C. σ_{max} = 140 MPa, N_f = 200,000, t_f = 5.6 h

VI. Conclusion and Recommendations

6.1 Conclusion

Based on this research's comparison to that of the unnotched specimen in [7] the Hi-Nicalon/PyC/HyprSiC composite appears to be nearly notch insensitive with relatively similar fatigue lifetimes in both air and steam. Minor inconsistency in these lifetimes is believed to be due to both panel to panel variability and the different batches that the notched and unnotched composites were drawn from. The notched specimen performed better in specimens tested at 1.0 Hz in air at higher stress levels (130 MPa and 140 MPa) and in steam at all stress levels tested. The notched specimen also had a longer fatigue life than that of the unnotched specimen at 140 MPa at 0.1 Hz in steam. This is theorized to be due to the fact that the proportional limit of the notched specimen (137.5 MPa) was greater than that of the unnotched specimen (116.3 MPa). The fatigue limit increased with increasing frequency: 80 MPa for 0.1 Hz, 100 MPa for 1.0 Hz, and 140 MPa for 10 Hz. This trend was also observed in the unnotched specimen.

The presence of steam degraded fatigue performance in specimens tested at 0.1 Hz at 140 MPa, at 1.0 Hz and 120 MPa and 130 MPa, and at 10 Hz. The specimens tested in steam also experienced greater permanent strains than those tested in air. Unnotched specimens showed a greater loss in elastic modulus than the notched specimens in air at similar test conditions (same frequency, same maximum stress level) while the opposite was true of the specimens tested in steam.

Prior fatigue had a significant effect on the retained tensile properties of the notched Hi-Nicalon/PyC/HyprSiC composite tested in this research. Tensile strength was reduced in all specimens achieving run-out in all conditions tested: nearly 20% in tests in air and roughly 15% in tests conducted in steam.

Micrographical analysis of all specimens tested revealed signs of oxidation in nearly all specimens tested, with the oxidation being more pronounced in specimens tested in steam. Increased exposure time to the test environment also caused larger areas of oxidation. Specimens achieving run-out suggested breakage of fibers during fatigue, reducing the number of fibers to carry the load, resulting in the reduced retained tensile strength.

6.2 Recommendations

Tests should be conducted on this Hi-Nicalon/PyC/HyprSiC composite with a center hole without a seal-coat applied to the hole to examine the material's behavior in this configuration, helping characterize the material's notch sensitivity. Maximum stress levels should also be increased to determine the upper limits of the S-N curve for both air and steam at the tested frequencies of 0.1 Hz, 1.0 Hz, and 10 Hz. The effects of thermal cycling on fatigue life should also be examined to determine the effects of fluctuating temperatures on the composite.

Appendix A

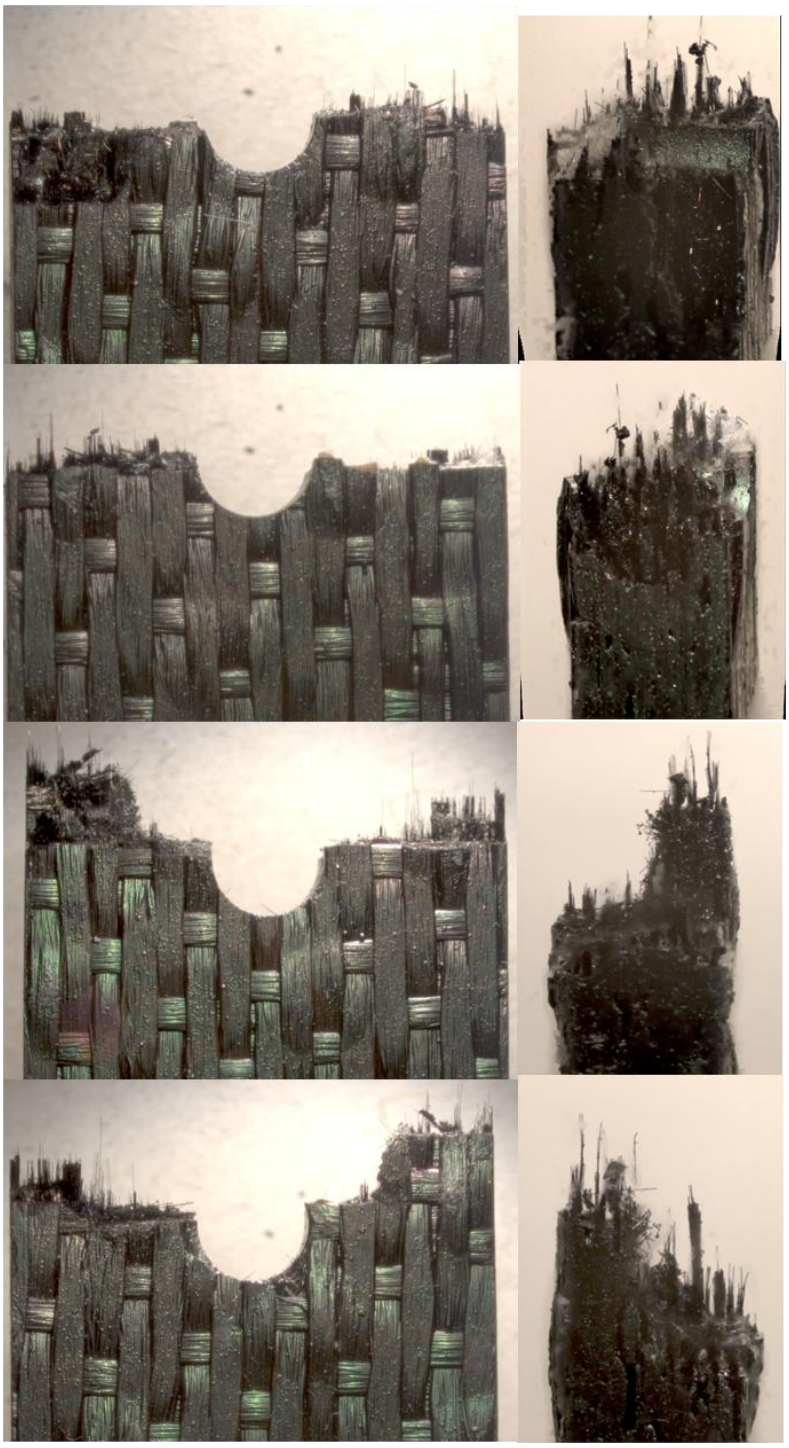

Figure 68: Optical micrographs of the fracture surfaces of specimen 11 tested in fatigue at 0.1 Hz in air at 1200°C. σ_{max} = 120 MPa, N_f = 22,195, t_f = 61.6 h

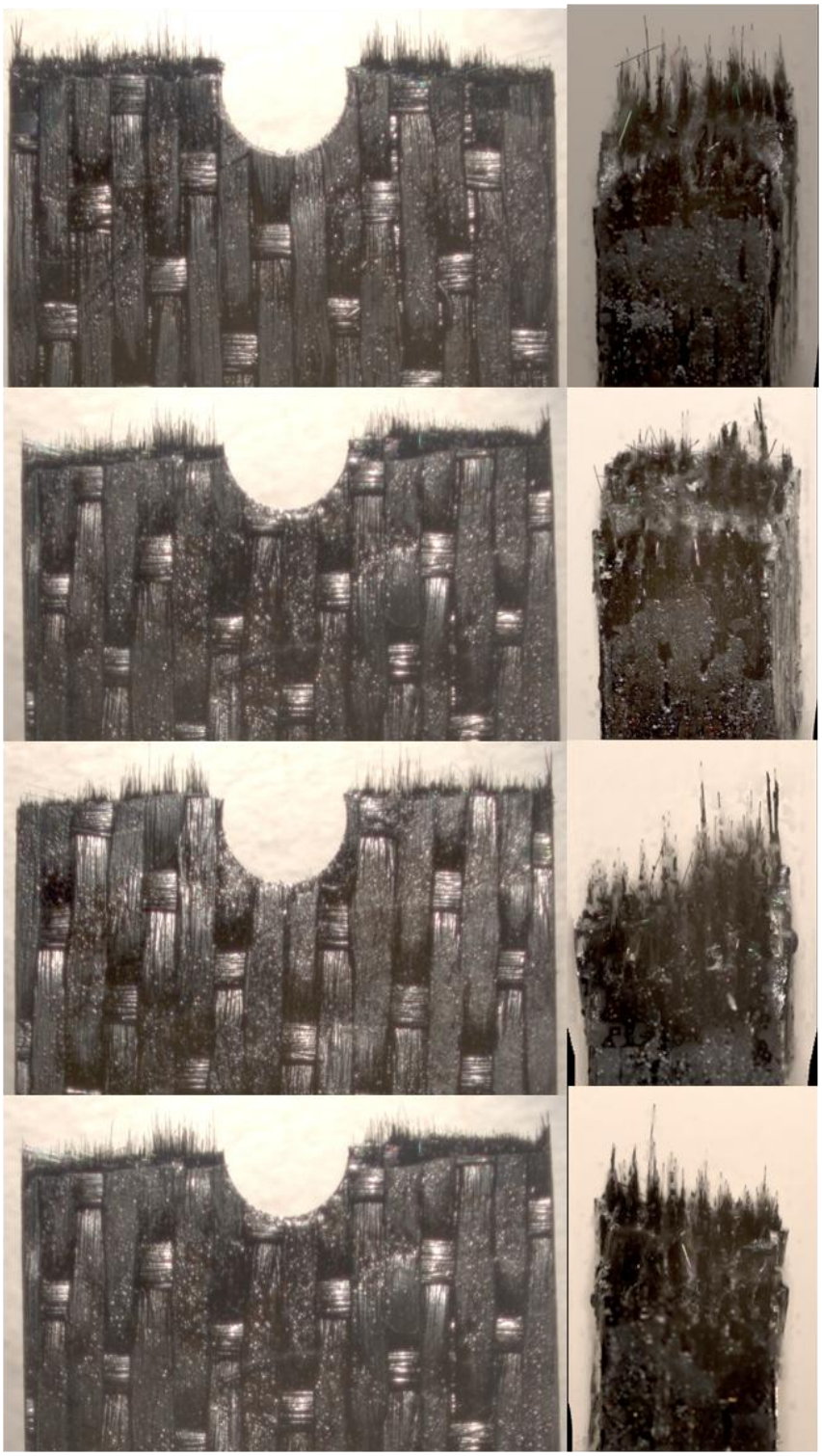

Figure 69: Optical micrographs of the fracture surfaces of specimen 12 tested in fatigue at 0.1 Hz in air at 1200°C. σ_{max} = 80 MPa, N_f = 100,000, t_f = 277.8 h

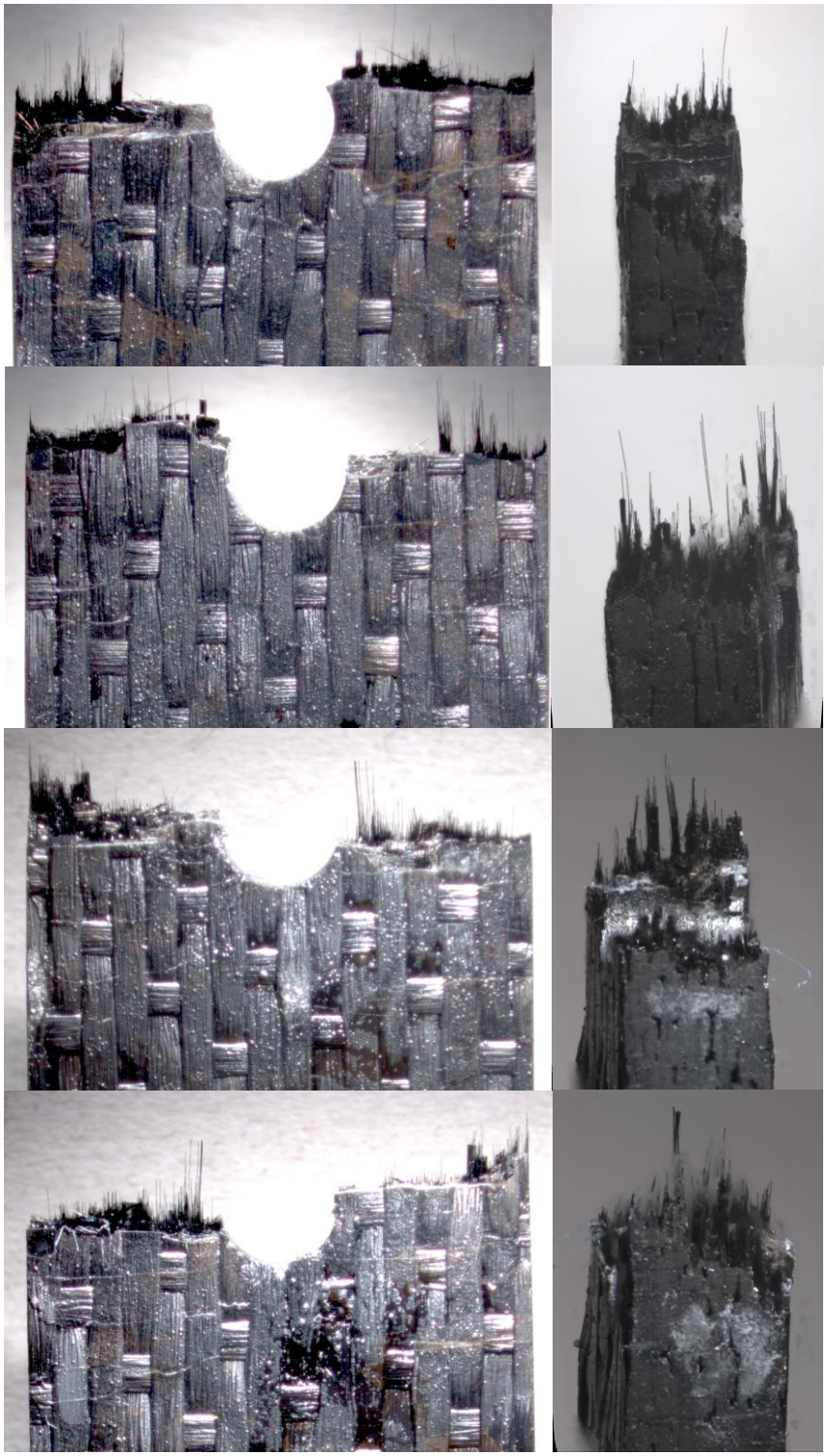

Figure 70: Optical micrographs of the fracture surfaces of specimen 13 tested in fatigue at 1.0 Hz in steam at 1200°C. σ_{max} = 120 MPa, N_f = 177,335, t_f = 49.3 h

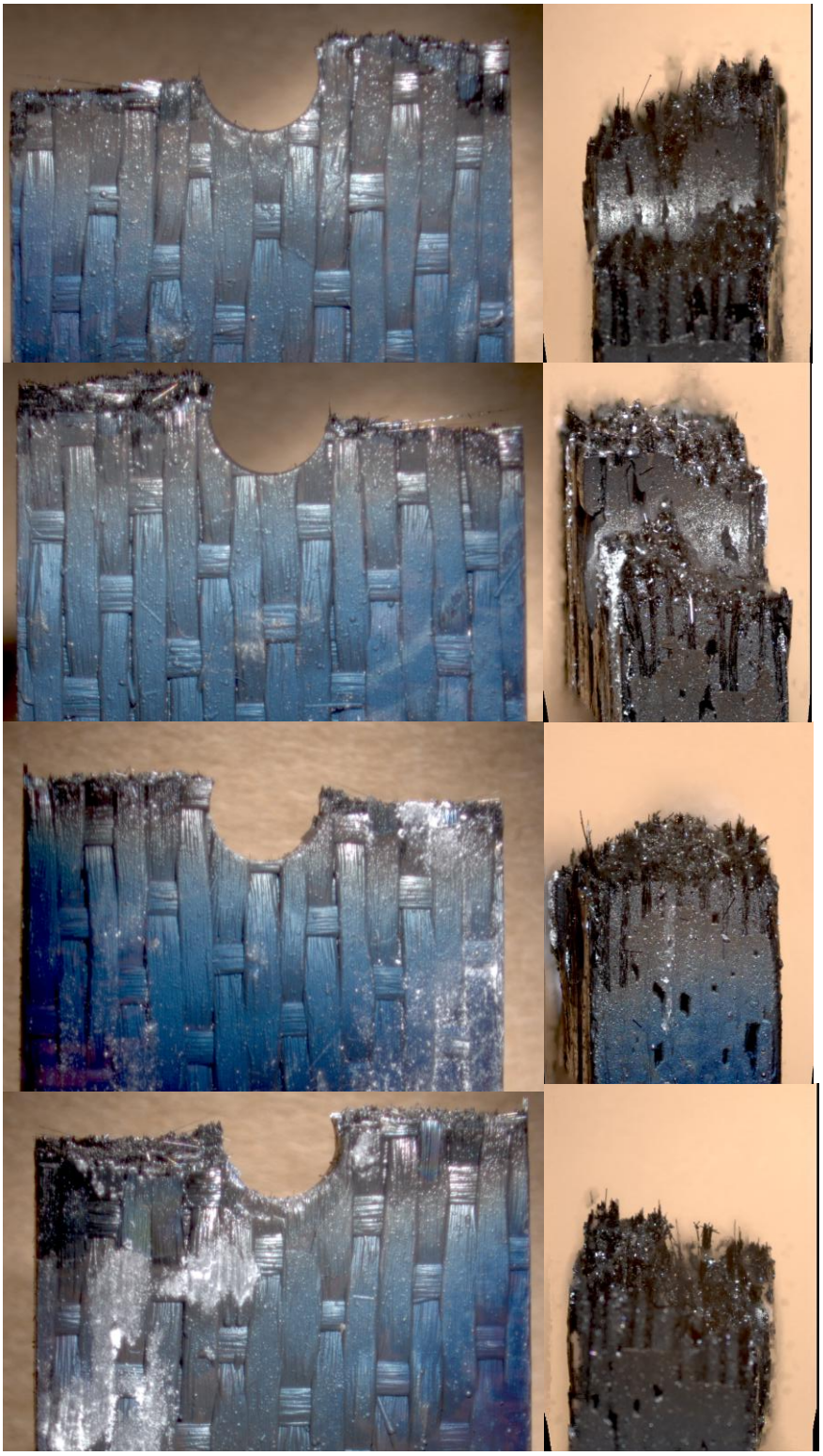

Figure 71: Optical micrographs of the fracture surfaces produced in tensile test to failure conducted at 0.05mm/sec at 1200°C air on specimen 14

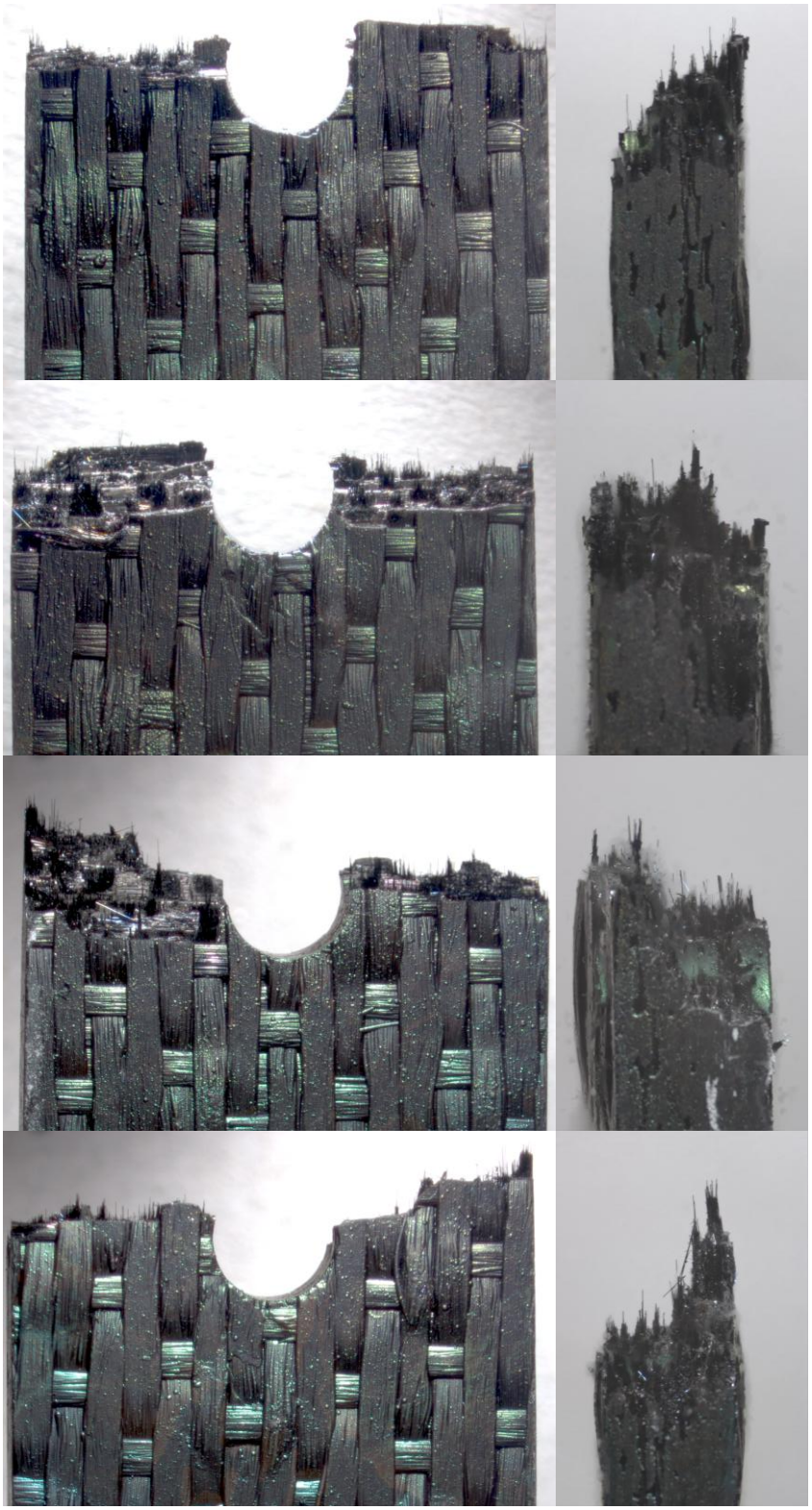

Figure 72: Optical micrographs of the fracture surfaces of specimen 15 tested in fatigue at 1.0 Hz in air at 1200°C. σ_{max} = 120 MPa, N_f = 113,522, t_f = 31.5 h

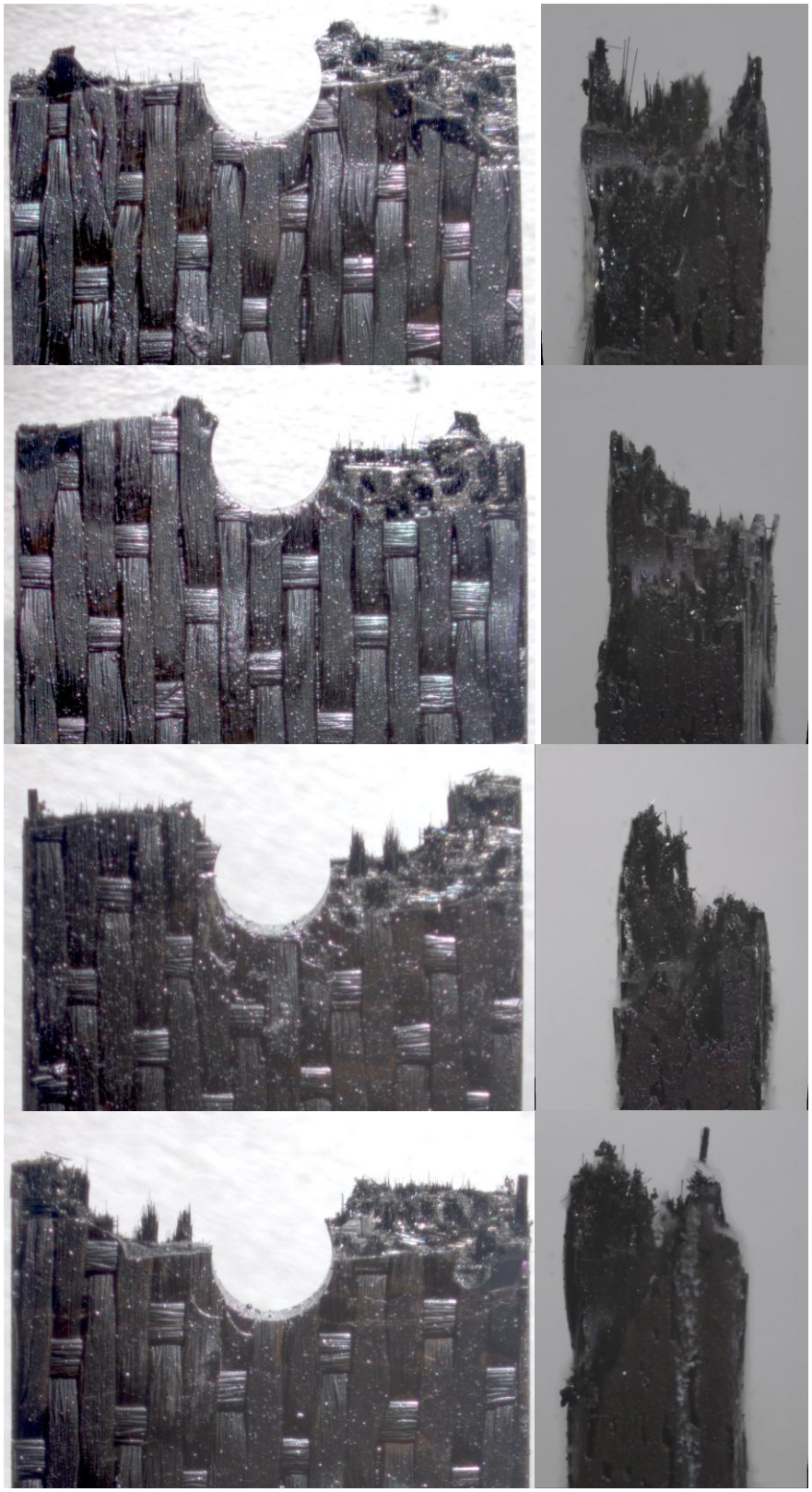

Figure 73: Optical micrographs of the fracture surfaces of specimen 16 tested in fatigue at 1.0 Hz in air at 1200°C. σ_{max} = 130 MPa, N_f = 104,000, t_f = 28.9 h

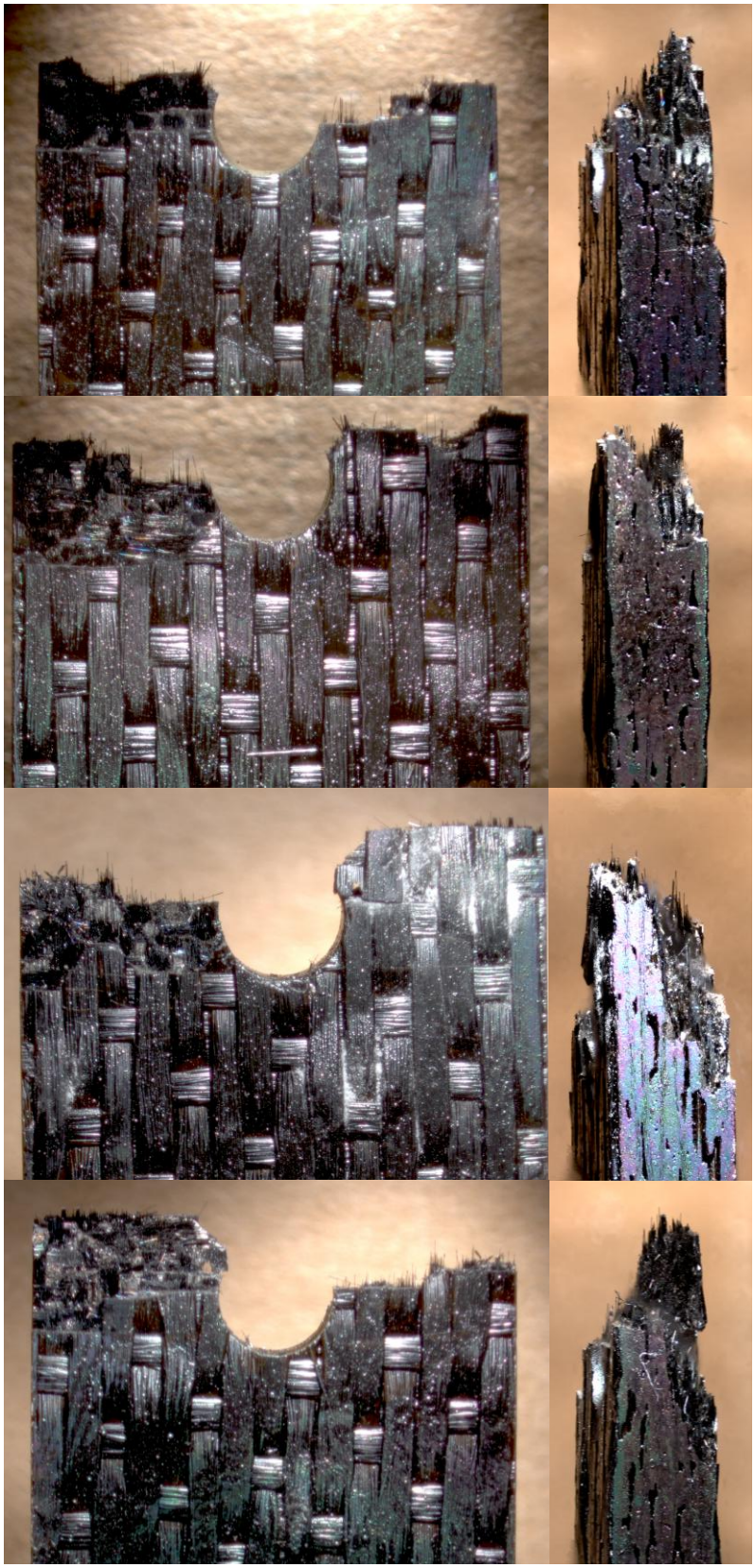

Figure 74: Optical micrographs of the fracture surfaces of specimen 18 tested in fatigue at 1.0 Hz in air at 1200°C. σ_{max} = 120 MPa, N_f = 77,575, t_f = 21.5 h

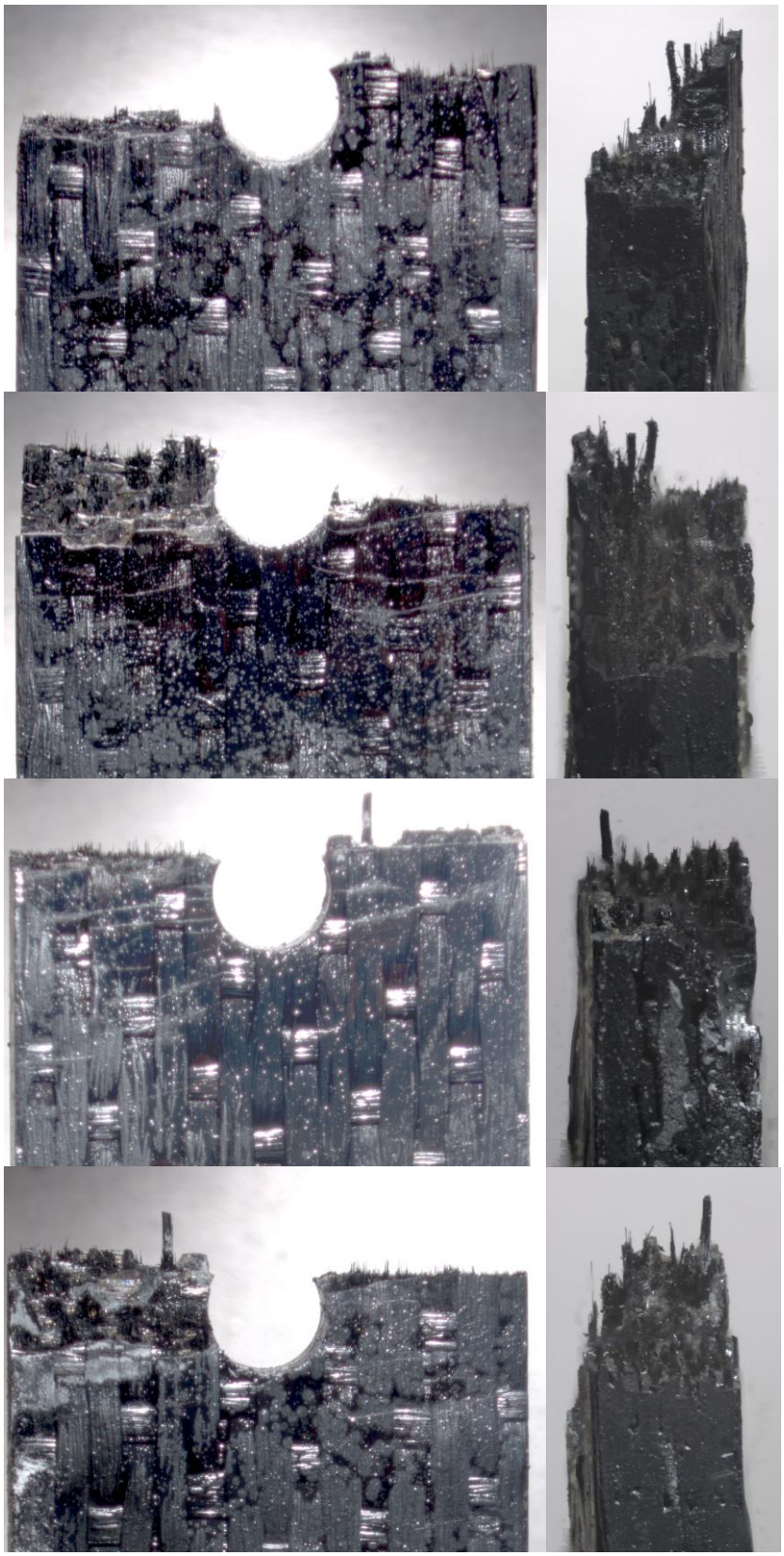

Figure 75: Optical micrographs of the fracture surfaces of specimen 32 tested in fatigue at 1.0 Hz in steam at 1200°C. σ_{max} = 130 MPa, N_f = 115,050, t_f = 32.0 h

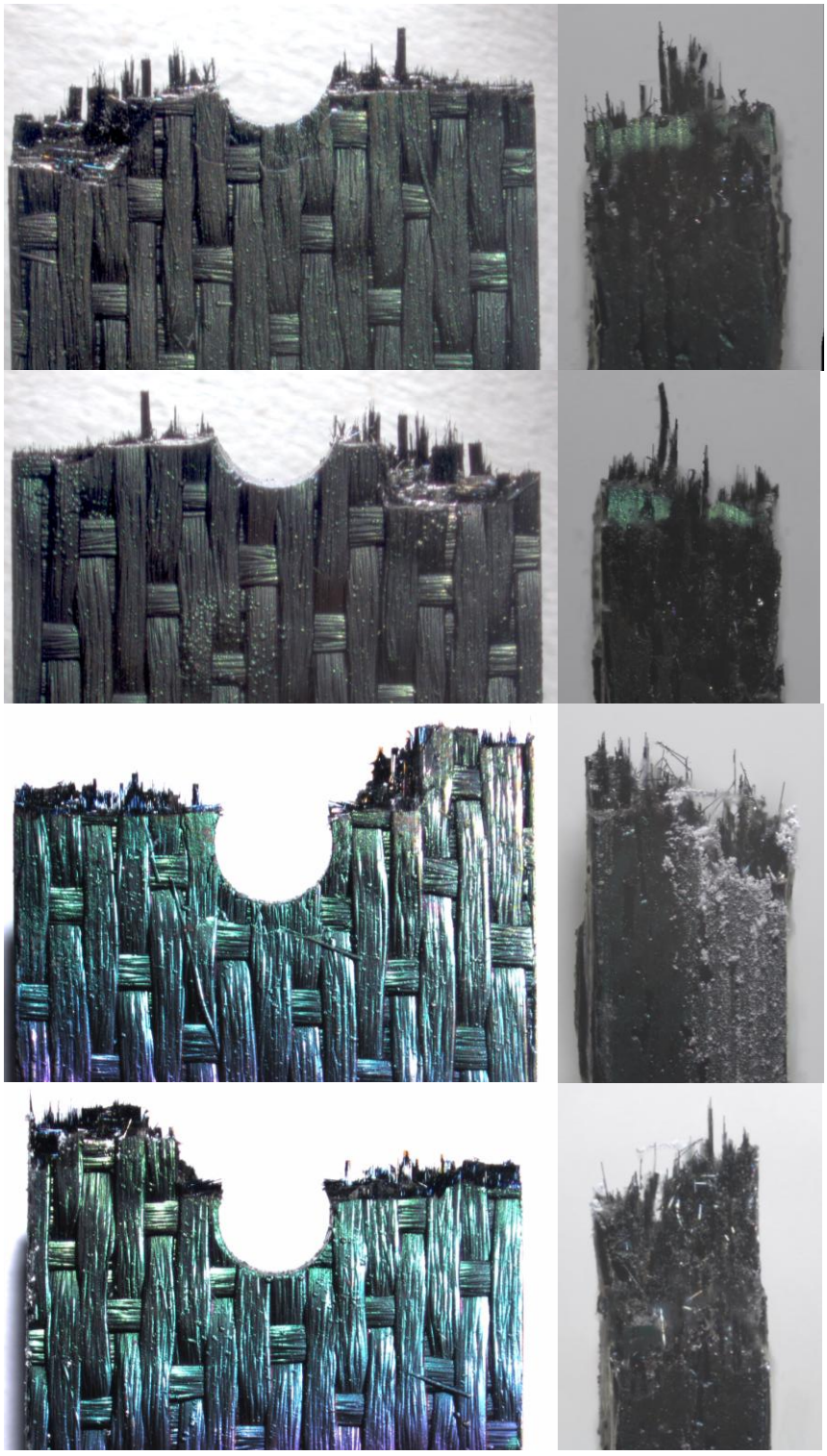

Figure 76: Optical micrographs of the fracture surfaces of specimen 33 tested in fatigue at 1.0 Hz in air at 1200°C. σ_{max} = 140 MPa, N_f = 105,421, t_f = 29.3 h

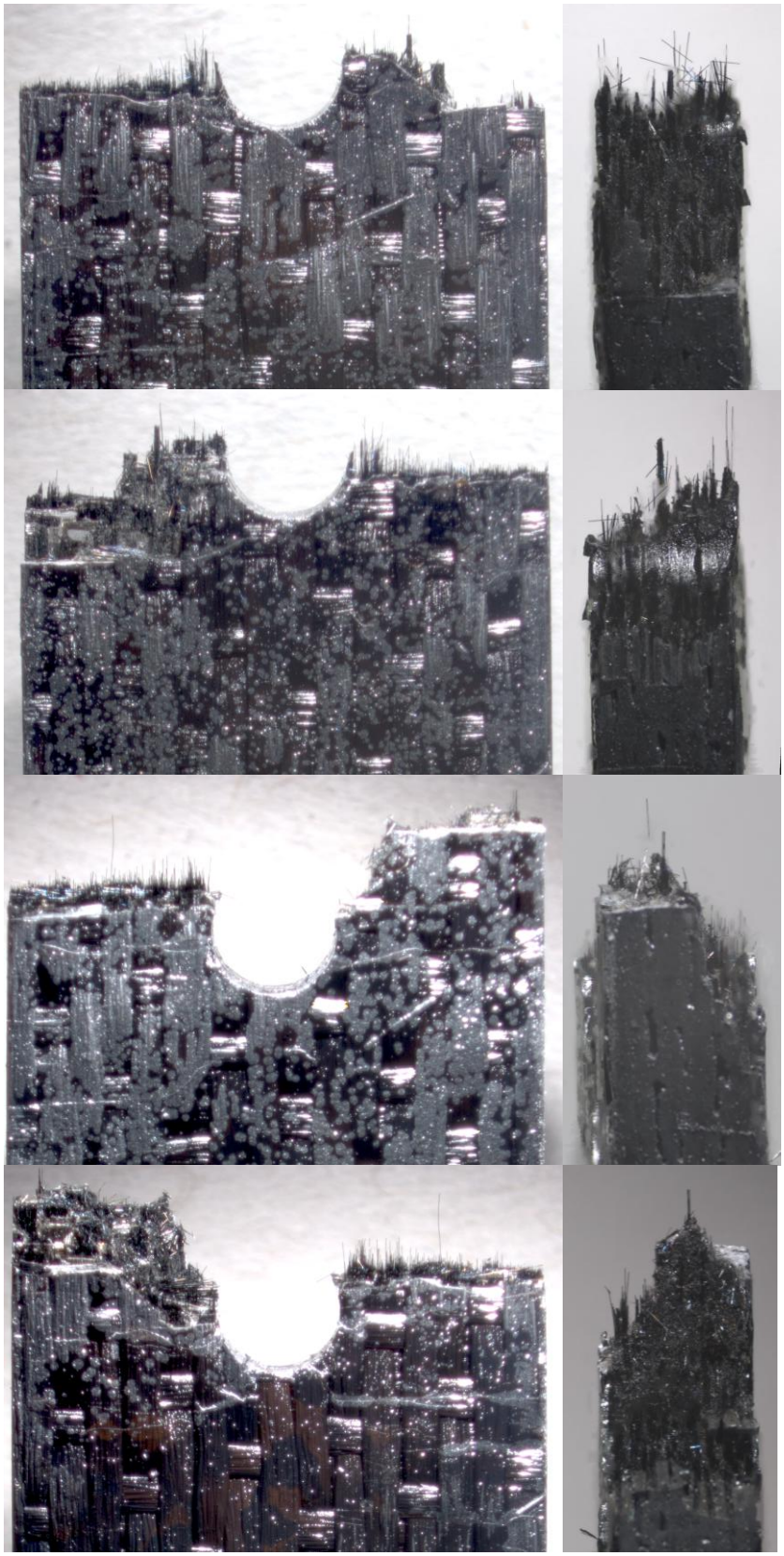

Figure 77: Optical micrographs of the fracture surfaces of specimen 34 tested in fatigue at 1.0 Hz in steam at 1200°C. σ_{max} = 140 MPa, N_f = 74,280, t_f = 20.6 h

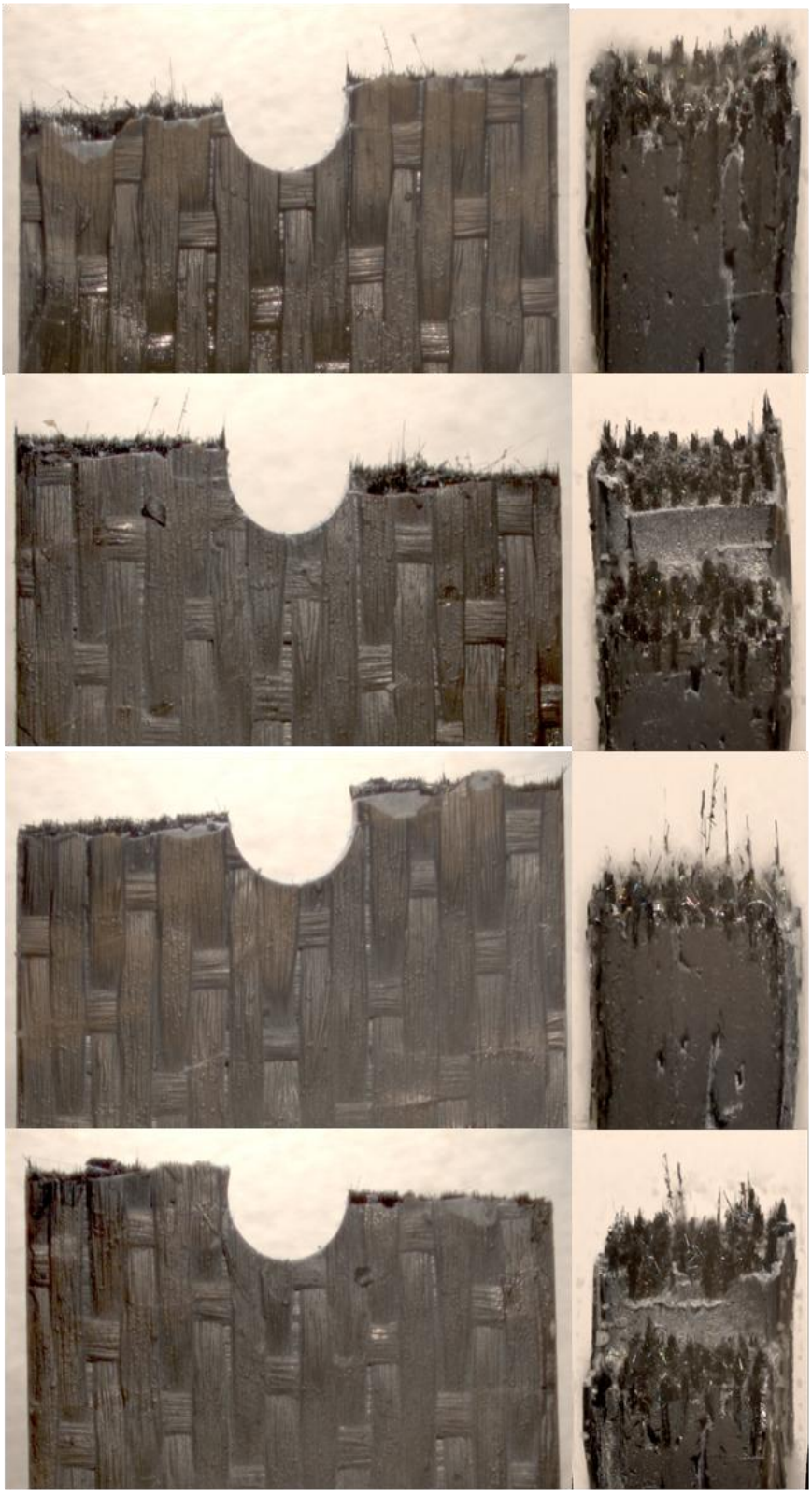

Figure 78: Optical micrographs of the fracture surfaces of specimen 35 tested in fatigue at 0.1 Hz in steam at 1200°C. σ_{max} = 100 MPa, N_f = 100,000, t_f = 277.8 h

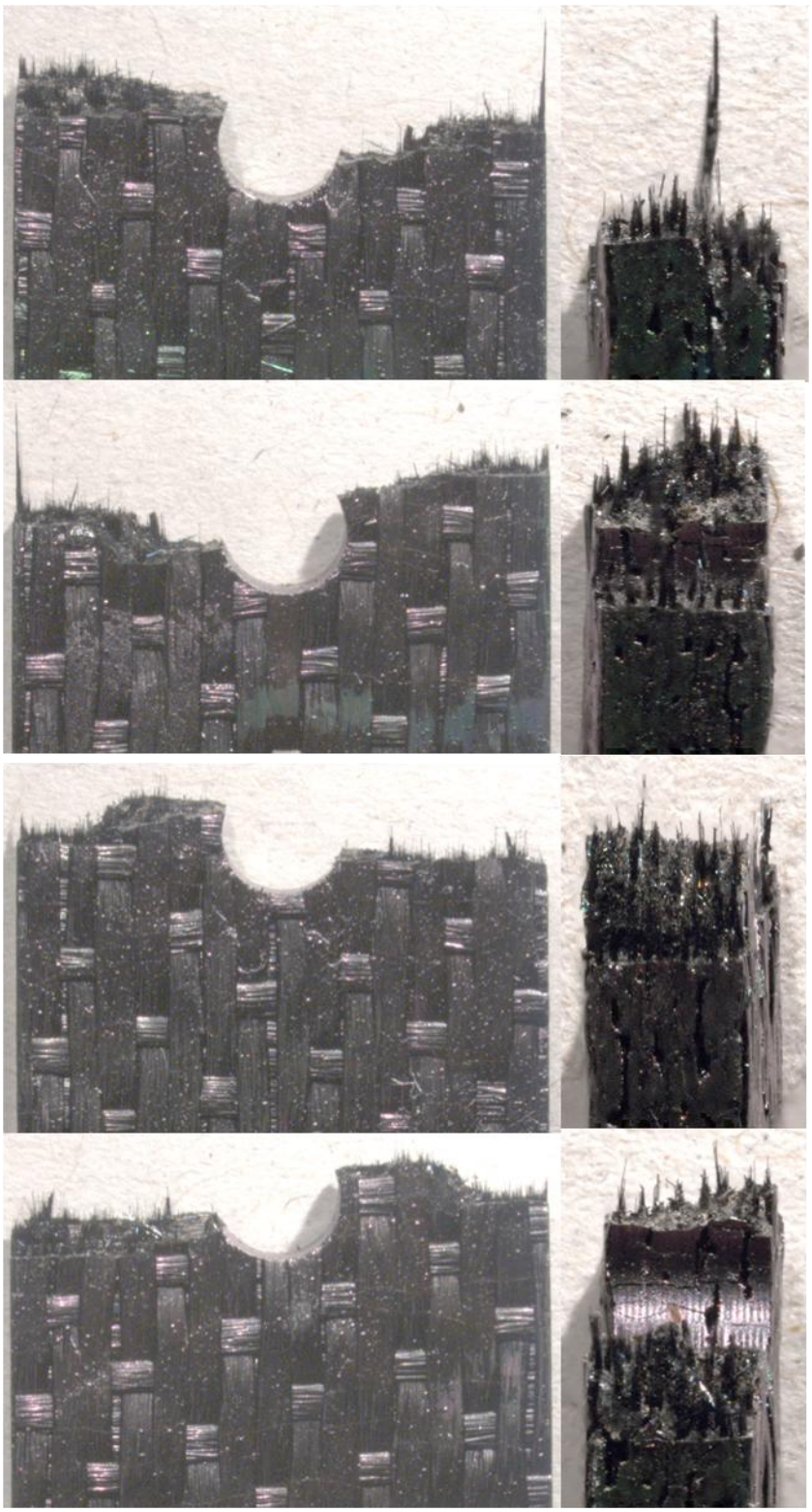

Figure 79: Optical micrographs of the fracture surfaces of specimen 36 tested in fatigue at 0.1 Hz in air at 1200°C. σ_{max} = 140 MPa, N_f = 29,694, t_f = 82.5 h

Figure 80: Optical micrographs of the fracture surfaces of specimen 37 tested in fatigue at 1.0 Hz in air at 1200°C. σ_{max} = 100 MPa, N_f = 200,000, t_f = 55.6 h

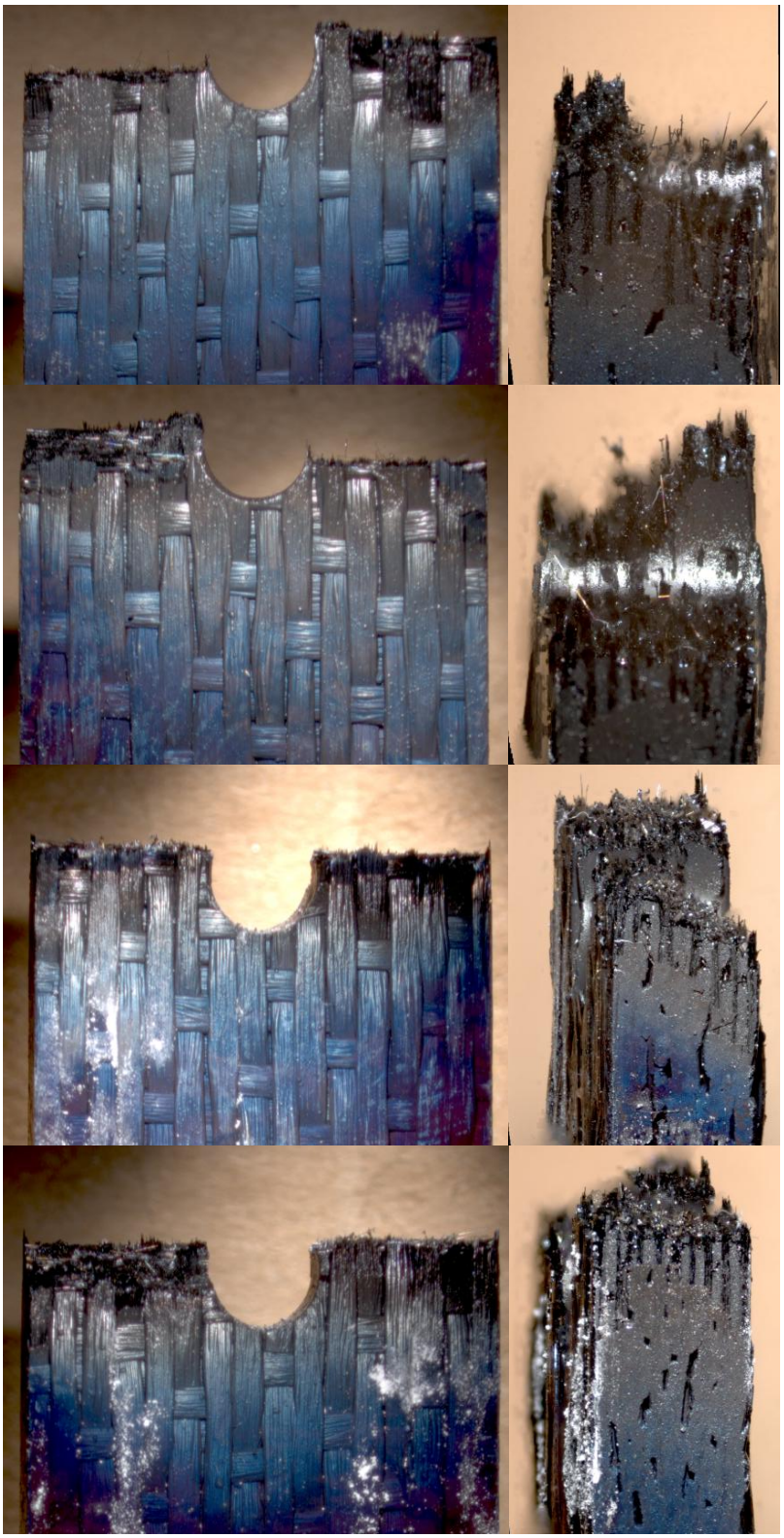

Figure 81: Optical micrographs of the fracture surfaces produced in tensile test to failure conducted at 0.05mm/sec at 1200°C air on specimen 38

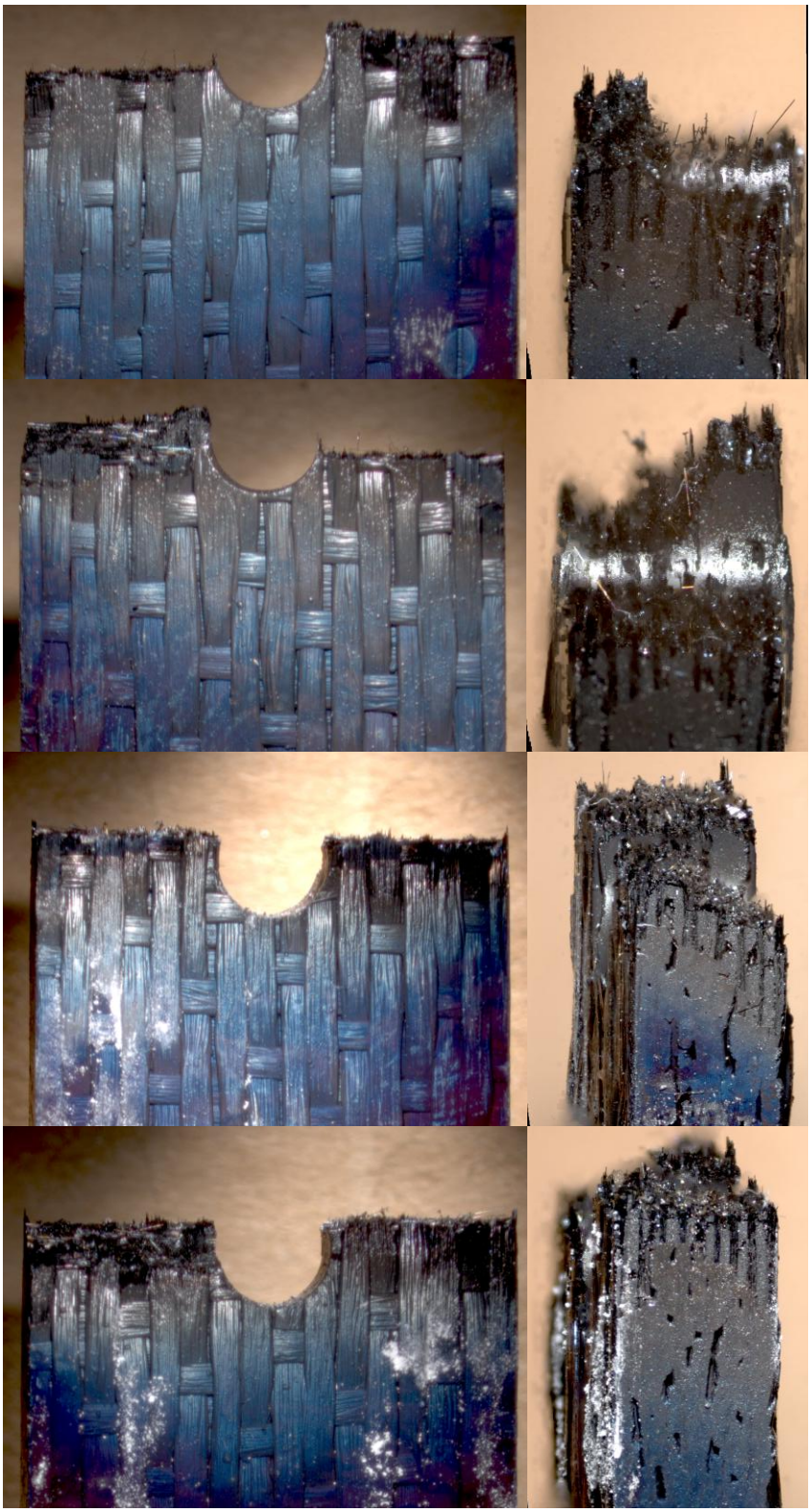

Figure 82: Optical micrographs of the fracture surfaces of specimen 41 tested in fatigue at 1.0 Hz in air at 1200°C. σ_{max} = 140 MPa, N_f = 43,116, t_f = 12.0 h

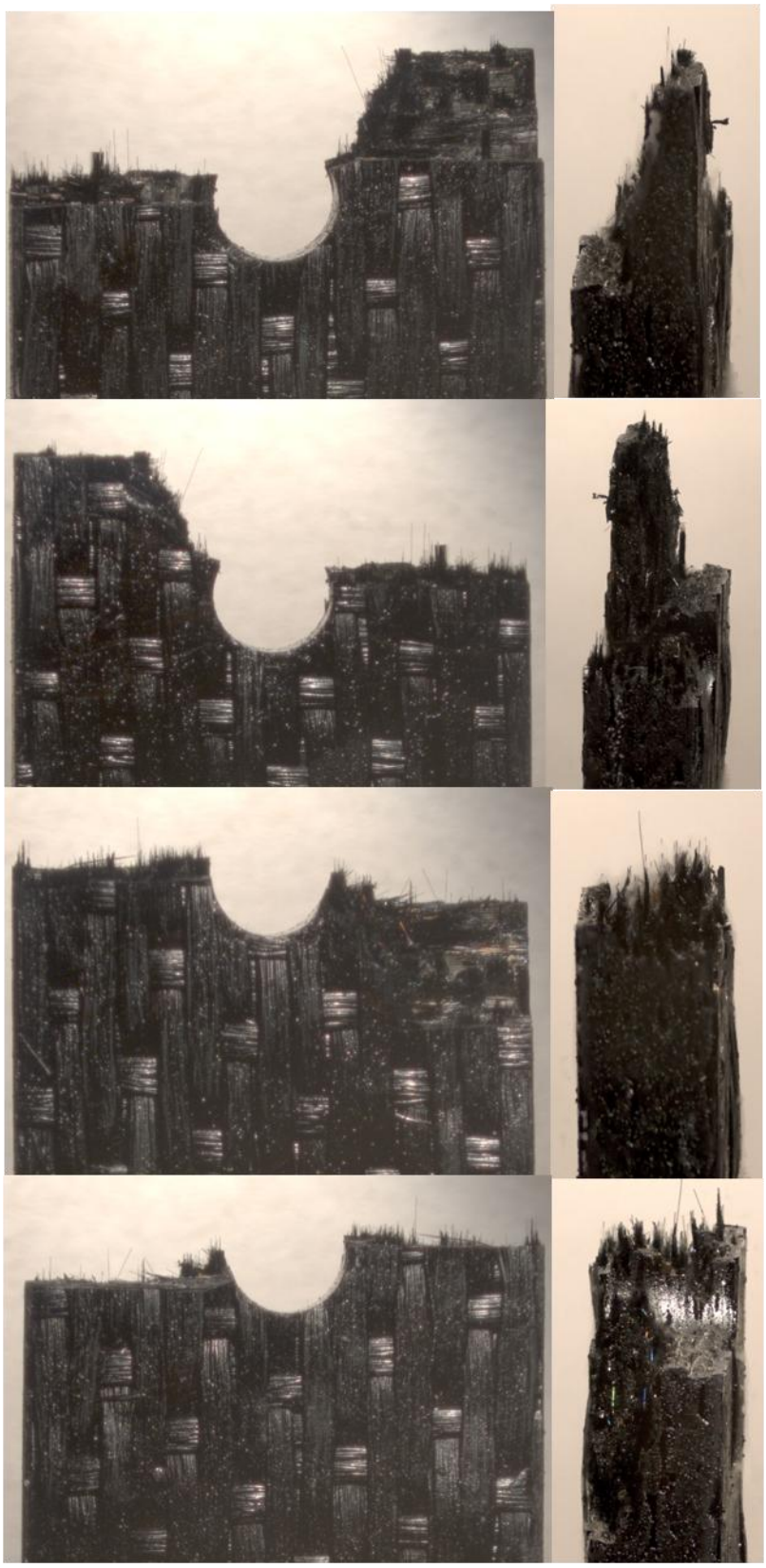

Figure 83: Optical micrographs of the fracture surfaces of specimen 42 tested in fatigue at 0.1 Hz in air at 1200°C. σ_{max} = 140 MPa, N_f = 51,238, t_f = 142.3 h

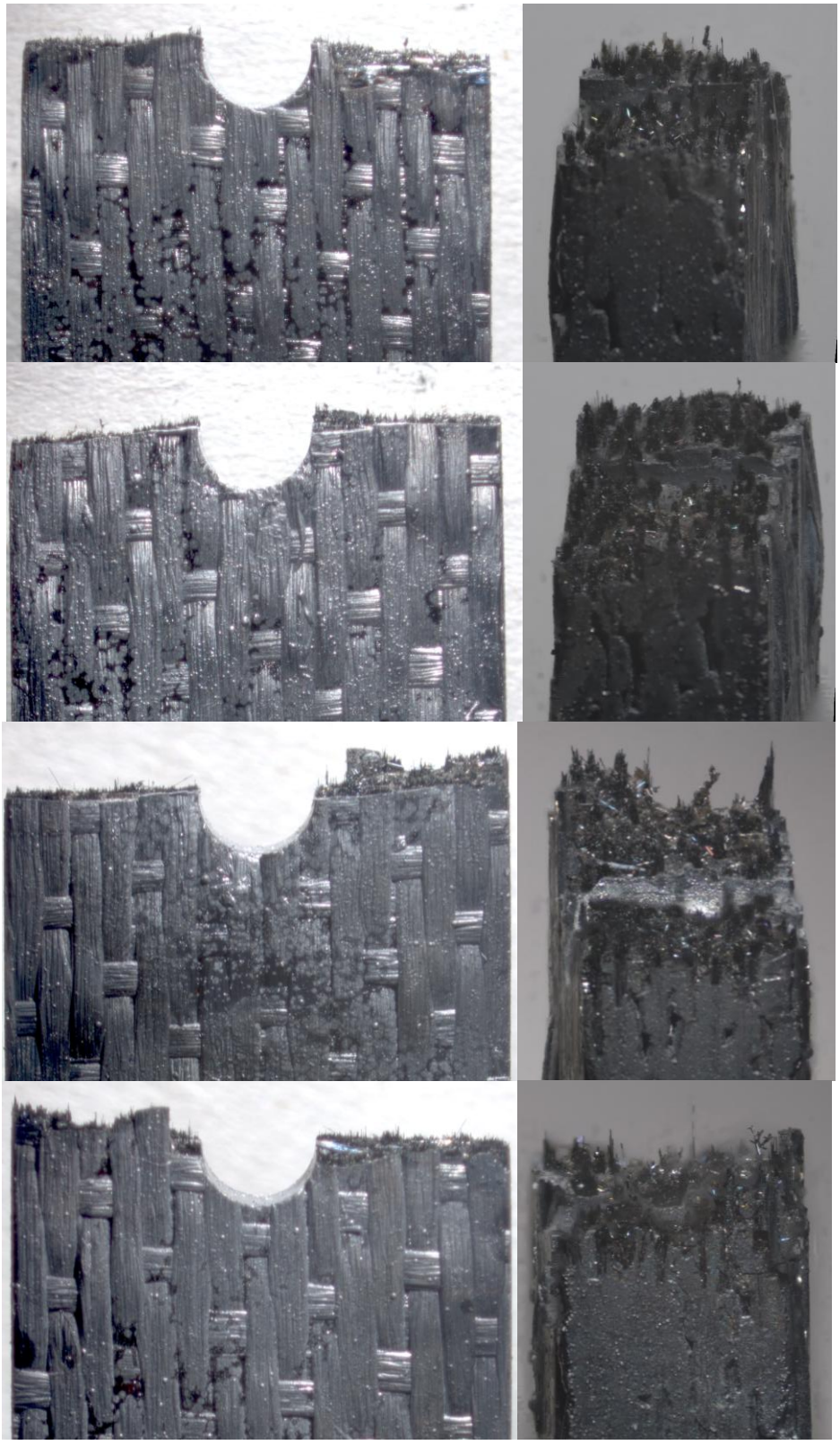

Figure 84: Optical micrographs of the fracture surfaces of specimen 43 tested in fatigue at 1.0 Hz in steam at 1200°C. σ_{max} = 100 MPa, N_f = 200,000, t_f = 55.6 h

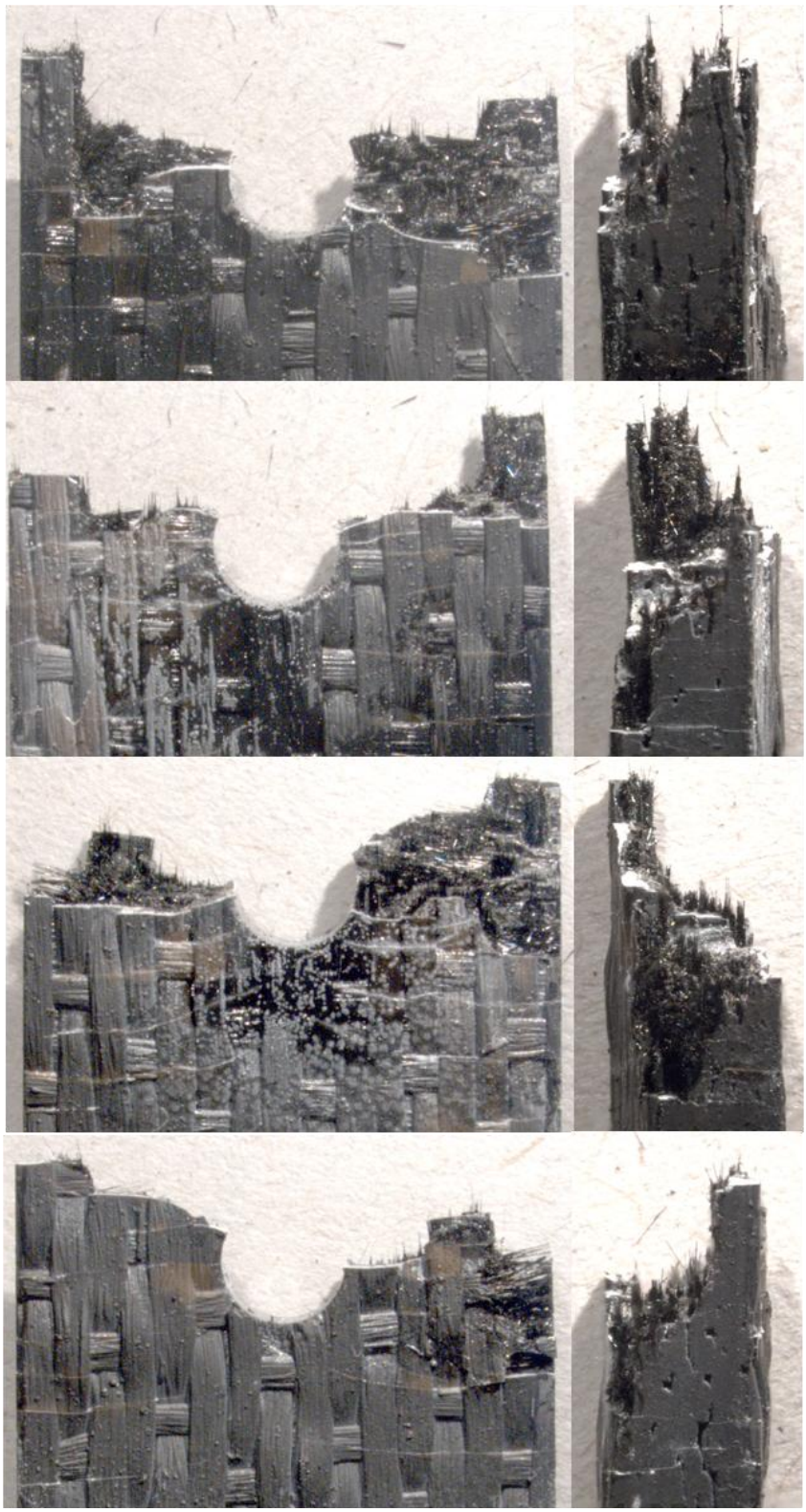

Figure 85: Optical micrographs of the fracture surfaces of specimen 44 tested in fatigue at 0.1 Hz in steam at 1200°C. σ_{max} = 120 MPa, N_f = 44,515, t_f = 123.7 h

Figure 86: Optical micrographs of the fracture surfaces produced in tensile test to failure conducted at 0.05mm/sec at 1200°C air on specimen 45

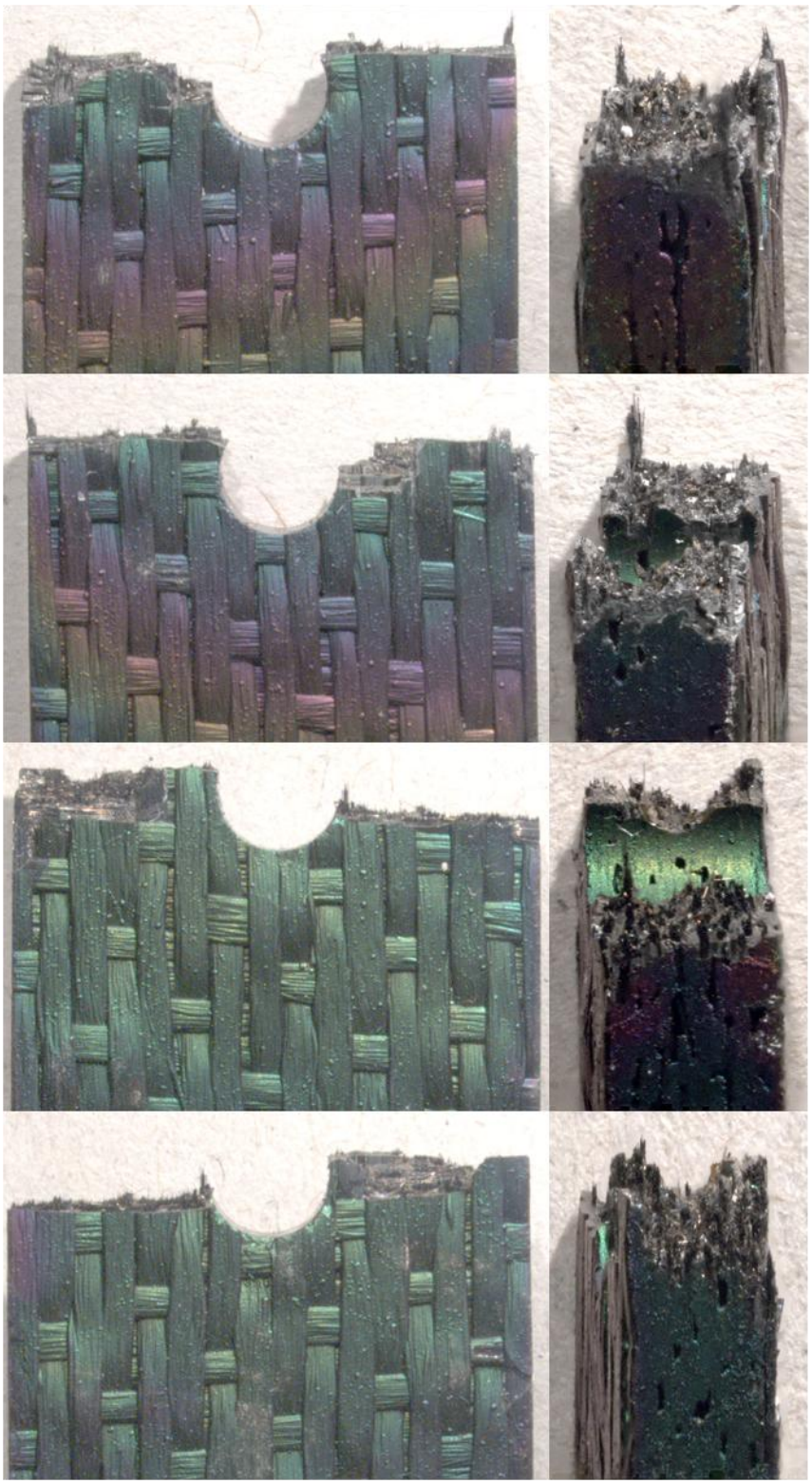

Figure 87: Optical micrographs of the fracture surfaces of specimen 46 tested in fatigue at 10 Hz in steam at 1200°C. σ_{max} = 140 MPa, N_f = 26,485, t_f = 0.7 h

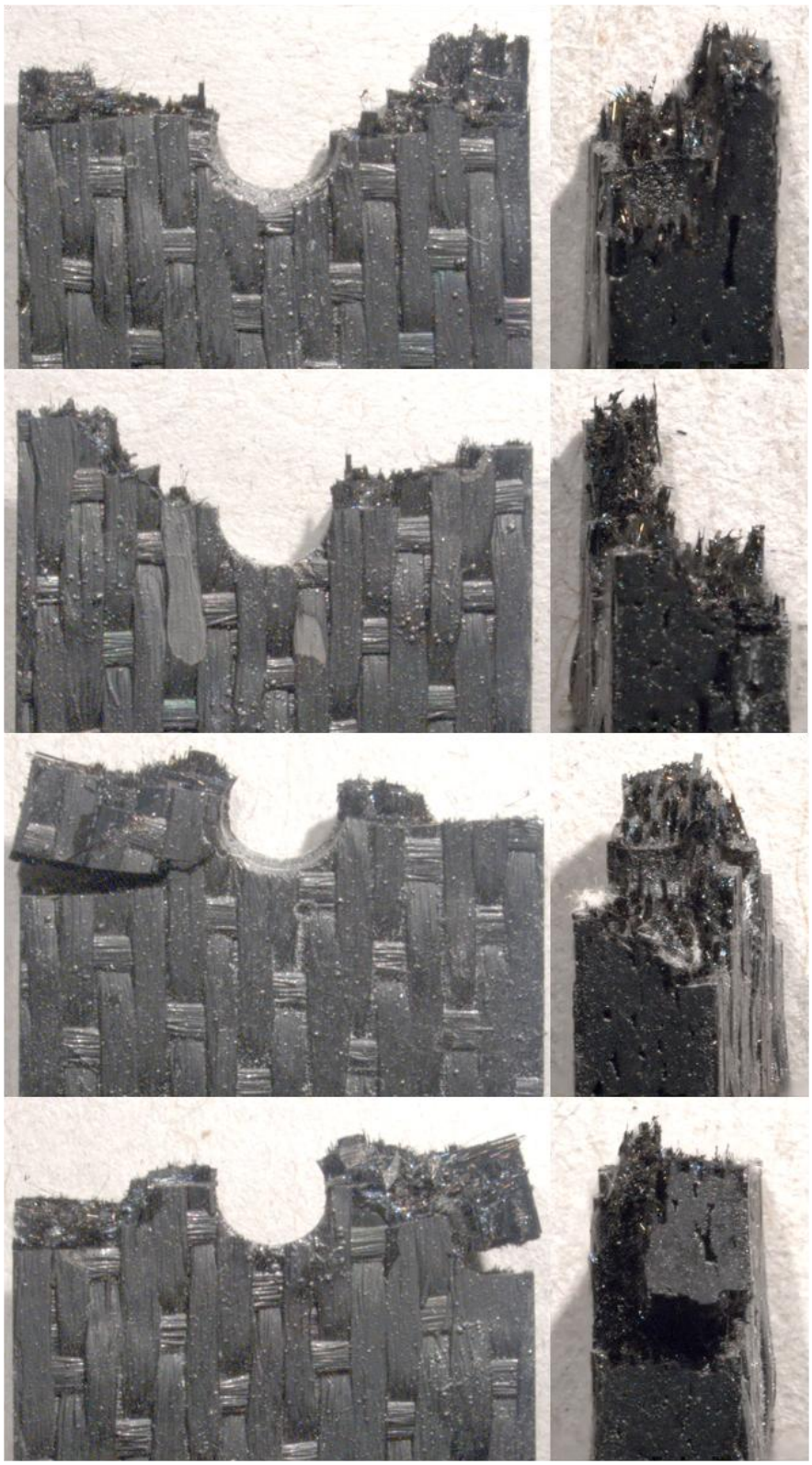

Figure 88: Optical micrographs of the fracture surfaces of specimen 47 tested in fatigue at 10 Hz in air at 1200°C. σ_{max} = 140 MPa, N_f = 200,000, t_f = 5.6 h

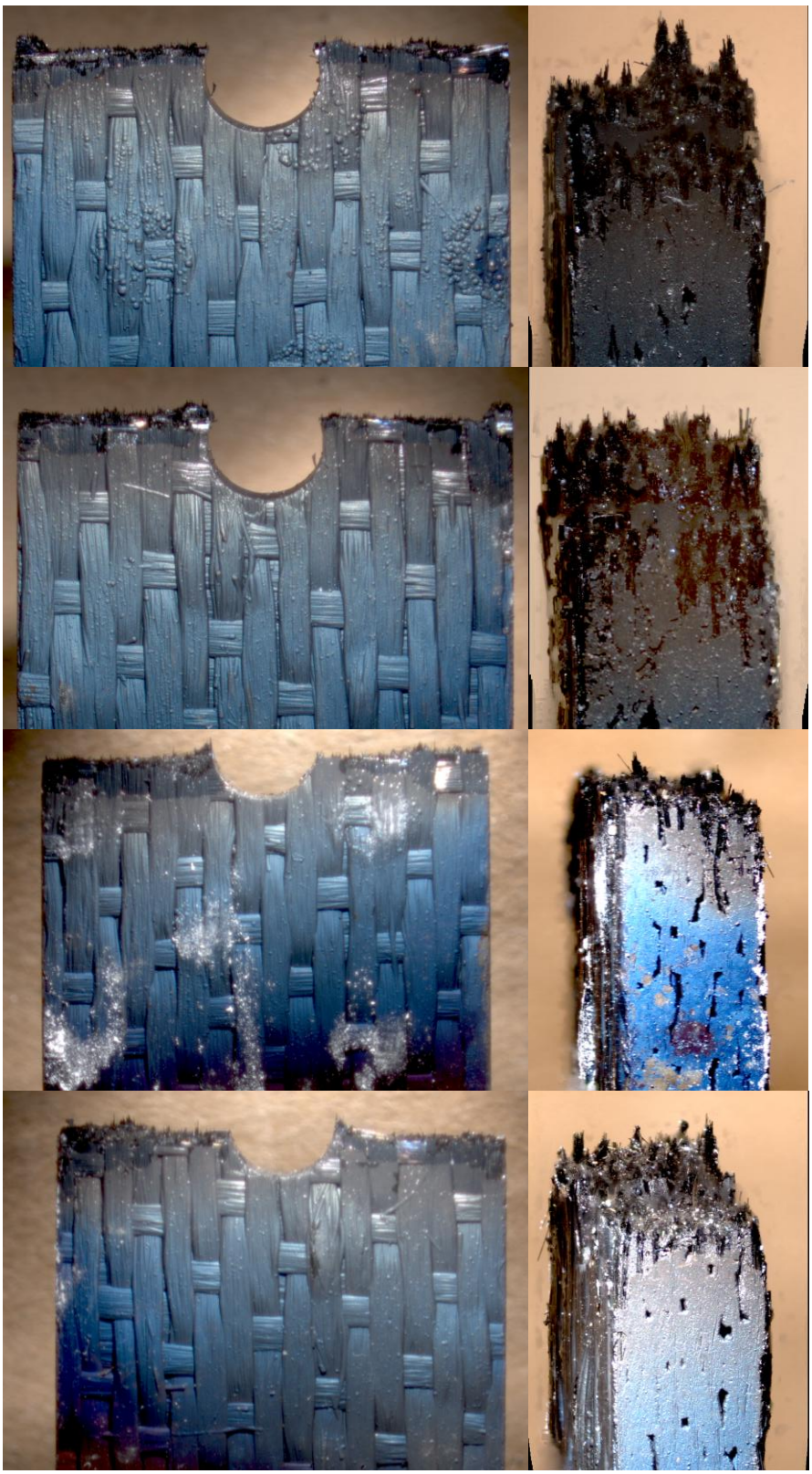

Figure 89: Optical micrographs of the fracture surfaces produced in tensile test to failure conducted at 0.05mm/sec at 1200°C air on specimen 48

Appendix B

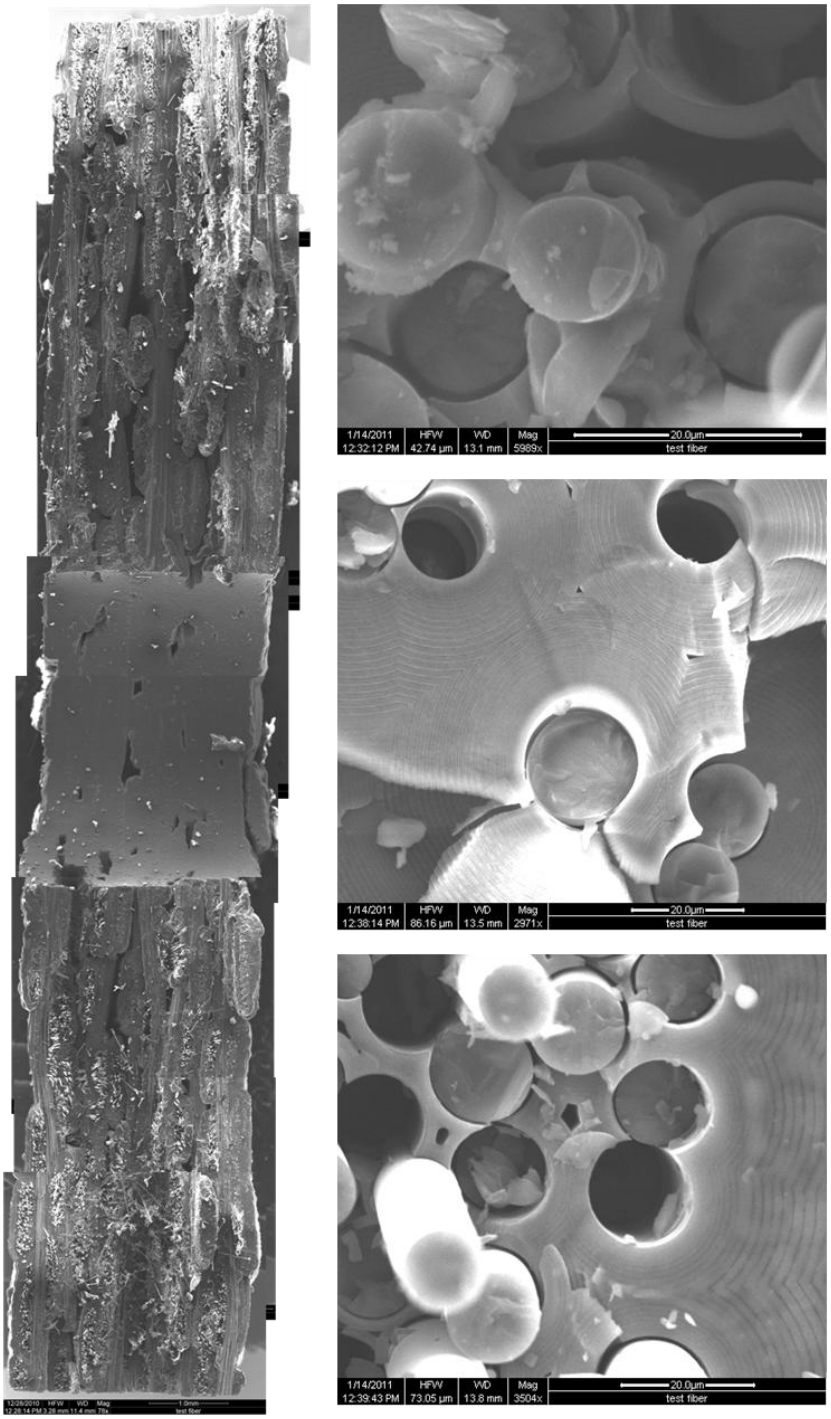

Figure 90: SEM micrographs of the fracture surfaces of specimen 15 tested in fatigue at 1.0 Hz in air at 1200°C. σ_{max} = 120 MPa, N_f = 113,522, t_f = 31.5 h

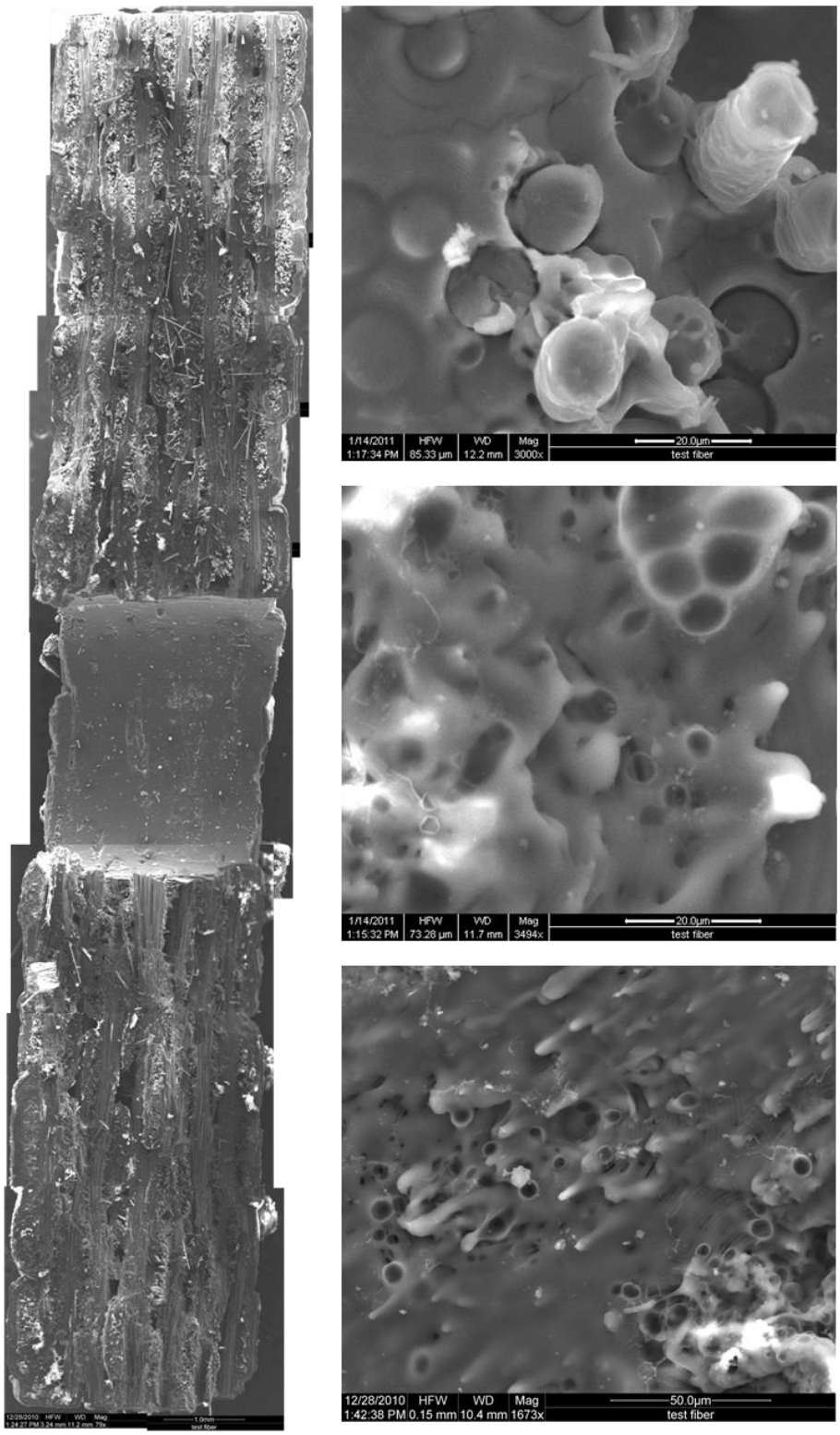

Figure 91: SEM micrographs of the fracture surfaces of specimen 32 tested in fatigue at 1.0 Hz in air at 1200°C. σ_{max} = 130 MPa, N_f = 115,050, t_f = 32.0 h

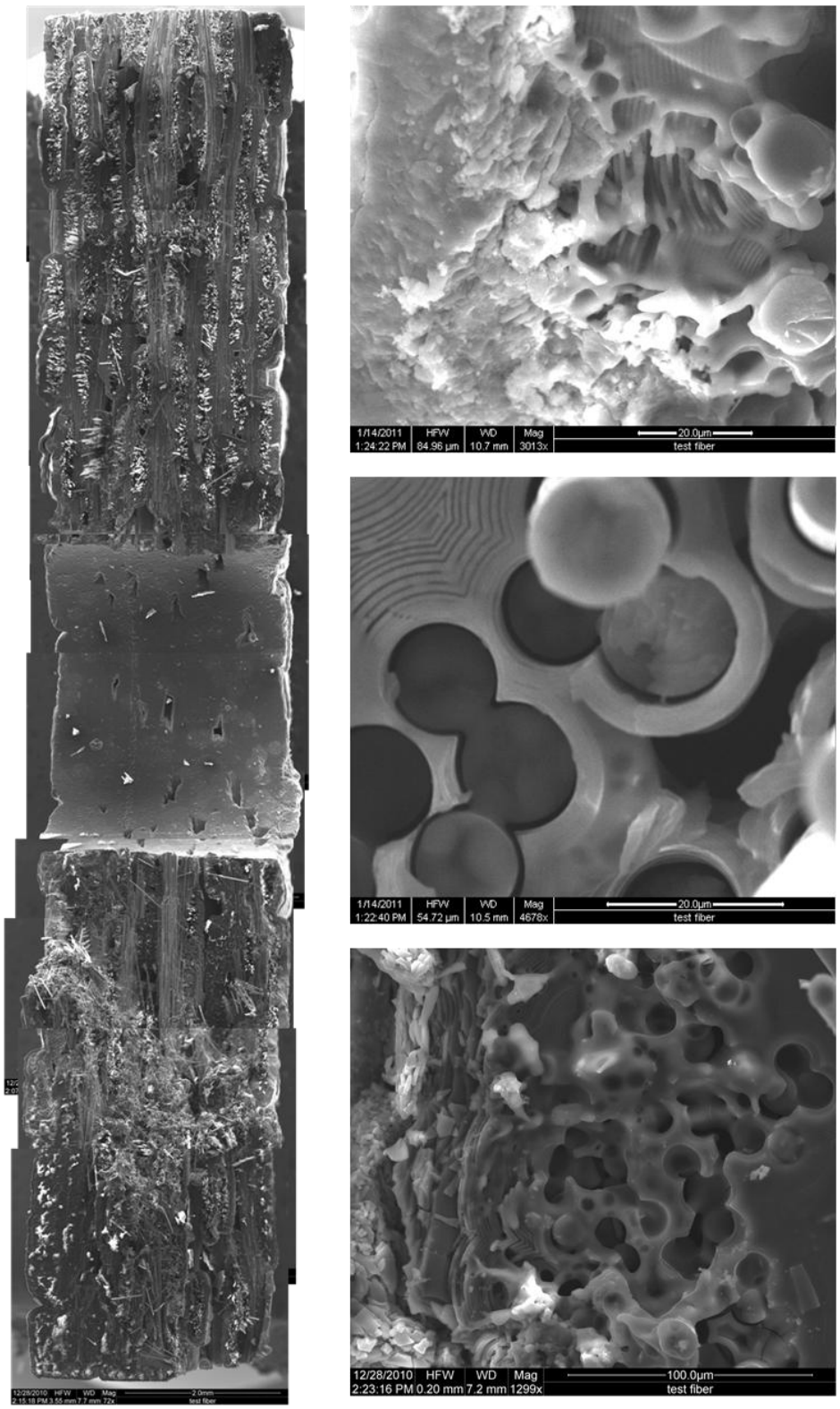

Figure 92: SEM micrographs of the fracture surfaces of specimen 34 tested in fatigue at 1.0 Hz in air at 1200°C. σ_{max} = 140 MPa, N_f = 74,280, t_f = 20.6 h

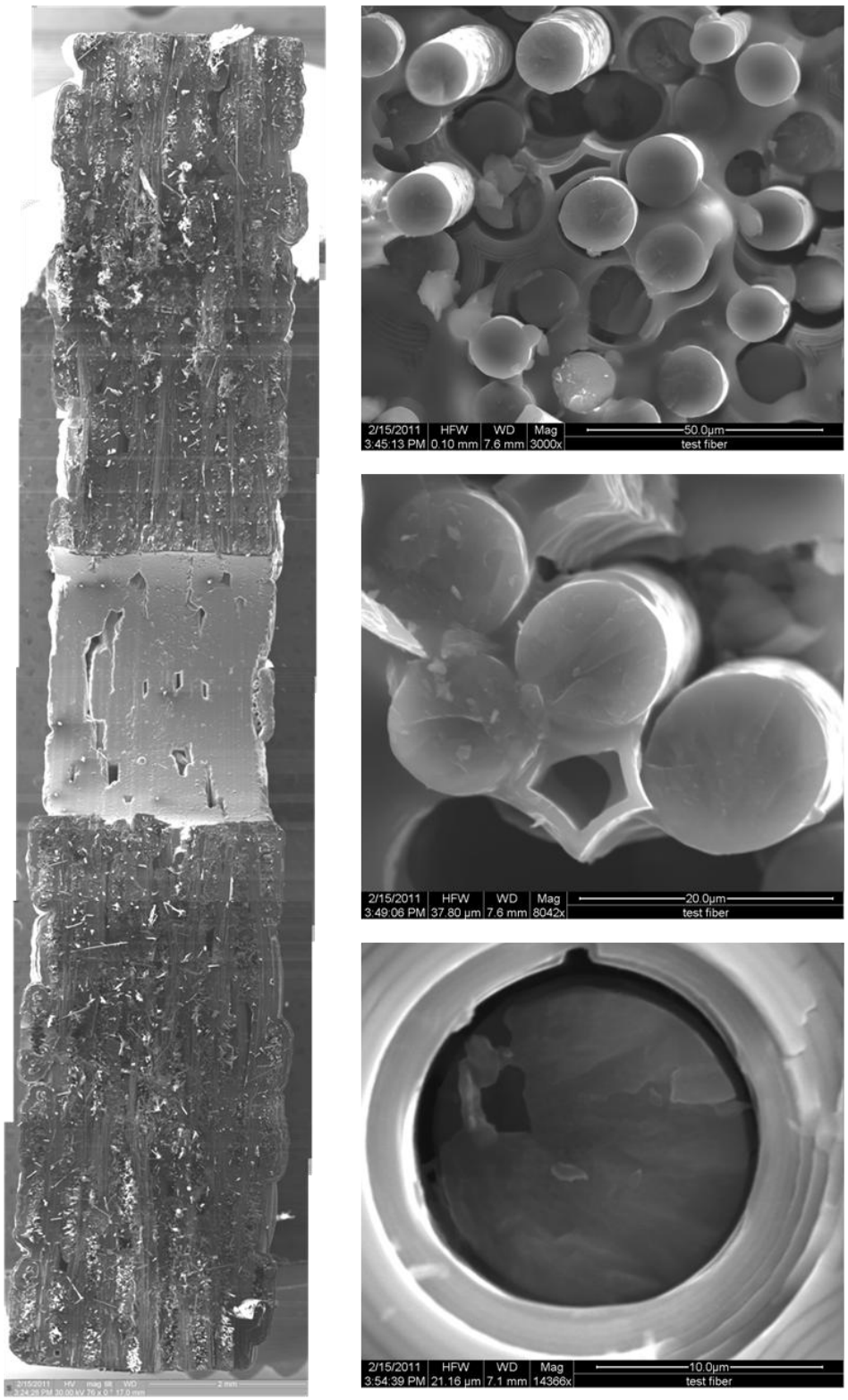

Figure 93: SEM micrographs of the fracture surfaces of specimen 36 tested in fatigue at 0.1 Hz in air at 1200°C. σ_{max} = 140 MPa, N_f = 29,694, t_f = 82.5 h

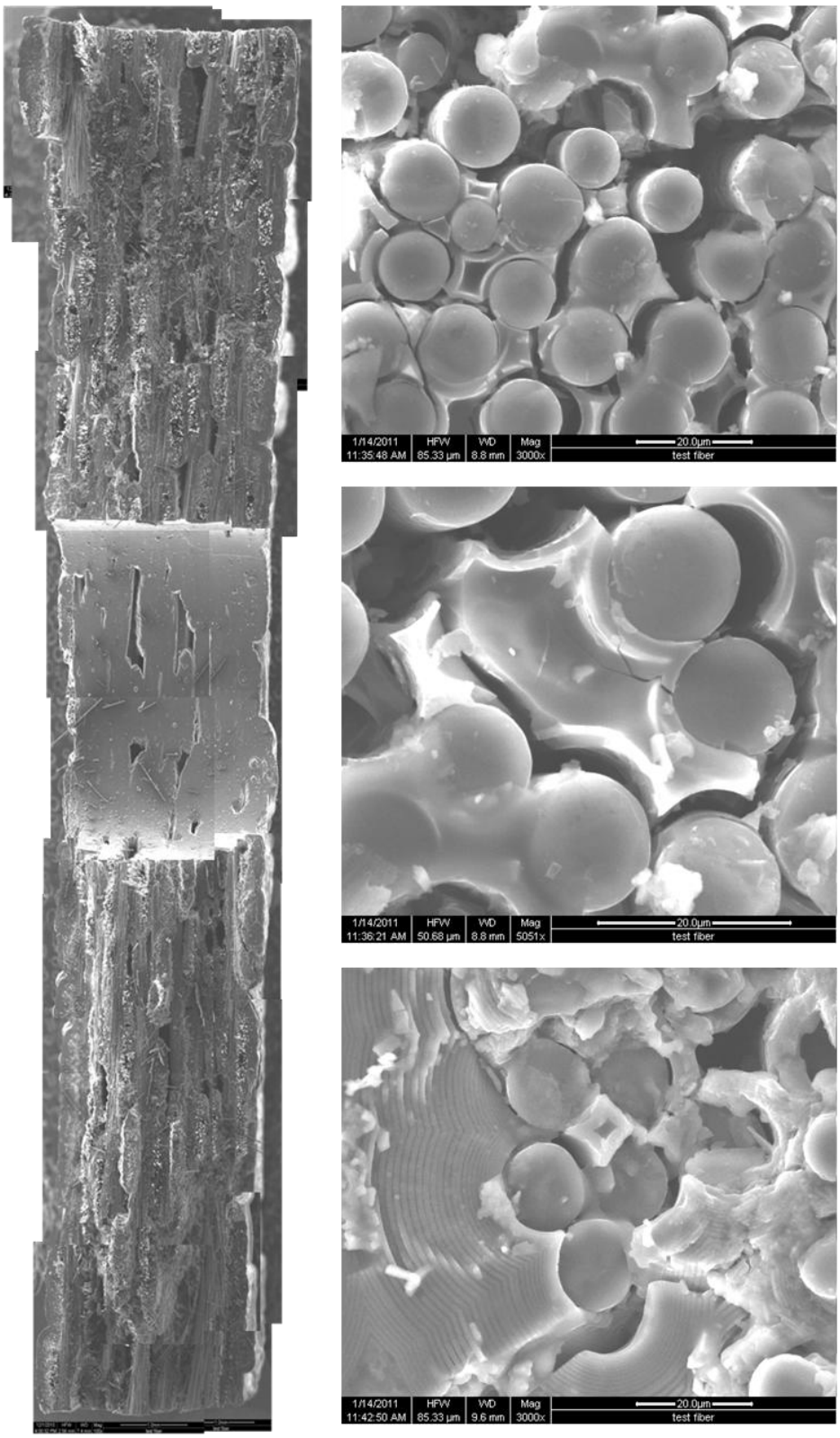

Figure 94: SEM micrographs of the fracture surfaces of specimen 41 tested in fatigue at 1.0 Hz in air at 1200°C. σ_{max} = 140 MPa, N_f = 43,116, t_f = 12.0 h

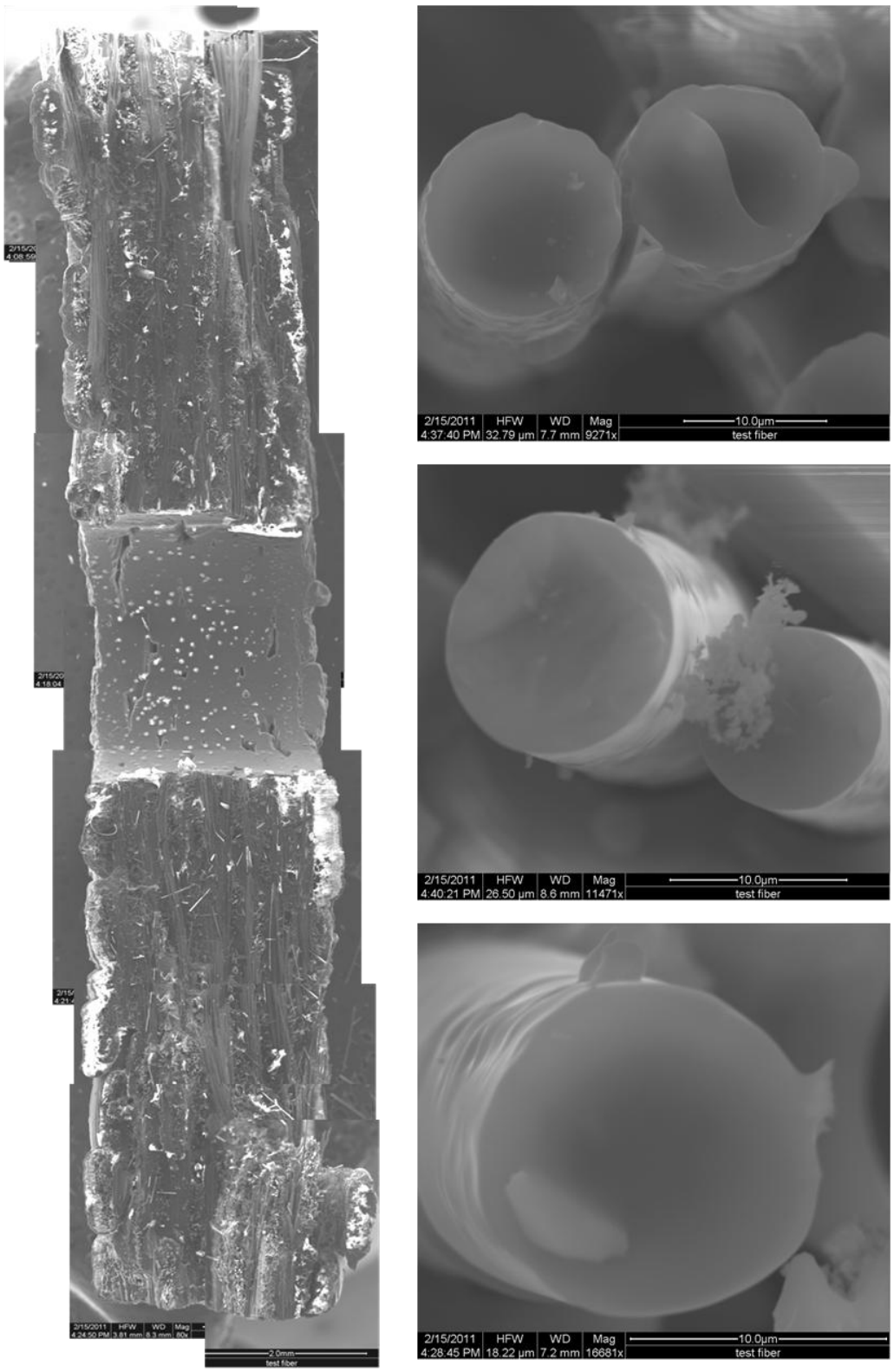

Figure 95: SEM micrographs of the fracture surfaces of specimen 44 tested in fatigue at 0.1 Hz in steam at 1200°C. σ_{max} = 120 MPa, N_f = 44,515, t_f = 123.7 h

Bibliography

1. AIAA Air Breathing Propulsion Technical Committee. *The Versatile Affordable Advanced Turbine Engines (VAATE) Initiative.* Reston: American Institute of Aeronautics and Astronautics, January 2006.

2. Anderson, T.L. *Fracture Mechanics: Fundamentals and Applications. Third Edition.* Boca Raton : Taylor & Francis Group, LLC, 2005.

3. Antti, M-L., and E.Lara-Curzio. "Effects of Notches, Specimen Size, and Fiber Orientation on the Monotonic Tensile Behavior of Composties at Amabient and Elevated Temperatures." *25th Annual Conference on Composites, Advanced Ceramics, Materials, and Structres, A: Ceramic Engineering and Sciience Proceedings*. Vol 22, Issue 3 (eds. M.Singh and T. Jessen), John Wiley & Sons Inc, Hoboken, NJ, 2001: 643-650.

4. Branco, C.M. *Elevated Temperature Fatigue of IN718: Effects of Stress Ratio and Frequency*. AGARD-CP-569, NATO, AGARD, SMP, 7 Rue Ancelle, 92200 Neuilly sur Seine, France, March 1996.

5. Chawla, K.K. *Ceramic Matrix Composites. Second Edition.* Boston : Kluwer Academic Publishers, 2003.

6. Christensen, Devon T. *Fatigue Behavior of an Advanced SiC/SiC Composite at Elevated Temperature in Air and Steam.* MS thesis, AFIT/GAE/ENY/09-D02. School of Engineering and Management, Air Force Institute of Technology (AU), Wright-Patterson AFB, OH, December 2009.

7. Delapasse, Jacob. *Fatigue Behavior of an Advanced SiC/SiC Composite with an Oxidation Inhibited Matrix at 1200°C in Air and Steam.* MS thesis, AFIT/GAE/ENY/10-M07. School of Engineering and Management, Air Force Institute of Technology (AU), Wright-Patterson AFB, OH, March 2010.

8. DiCarlo, J.A., H-M Yun, G.N. Morscher, and R.T Bhatt. "SiC/SiC Composites for 1200°C and Above." *Handbook of Ceramic Composites.* 2005.

9. Geels, Kay. *Metallographic and Materialographic Specimen Preparation, Light Microscopy, Image Analysis and Hardness Testing.* Lancaster, PA: ASTM International, 2007.

10. Genin, G.M. and J.W. Hutchinson. "*Composite Laminates in Plane Stress: Constitutive Modeling and Stress Redistribution due to Matrix Cracking*." *Journal of the American Ceramic Society,* 80, 1997: 1245-1255.

11. Hoeppner, D. W. *History and Prognosis of Material Discontinuity Effects on Engine Components Structural Integrity.* AGARD-R-790, NATO, AGARD, SMP, 7 Rue Ancelle, 92200 Neuilly sur Seine, France, April 1993.

12. Knauf, Michael. *Fatigue Behavior of a SiC/SiC Composite at 1000°C in Air and Steam.* MS thesis, AFIT/GAE/ENY/10D-01. School of Engineering and Management, Air Force Institute of Technology (AU), Wright Patterson AFB, OH, December 2010.

13. Knauf, M.W., private communications (2010)

14. Kramb, V.A., R John, and L.P. Zawada. "Notched Fracture Behavior of an Oxide/Oxide Ceramic-Matrix Composite." *Journal of the American Ceramic Society,* 82, 1999: 3087-3096.

15. Mall, S. and W.A. Weidenaar. "Tension-Compression Fatigue Behaviour of Fibre-Reinforced Ceramic Matrix Composite with Circular Hole." *Composites, 26*, 1995: 631-636.

16. Mazdiyasni, K.S. *Fiber Reinforced Ceramic Composites: Materials, Processing, and Testing.* Park Ridge, NJ: Noyes Publications, 1990.

17. McNulty, J.C., M.Y. He, and F.W. Zok. "Notch Sensitivity of Fatigue Life in a Sylramic™/SiC composite at elevated temperature." *Composites Science and Technology, 61,* 2000: 1331-1338.

18. Schmidt, S., H. Knabe, H. Immich, R. Mestring, and A. Gessler. "Advanced Ceramic Matrix Composite Material for Current and Future Propulsion Technology Applications." *Acta Astronautica, 55*, 2004: 409-420.

Vita

2d Lt Garrett Kurtz was raised in Bairdford, Pennsylvania, a rural suburb of Pittsburgh. He graduated from Deer Lakes High School in 2005 and entered the United Stated Air Force Academy in Colorado Springs, Colorado in the summer of 2005. In May of 2009, he graduated with a Bachelor of Science Degree in Mechanical Engineering.

Lieutenant Kurtz's first assignment was to the Graduate School of Engineering and Management, Air Force Institute of Technology. Upon graduation he will take an assignment in the Air Force Research Lab (AFRL) propulsion directorate at Wright-Patterson AFB, OH.

REPORT DOCUMENTATION PAGE		*Form Approved* *OMB No. 0704–0188*

1. REPORT DATE (DD–MM–YYYY) 24-03-2011	2. REPORT TYPE Master's Thesis	3. DATES COVERED *(From — To)* Aug 2009 – Mar 2010

4. TITLE AND SUBTITLE Notch Sensitivity of Fatigue Behavior of a Hi-Nicalon/SiC Ceramic Composite with an Oxidation Inhibited Matrix at 1200°C in Air and in Steam	5a. CONTRACT NUMBER 5b. GRANT NUMBER 5c. PROGRAM ELEMENT NUMBER
6. AUTHOR(S) Kurtz, Garrett, 2d Lt, USAF	5d. PROJECT NUMBER 5e. TASK NUMBER 5f. WORK UNIT NUMBER
7. PERFORMING ORGANIZATION NAME(S) AND ADDRESS(ES) Air Force Institute of Technology Graduate School of Engineering and Management (AFIT/ENY) 2950 Hobson Way WPAFB OH 45433-7765	8. PERFORMING ORGANIZATION REPORT NUMBER AFIT/GAE/ENY/11-M17
9. SPONSORING / MONITORING AGENCY NAME(S) AND ADDRESS(ES) Intentionally Left Blank	10. SPONSOR/MONITOR'S ACRONYM(S) 11. SPONSOR/MONITOR'S REPORT NUMBER(S)

12. DISTRIBUTION / AVAILABILITY STATEMENT
APPROVED FOR PUBLIC RELEASE; DISTRIBUTION UNLIMITED

13. SUPPLEMENTARY NOTES
This material is declared a work of the United States Government and is not subject to copyright protection in the United States.

14. ABSTRACT

The effects of holes on the fatigue behavior of an advanced Silicon Carbide/Silicon Carbide (SiC/SiC) ceramic matrix composite (CMC) was investigated at 1200°C in laboratory air and in steam environment. The composite consisted of an oxidation inhibited HyprSiC matrix reinforced with laminated Hi-Nicalon fibers woven in an eight-harness-satin weave (8HSW). Fiber preforms were coated with pyrolytic carbon (PyC) fiber coating with boron carbide overlay and were then densified with HyprSiC matrix via chemical vapor infiltration (CVI). Effects if center hole on tensile stress-strain behavior and tensile properties were evaluated at 1200ºC. To assess the effect of holes on fatigue performance, the standard dogbone-shaped specimens with a center-hole were subjected to tension-tension fatigue tests at frequencies of 0.1, 1.0, and 10 Hz for fatigue stresses ranging from 80 to 140 MPa in air and from 100 to 140 MPa in steam. The R ratio (minimum stress to maximum stress) was 0.05. Fatigue run-out was defined as 10^5 cycles at the frequency of 0.1 Hz and as $2x10^5$ cycles at the frequencies of 1.0 and 10 Hz. Specimens that achieved run-out were tested in tension to failure to characterize the retained tensile properties. Composite microstructure, as well as damage and failure mechanisms were investigated.

15. SUBJECT TERMS
Ceramic Matrix Composite (CMC), Silicon Carbide/Silicon Carbide (SiC/SiC), Chemical Vapor Infiltration (CVI), Fatigue Testing, Material Properties, Cyclic Loading, Notch Sensitivity, Environmental Testing

16. SECURITY CLASSIFICATION OF:			17. LIMITATION OF ABSTRACT	18. NUMBER OF PAGES	19a. NAME OF RESPONSIBLE PERSON Dr. Marina B. Ruggles-Wrenn
a. REPORT U	b. ABSTRACT U	c. THIS PAGE U	UU	135	19b. TELEPHONE NUMBER (Include Area Code) (937)255-3636, ext 4641 Email: marina.ruggles-wrenn@afit.edu

Standard Form 298 (Rev. 8–98)
Prescribed by ANSI Std. Z39.18